REGION-OF-INTEREST RECONSTRUCTION FROM TRUNCATED CONE-BEAM CT

A Dissertation Presented to

the Faculty of the Department of Mathematics

University of Houston

In Partial Fulfillment

of the Requirements for the Degree

Doctor of Philosophy

By

Tasadduk Chowdhury

August 2016

REGION-OF-INTEREST RECONSTRUCTION FROM TRUNCATED CONE-BEAM CT

Tasadduk Chowdhury

Approved:

Dr. Robert Azencott (Committee Chair)
Department of Mathematics, University of Houston

Committee Members:

Dr. Demetrio Labate
Department of Mathematics, University of Houston

Dr. Bernhard Bodmann
Department of Mathematics, University of Houston

Dr. Shishir Shah
Department of Computer Science, University of Houston

Dean, College of Natural Sciences and Mathematics
University of Houston

Acknowledgements

First and foremost, I deeply acknowledge my advisor Dr. Robert Azencott, to whom I will forever be indebted for his constant support and guidance during my graduate student career.

I would like to thank the committee members, Dr. Demetrio Labate, Dr. Bernhard Bodmann, and Dr. Shishir Shah, for taking the time from their busy lives to read this thesis and share valuable insights.

I want to thank Dr. Anando Sen for his endless collaborative support since the beginning of this project and for always being a good friend to me.

I thank all my friends in the UH Math Department, including Francois, Angelynn, Cameron, Ricky, Aarti, Brett, Kayla, Rachel, Pankaj, Rahul, Ananya, Pei, Hungzen, Danil, Jared, Illja, and others, for providing me moral support, courage, and advice.

I will forever be thankful to my lovely wife, Jannatul Ferdous, for being unconditionally supportive and caring to me all the time (especially during the writing stage of this thesis) and for teaching me how to be optimistic and confident.

Finally, I would like to thank my mother and my step-father for always believing in me. My success is due to their encouragements. I will forever honor them for the sacrifices they had made for me. I consider myself to be the most lucky person on the planet to have them as my parents.

This thesis is dedicated to my mother Afroza Begum, my step-father Muslehuddin A. Khan, and my wife Jannatul Ferdous.

REGION-OF-INTEREST RECONSTRUCTION FROM TRUNCATED CONE-BEAM CT

An Abstract of a Dissertation

Presented to

the Faculty of the Department of Mathematics

University of Houston

In Partial Fulfillment

of the Requirements for the Degree

Doctor of Philosophy

By

Tasadduk Chowdhury

August 2016

Abstract

This thesis presents a novel algorithm in 3D computed tomography (CT) dedicated to accurate region of interest (ROI) reconstruction from truncated cone-beam projections. Here data acquisition involves cone-beam x-ray sources positioned on any piecewise smooth 3D-curve satisfying the very generic, classical Tuy's conditions and uses only x-rays passing through the ROI. Our ROI-reconstruction algorithm implements an iterative procedure where we systematically alternate intermediary reconstructions by an exact non-truncated cone-beam inversion operator, with an effective density regularization method. We validate the accuracy of our ROI-reconstruction algorithm for a 3D Shepp-Logan phantom, a 3D image of a Mouse, and a 3D image of a human jaw, for different cone-beam acquisition curves, including the twin-orthogonal circles and the spherical spiral curve, by simulating ROI-censored cone-beam data and our iterative ROI-reconstruction for a family of spherical ROIs of various radii. The main result is that, provided the density function is sufficiently regular and the ROI radius is larger than a critical radius, our procedure converges to an ϵ-accurate reconstruction of the density function within the ROI. Our extensive numerical experiments compute the critical radius for various accuracy levels ϵ. These results indicate that our ROI reconstruction is a promising step towards addressing the dose-reduction problem in CT imaging.

Contents

List of Figures

List of Tables

Chapter 1

Introduction

1.1 Background and Motivation

Computed tomography (CT) is an indispensable non-invasive procedure that is commonly used in the field of medical imaging and other industries to acquire the internal images of an object using x-rays. The word "tomography" is derived from the greek word $\tau o \mu o \sigma$, meaning *slice* [42]. Modern x-ray CT allows one to visualize the internal structure of a three-dimensional object as two-dimensional slices by computing the spatial density of the x-ray linear-attenuation coefficient (LAC), the physical parameter that distinguishes the internal structures from each other [7]. The spatial density of the LAC of an anatomical object is acquired indirectly by solving an inverse problem which uses certain external measurements of the LAC density. Each measurement is an integral of the LAC density along a line, representing a narrow pencil beam of x-rays. The line-integral is indirectly obtained using using Lambert-Beer's law [7,31], by taking the logarithm of the ratio between the number of photons that enters the

object and the number of photons that exits.

The inception of the classical CT started during the 1960s and the 1970s, with the pioneering works of Godfrey Hounsfield and Allan Cormack [7]. They received the Nobel Prize for Medicine in 1979 for the invention of the first x-ray CT scanner and the development the early reconstruction algorithms. In the 1970s, CT imaging devices known as the *third-generation CT scanners* reconstructed the 2D cross-sectional images of a 3D density by irradiating each cross-section with divergent fan-beam of x-rays, rotating around the object along a circular path. One major disadvantage of the 2D cross-sectional CT imaging via fan-beam x-rays is its lengthy acquisition time. Since the movement of a patient is unavoidable for a long period of time, fan-beam CT images usually have motion artifacts [7, 57]. With the arrival of cone-beam CT scanners commonly referred to as the *seventh-generation CT scanners* or the *multi-slice CT scanners* [7], the data acquisition time for 3D CT was significantly shortened. The cone-beam x-ray measurements are made by x-rays originating from a point source and penetrating the 3D object of interest, where the source moves around the object along a curve that surrounds the object. Compared to fan-beam CT, cone-beam CT requires relatively less acquisition time and provide highly accurate 3D image reconstruction. With the invention of the seventh-generation cone-beam CT scanner and an overflow of cone-beam reconstruction algorithms developed between the mid 1980s to mid 1990s (see [7, 43, 57] for a comprehensive list), most of the CT research interests shifted from the cross-sectional density reconstruction from fan-beam x-rays to *fully 3D image reconstruction* from cone-beam x-rays.

Although several competing medical imaging modalities were invented during the 1980s, such as magenetic resonance imaging (MRI) and positron emission tomography

(PET), CT still remains to be the most-widely-used imaging method in radiology to date [7]. Currently, the number of medical CT scans performed in the US and Japan are about 85 million and 63 million, respectively [6]. Besides its popularity in the medical industry, applications of computed tomography have been developed recently in other areas, such as forensics, archeology, and paleontology, [7]. In the industry, Cone-beam scanners are used for non-destructive evaluation of products such as metal parts and ceramic materials [57, 61].

Despite its popularity in the medical imaging, CT scans may cause risks of cancer to patients due to high radiation levels of x-rays. X-ray radiation can severely damage body cells and DNA molecules, which can eventually lead to cancer [6]. A study of 10.9 million people in Australia [40] reported that the increased incidence of cancer after CT scan exposure in this group was mostly due to irradiation, where one in 1800 CT scans was followed by an excess cancer. The health risks of radiation-induced carcinogenesis have shown to be essentially proportional to radiation exposure levels [22].

The collective dosage of radiation to patients may be reduced either by minimizing the number of CT scans that are not medically necessary, or by reducing the dose per CT scan [6]. It may not be possible to reduce the number of CT scans required for a patient undergoing regular scanning to monitor the growth of a tumor. However, the level of x-ray dosage can be reduced significantly by using restricted cone-beam x-ray scanning, where the x-rays are only allowed to pass through a small region-of-interest (ROI) located within the whole object.

This thesis presents a novel algorithm in cone-beam CT that reconstructs the ROI density of an object accurately from restricted cone-beam x-rays, while substantially

reducing the overall dosage during the acquisition stage. Here data acquisition involves x-ray sources positioned on any piecewise smooth 3D-curve satisfying the very generic, Tuy's conditions and uses only x-rays passing through the ROI. Our ROI reconstruction algorithm converges for sufficiently large spherical ROIs within the density support at exponential speed. This claim was verified using simulated acquisition of ROI-truncated cone-beam projection data for various acquisition geometries, including the twin-circular curve and the spherical spiral curve.

1.2 Outline

This thesis is divided into 12 chapters including the Introduction.

Chapter 2 reviews the current state of the art local CT reconstruction from truncated projection data.

Chapter 3 recalls thoroughly the classical mathematical theory of cone-beam computed tomography. We introduce the cone-beam transform, which integrates an appropriate function f over half-lines in $\mathbb{R}^3$. To acquire cone-beam data, the source of the cone-beam moves along a smooth curve in $\mathbb{R}^3$ that surrounds the support of f. The aim of cone-beam CT is to reconstruct a density f from its cone-beam transform. We discuss the well-known *Tuy's condition* [59] of the source curve, which determines whether an exact inversion of the cone-beam transform is possible, and give examples of curves that satisfy the condition. In addition, we present Tuy's exact cone-beam inversion formula [59]. Although Tuy's formula is not computationally efficient, many inversion formulas have been derived from it.

In **Chapter 4**, we introduce the classical 3D Radon transform, which maps an appropriate function f on $\mathbb{R}^3$ to its integrals over planes. A few important proper-

ties of the Radon transform are briefly discussed. The most remarkable theorem in tomography, the Fourier Slice Theorem, is presented, and is used to derive the inversion of the Radon transform. An efficient numerical method to invert the 3D Radon transform is presented.

In **Chapter 5** we present Grangeat's fundamental relation between the 3D Radon transform and the cone-beam transform [20]. We explain how this link between the 3D Radon transform and the cone-beam transform can be exploited to devise a computationally efficient cone-beam inversion method. Finally, we present a robust *filtered backprojection* (FBP) type cone-beam inversion method, derived by Defrise and Clack [13]. This method is a variant of Grangeat's original inversion formula.

For proper medical diagnosis, it is important to produce high quality CT images. It is just as important to decrease the overall x-ray radiation exposure on patients to decrease health risks. In chapter **Chapter 6**, we introduce the notion of reconstruction via ROI truncated cone-beam transform, where the cone-beam rays are only allowed to pass through a fixed region-of-interest within the support of the density. We present a new algorithm for accurate reconstruction from truncated cone-beam projections acquired on arbitrary curves satisfying Tuy's condition. A major component of our ROI reconstruction algorithm requires effective regularization of densities. **Chapter 7** discusses several wavelets-based regularization methods .

In **Chapter 8**, we present two numerical non-truncated cone-beam inversion algorithms based on Grangeat's formula with cone-beam data acquired from a generic smooth curve satisfying Tuy's condition. Next, we describe the numerical implementation of our ROI reconstruction algorithm. The algorithm is implemented on a general setting and applies to any curve satisfying Tuy's condition.

Numerical ROI reconstruction results for a set of 3D images are presented in **Chapter 9**, with acquisition on the twin-circular curve. We choose arbitrary spheres of various radii placed within the support of the density f as the ROIs. To prove the robustness and accuracy of our method, we compare it against a naive method for ROI reconstruction, which applies inversion method directly on the truncated cone-beam data. Our ROI reconstruction algorithm performed much better, giving relative reconstruction of 10% in most cases, for relatively small spherical ROIs strictly within the density. Our numerical experiments confirm that the algorithm converges to an ϵ-accurate image within the ROI, given that the ROI is a sphere which is no smaller than a critical radius, which depends on the level of accuracy demanded.

In **Chapter 10**, we present a non-truncated cone-beam inversion method based on the exact cone-beam FBP formula, with acquisition on a non-standard spherical spiral trajectory. We outline how an effective source weighting function M can be computed efficiently. In Chapter **Chapter 11**, we validate our ROI reconstruction algorithm, using the spherical spiral inversion technique developed in the previous chapter, through numerical ROI reconstruction of several discretized densities.

In **Chapter 12**, we discuss some limitations of our algorithm and possible extensions to intriguing research areas.

Note: Material in this thesis has appeared elsewhere. Parts of Chapter 6 has appeared in [3] and parts of Sections 6.4 has appeared in [8].

Chapter 2

State-of-the-Art Region-of-Interest Tomography

The problem of region of interest (ROI) reconstruction from truncated projections in CT has been studied in multiple papers and using a variety of methods. According to Natterer [41], incomplete data problems (in 2D or 3D) can be categorized into the following three categories:

1. *Limited angle/source problems.* Here, if the source curve Γ is parametrized as $\{s(\lambda) : \lambda \in \Lambda\}$, then the non-truncated projection data is acquired from a subset $\{s(\lambda) : \lambda \in \Lambda'\}$ of Γ, where $\Lambda' \subset \Lambda$.

2. *Exterior problems.* Here, the projection data is acquired from all source positions, and for a fixed region of interest C, measurements of all x-rays passing through C are discarded. This problem aims to recover the density outside of C.

3. *Interior problems.* Here, the projection data is acquired from all source posi-

tions, and for a fixed region of interest C, line-integral measurements are kept only for the rays passing through C. This problem aims to recover the density strictly restricted to the region of interest C.

Natterer proved in [41] that the interior problem does not have an unique solution in general. Regardless of the loss of uniqueness, there has been extensive research in local reconstruction from ROI-restricted projections in CT literature (see [9] and [60] recent reviews). In this chapter, we present briefly a few approximate and exact methods for 2D and 3D ROI-reconstruction from truncated projections.

2.1 Wavelets-based ROI-Reconstruction

In the past, wavelets have been used to localize the 2D Radon transform in order to solve the the two-dimensional interior problem. Papers by Tim Olson and Joe Destefano [47, 48] developed a multi-resolution method that uses the properties of wavelets to localize the 2D Radon transform in order to reconstruct approximately a local region of interest. This wavelet-based tomographic method is not truly local as it requires line-integral measurements of the density from all rays passing through the region of interest C and a small fraction of the rays not passing through C. Rashid-Farrokhi *et al* [50] developed a wavelet-based method which uses locally restricted projection data, and found that the reconstruction error of their method depends on the amount of data used in the algorithm. One of the first 3D ROI cone-beam CT problem in the wavelet framework was first solved by Zhao and Wang [68]. Their main contribution was the reformulation of the FDK cone-beam reconstruction algorithm from the wavelet perspective, using both full and half-circular non-truncated cone-

beam data acquisition, for either global or local approximate reconstruction without severe image artifacts.

One should note that all the ROI-reconstruction methods mentioned above are approximate and have no theoretical basis for exact and stable reconstruction. Recently, Klann *et al.* [30] presented a wavelet-based algorithm for 2D region of interest tomography form ROI-restricted data which converges to the exact density. In the paper, it is proved that piecewise constant densities f of the following form

$$f(x) = \sum_{n=1}^{N} a_n 1_{\Omega_n}(x),$$

where each set Ω_n is compact with piecewise smooth boundary and nontrivial interior, are determined by their ROI-restricted x-ray data. Klann *et al.* [30] developed an algorithm using a Haar wavelet basis and used a weighted ℓ_p-penalty with weights that depend on the relative location of wavelets to the region of interest. Various tests were performed on phantoms to demonstrate the effectiveness of the method. Besides requiring densities to be piecewise constant, their method assumes the ideal case of a noiseless acquisition.

2.2 Known Sub-region ROI-Reconstruction

In many practical situations, the density f is known on a sub-region in advance, such as air in airways, blood through vessels, or images from prior CT scans. Courdurier *et al.* [10] showed that when the attenuation function is *a priori* known in a sub-region, a reduced set of x-ray measurements are enough to uniquely determine the whole density. Stability estimates were derived to show that reconstruction can be

stable near the region the attenuation is known. Similar types of ROI-reconstruction problems with *a priori* knowledge of the ROI density were explored in [64, 65]. However, these methods have serious limitations in the sense that the precise sub-region knowledge maybe unavailable in many important cases such as perfusion cardiac CT/micro-CT [29].

2.3 Sparse ROI-Reconstruction

Recent research efforts have been made in region-of-interest reconstruction from ROI-truncated projections based on compressive sensing (CS). The Nyquist-Shannon sampling theorem states that a signal must be sampled at least twice as fast as its maximum frequency for a an exact recovery. The CS theory has the power to sample compressible signals at a rate much less than the Nyquist rate and yet allow accurate reconstruction of these signals. Using the theory of compressed sensing, Yu and Wang [66] recently showed that exact 2D region-of-interest reconstruction is theoretically achievable with ROI-truncated projection data if the density f is a piecewise polynomial on the ROI. Their method uses ROI-truncated data to iteratively reconstruct the interior by minimizing the total variation of a reconstructed image. It was empirically demonstrated that the interior problem is stable when the density f is piecewise polynomial on the ROI.

Recently, Katsevich *et al.* [29] considered a similar problem as above, but with the assumption that f_{ROI}, the density f restricted to the region of interest, is a polynomial, rather than being piecewise polynomial. Assuming that the degree of the polynomial of f_{ROI} is known, along with some other fairly mild assumptions, a stability estimate for the interior problem was presented. In addition, Katsevich

et al. [29] proved the following general uniqueness result: if there is an open set $C \subset \operatorname{supp} f$ on which f_{ROI} is the restriction of a real-analytic function, then f_{ROI} is uniquely determined by the x-ray measurement restricted only to the rays passing through C.

Generalized total variation based interior tomography, in 2D and 3D, is explored in [34, 62]. The authors proposed a novel multiscale reconstruction method, which uses the Bedrosian identity of the Hilbert transform to show that the high frequency parts of the one-dimensional signals can be quickly recovered analytically. This implies that computationally expensive iterative reconstruction need only be applied to low resolution images in the down-sampled domain, which significantly reduces the computational burden. Recall that non-truncated cone-beam acquisition from planar curves do not provide sufficient data for exact reconstruction (see Tuy's condition in Chapter 3). It was shown that for acquisition from incomplete cone-beam source curves (e.g., a circular curve), their multi-scale interior tomography approach can be combined with a novel spectral blending method to mitigate cone-beam artifacts from missing frequency regions. The efficacy of their algorithm was validated using truncated cone-beam data acquired from helical and circular trajectories.

2.4 Iterative ROI-Reconstruction Algorithms

In the past, iterative methods were shown to provide a more flexible alternative for the reconstruction from truncated or incomplete cone-beam projections since they can be applied to essentially any type of acquisition mode [55, 69]. However, those ROI-reconstruction methods are mostly heuristic and provide no theoretical justification for convergence. The ROI-reconstruction method presented in this thesis is

an extension to the method presented in the PhD thesis of our collaborator Anando Sen [51], who has provided constant guidance in the process of writing this thesis. In each step of the iterative ROI-reconstruction algorithm in [51], a non-truncated cone-beam inversion $\mathcal{D}^{-1}$ is applied to the ROI-truncated projection data, followed by an application of a density regularization (local averaging or hard wavelets thresholding) to the reconstructed density. One shortcoming of the algorithm from Sen's thesis is that it was only used with cone-beam inversion operators $\mathcal{D}^{-1}$ that rely on specific imaging geometries. For example, Sen explored in [51] ROI-reconstruction using the Fourier-based cone-beam filtered backprojection, which requires cone-beam sources to lie on the sphere surrounding the density support.

Chapter 3

Classical Non-truncated Cone-beam Reconstruction

In cone-beam tomography, one considers the exact reconstruction of a suitable three-dimensional density function by inverting its non-truncated cone-beam transform. The cone-beam transform integrates a density over all half-lines originating from a source point, which is located on a smooth curve in the three-dimensional space. By non-truncated cone-beam transform, we mean that each nonzero line integral value of the density is available. The case when some of the line-integral data are missing is known as the *truncated* cone-beam transform. Not all source curves actually permit an exact inverse of the cone-beam transform. Only a family of curves satisfying a set of special conditions permit exact reconstruction of a compactly supported density from cone-beam measurements. A handful of researchers, including Tuy [59], Smith [56], and Grangeat [19, 20], independently developed exact cone-beam reconstruction formulas in the 80s and 90s. Although their formulas appear to be different, they all

require the same condition on the source curve for exact reconstruction of the density.

In this chapter, we present Tuy's cone-beam inversion formula [59] and the completeness conditions for exact reconstruction of a density from the non-truncated cone-beam transform.

3.1 Definitions

Let $\mathbb{S}^2$ denote the unit sphere centered at the origin in $\mathbb{R}^3$. Recall that a *ray* $r(s,\beta)$ is a half-line in $\mathbb{R}^3$ that originates from a point s and extends in the direction of a unit vector $\beta \in \mathbb{S}^2$. That is,

$$r(s,\beta) = \{x \in \mathbb{R}^3 : s + t\beta, t \in \mathbb{R}\}.$$

Assume that the density function $f : \mathbb{R}^3 \to \mathbb{R}$ is smooth and has a compact support Ω. The cone-beam transform integrates a density function f over rays in $\mathbb{R}^3$, where the sources of the beam belong to a smooth three-dimensional curve Γ. We assume that $\Omega \subset B$ and $\Gamma \subset V$, where B is a closed ball in $\mathbb{R}^3$ and V is a compact subset of $\mathbb{R}^3 \setminus B$.

Definition 3.1.1. The *cone-beam transform* (or the *divergent beam transform*) $\mathcal{D}$ of a function $f : \mathbb{R}^3 \to \mathbb{R}$ of compact support is defined as the following integral transform

$$\mathcal{D}f(s,\beta) = \int_0^\infty f(s + t\beta)\, dt, \quad s \in \mathbb{R}^3, \beta \in \mathbb{S}^2. \tag{3.1}$$

The value $\mathcal{D}f(s,\beta)$ represents the integral of f over the ray $r(s,\beta)$. We refer to the point $s \in \mathbb{R}^3$ as the *source* of the cone-beam transform. In a practical medical

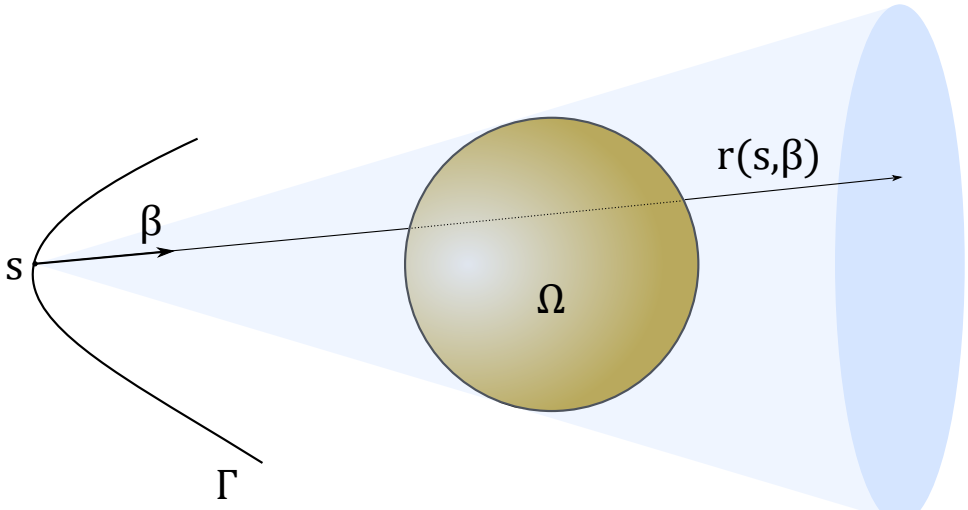

Figure 3.1: The cone-beam transform of the density function f integrates f over the ray $r(s, \beta)$ originating from the source s and in the direction $\beta \in \mathbb{S}^2$.

imaging setting, the sources of the cone-beam are located on a smooth curve $\Gamma \subset \mathbb{R}^3$ surrounding the support Ω of f (see Figure 3.1). For a fixed source position $s \in \Gamma$, the set of all values $\mathcal{D}f(s, \beta)$ is called the *cone-beam projection of* f. Note that the cone-beam projection of f from a source $s \in \Gamma$ is obtained by integrating f only over those rays $r(s, \beta)$ that intersect Ω. The transform is given its name since these rays originating from source s and penetrating the support Ω form the shape of a cone.

Remark 3.1.2. For a compactly supported 3D density function f, its *X-ray transform* Xf is defined as [43]

$$Xf(x, \beta) = \int_{-\infty}^{\infty} f(x + t\beta)\, dt, \quad x \in \Omega, \quad \beta \in \mathbb{S}^2.$$

We see that the cone-beam transform and the X-ray transform are identical, except when $x \in \Omega$. Many researchers in the tomography literature use these terms interchangeably.

3.2 A Brief Review of Distributions

Schwartz's theory of distributions has many applications in various fields of science and engineering. The theory of distrubtions plays a key role in the derivations of many popular reconstruction algorithms of computed tomography. For example, the 2D Radon inversion formula uses the Hilbert Transform of a function, which is an integral that does not converge in the ordinary sense [41, 43]. In 3D cone-beam computed tomography, intermediary functions in Tuy's formula [59], Grangeat's formula [20], and Smith's formula [56], use distributions that may or may not exist as functions in the ordinary sense. In this section, we briefly discuss the concept of distributions and some results relevant to derivation of inversion formulas in cone-beam tomography. An in-depth study on the topic of distributions can be found in [4, 18, 36].

The Schwartz Space

An infinitely differentiable function ψ on $\mathbb{R}^n$ is *rapidly decreasing at infinity* if

$$\lim_{||x|| \to \infty} |x^p \partial^q \psi(x)| = 0$$

for all $p \in \mathbb{N}^n$ and for all $q \in \mathbb{N}^n$, where $\mathbb{N}^n$ is the set of n-tuples of positive integers. In other words, a smooth function ψ is rapidly decreasing if ψ and all of its derivatives decrease faster than any inverse power of $||x||$ at infinity. The class of all rapidly

decreasing functions denoted by $\mathcal{S}(\mathbb{R}^n)$ forms a vector space over $\mathbb{R}^n$. One commonly refers to $\mathcal{S}(\mathbb{R}^n)$ as the *Schwartz space* of functions.

A sequence of functions $\{\psi_j\}$ *converges to zero* in $\mathcal{S}(\mathbb{R}^n)$ if $x^p \partial^q \psi(x) \to 0$ uniformly on $\mathbb{R}^n$ as $j \to \infty$, for all $p, q \in \mathbb{N}^n$ [4]. A linear functional T over $\mathcal{S}(\mathbb{R}^n)$ is said to be *continuous* if for any sequence $\{\psi_j\}$ converging to zero in $\mathcal{S}(\mathbb{R}^n)$, we have

$$\lim_{j\to\infty} \langle T, \psi_j \rangle = 0,$$

where $\langle T, \psi \rangle$ represents the value of T on $\psi \in \mathcal{S}(\mathbb{R}^n)$.

Distributions and their Properties

A continuous linear functional T over $\mathcal{S}(\mathbb{R}^n)$ is called a *distribution* or a *generalized function*. A distribution can be defined over other classes of *test functions*, such as $C_c^\infty(\mathbb{R}^n)$, the space of compactly supported infinitely differentiable functions. To distinguish from others, a distribution over the test function space is $\mathcal{S}(\mathbb{R}^n)$ is called a *tempered distribution*. The set of all distributions over $\mathcal{S}(\mathbb{R}^n)$ is denoted by $\mathcal{S}'(\mathbb{R}^n)$

Any locally integrable function f can be used to generate a distribution:

$$\langle f, \psi \rangle = \int_{\mathbb{R}^n} f(x)\psi(x)\, dx. \tag{3.2}$$

Any such distribution which can be associated with an ordinary function is said to be *regular*. There exist many distributions in which are not regular. For example, Dirac's *delta distribution* on $\mathcal{S}(\mathbb{R})$:

$$\langle \delta, \psi \rangle = \psi(0), \quad \text{for all } \psi \in \mathcal{S}(\mathbb{R}). \tag{3.3}$$

One can easily verify that δ is a continuous linear functional on $\mathcal{S}(\mathbb{R})$. However, there exist no ordinary function which has the sifting property of the delta distribution. Such distributions that cannot be generated by ordinary functions are called *singular*. In practice, it is quite common to see singular distributions written as ordinary functions. For example, the values of the delta distribution is usually written as

$$\langle \delta, \psi \rangle = \int_{-\infty}^{\infty} \delta(x)\psi(x)\, dx = \psi(0).$$

It is understood that the integral is written formally to be consistent with the definition of regular distributions in (3.2). One should keep in mind that the δ-distribution does not make sense point-wise as ordinary functions, although it appears as $\delta(x)$ inside the formal integral.

If T is a distribution, then $\partial^q T$, the partial derivative of T of order $q \in \mathbb{N}^n$ exists as a distribution in the following sense:

$$\langle \partial^q T, \psi \rangle = (-1)^{|q|} \langle T, \partial^q \psi \rangle, \quad \text{for all } \psi \in \mathcal{S}(\mathbb{R}^n),$$

where $|q| = \sum_{i=1}^{n} q_i$. If T is generated by a differentiable function f of order $q \in \mathbb{N}^n$, then its distributional derivatives and classical derivatives coincide. It is interesting to note that functions which do not have derivatives in the classical sense have derivatives in the sense of distributions. Using distributional derivatives and the definition of the δ-distribution, one can define the singular distribution δ':

$$\langle \delta', \psi \rangle = -\langle \delta, \psi' \rangle = -\psi'(0), \quad \text{for all } \psi \in \mathcal{S}(\mathbb{R}). \tag{3.4}$$

Any singular distribution can be seen as the limit of a sequence of regular distributions [18, 36]. If T is a distribution on $\mathcal{S}(\mathbb{R}^n)$, then there exist a sequence of regular distributions $\{T_n\}$ in $\mathcal{S}'(\mathbb{R}^n)$ such that

$$\lim_{n\to\infty} \langle T_n, \psi \rangle = \langle T, \psi \rangle, \quad \text{for all } \psi \in \mathcal{S}(\mathbb{R}^n). \tag{3.5}$$

Note that different regular sequences can lead to the same value of $\lim_{n\to\infty}\langle T_n, \psi\rangle$. Hence, a singular distribution T is associated with a class of *equivalent regular sequences*, where each sequence satisfies (3.5). For example, the δ-distribution can be approximated by [18]

$$\langle \delta, \psi \rangle = \lim_{\epsilon\to 0^+} \left\langle \frac{1}{\pi}\frac{\epsilon}{x^2+\epsilon^2}, \psi(x) \right\rangle,$$

or,

$$\langle \delta, \psi \rangle = \lim_{a\to\infty} \left\langle \frac{\sin ax}{\pi x}, \psi(x) \right\rangle,$$

for all $\psi \in \mathcal{S}(\mathbb{R})$. When a distribution T is the limit of a regular sequence $\{T_n\}$, one commonly writes

$$\lim_{n\to\infty} T_n = T,$$

where the limit is to be understood in the sense of distributions, as in (3.5).

Distributions are only compared on open sets [18,36]. Two distributions T and T' in $\mathcal{S}'(\mathbb{R}^n)$ are said to be *equal on an open set* $\Omega \subset \mathbb{R}^n$ if $\langle T, \psi\rangle = \langle T', \psi\rangle$ for all test functions $\psi \in \mathcal{S}(\mathbb{R}^n)$ with $\operatorname{supp}\psi \subset \Omega$. This fact allows one to compare a singular distribution with a regular distribution generated by a locally integrable function on certain open sets. If $T \in \mathcal{S}'(\mathbb{R}^n)$ and f is a locally integrable function on $\mathbb{R}^n$ such

that

$$\langle T, \psi \rangle = \langle f, \psi \rangle$$

for all $\phi \in \mathcal{S}(\mathbb{R}^n)$ with $\operatorname{supp} \psi \subset \Omega$, where Ω is some open set of $\mathbb{R}^n$, then $T = f$ on Ω in the sense of distributions. For example, the δ-distribution is equal to zero on $(-\infty, 0)$ and $(0, \infty)$.

The Fourier transform $\hat{\psi}$ of a test function $\psi \in \mathcal{S}(\mathbb{R}^n)$ is defined as usual:

$$\hat{\psi}(\xi) = (2\pi)^{-n/2} \int_{\mathbb{R}^n} \psi(x)\, e^{-i\langle x, \xi \rangle}\, dx, \quad \xi \in \mathbb{R}^n.$$

Note that $\hat{\psi}$ is a function rapidly decreasing at infinity since $\psi \in \mathcal{S}(\mathbb{R}^n)$ [4]. Each tempered distribution has a well-defined Fourier transform. If T is a tempered distribution, then its Fourier transform $\widehat{T}$ is a tempered distribution defined by

$$\langle \widehat{T}, \psi \rangle = \langle T, \hat{\psi} \rangle, \quad \text{for all } \psi \in \mathcal{S}(\mathbb{R}^n). \tag{3.6}$$

Each property of the classical Fourier transform on $\mathcal{S}(\mathbb{R}^n)$ also holds for the distributional Fourier transform. These results and their proofs can be found in [4, 18].

3.3 Fourier Transform of the Cone-beam Transform as a Distribution

As before, assume that the density f is smooth and compactly supported. For theoretical purposes, one can extend the cone-beam transform $\mathcal{D}f$ from $\mathbb{R}^3 \times \mathbb{S}^2$ to a

function on $\mathbb{R}^3 \times \mathbb{R}^3 \setminus \{0\}$

$$\mathcal{D}f(s,y) = \int_0^\infty f(s+ty)\,dt = \frac{1}{||y||}\mathcal{D}f\left(s, \frac{y}{||y||}\right), \quad s \in \mathbb{R}^3, y \in \mathbb{R}^3 \setminus \{0\}. \tag{3.7}$$

Denote $\mathcal{D}_s f(y) \equiv \mathcal{D}f(s,y)$ when the source s of the cone-beam transform is fixed. As f is compactly supported, for each $s \in \mathbb{R}^3$, there exists a constant $C(s) > 0$ such that $|\mathcal{D}_s f(\beta)| \leq C(s)$ for all $\beta \in \mathbb{S}^2$. As the behavior of $\mathcal{D}_s f$ is similar to the function $||x||^{-1}$, the function $\mathcal{D}_s f$ generates a tempered distribution over $\mathcal{S}(\mathbb{R}^3)$ (see Tuy [59]). In fact, $\mathcal{D}_s f$ is a homogeneous distribution of degree -1. Thus, the Fourier transform of $\mathcal{D}_s f$ also exists as a tempered distribution, which is defined in terms of scalar products as

$$\langle \widehat{\mathcal{D}_s f}, \psi \rangle = \langle \mathcal{D}_s f, \hat{\psi} \rangle, \quad \text{for all } \psi \in \mathcal{S}(\mathbb{R}^3). \tag{3.8}$$

Tuy [59] observed that the Fourier transform of the cone-beam transform can be seen as a distributional limit of a regular sequence of distributions, generated by locally integrable functions. The ordinary functions in the sequence are expressed in terms of the Fourier transform of the original density function. This theorem is the main ingredient of the derivation of Tuy's cone-beam inversion formula.

Theorem 3.3.1. *Let $\widehat{f}$ be the Fourier transform of $f \in C_c^\infty(\mathbb{R}^3)$ and let $\{T_m\}$ be the sequence of regular distributions defined by*

$$T_m(\xi) = \int_0^m \rho \widehat{f}(\rho\xi) e^{i\rho\langle s,\xi\rangle}\,d\rho, \quad m > 0, \xi \in \mathbb{R}^3. \tag{3.9}$$

Then following holds for any test function $\psi \in \mathcal{S}(\mathbb{R}^3)$:

$$\langle \widehat{\mathcal{D}_s f}, \psi \rangle = \lim_{m\to\infty} \langle T_m, \psi \rangle = \lim_{m\to\infty} \int_{\mathbb{R}^3} T_m(\xi)\psi(\xi)\, d\xi. \tag{3.10}$$

Proof. See Tuy [59, Proposition 2]. □

3.4 Tuy's Inversion Formula

In 1983, Tuy [59] derived the very first closed-form exact inversion formulas for the cone-beam transform with acquisition from a bounded smooth curve in $\mathbb{R}^3$ satisfying a set of weak conditions. His formula served as a starting point for many other cone-beam inversion methods.

The 3D density to be reconstructed is the real integrable function f with compact support Ω. In Tuy's inversion method, the cone-beam sources are placed on a bounded, continuous, and piecewise differentiable curve Γ in $\mathbb{R}^3$, represented by a vector valued function $s : \Lambda \to \mathbb{R}^3$,

$$\Gamma = \{s(\lambda) \in \mathbb{R}^3 : \lambda \in \Lambda\},$$

where Λ is a finite union of intervals of the real-line. We assume that $\Omega \subset B$ and $\Gamma \subset V$, where B is a closed ball in $\mathbb{R}^3$ and V is a compact subset of $\mathbb{R}^3 \setminus B$. Tuy's inversion formula is valid if for all $x \in \Omega$ and for all $\beta \in \mathbb{S}^2$, the following conditions hold true:

1. There exists $\lambda = \lambda(x, \beta) \in \Lambda$ such that $\langle x, \beta \rangle = \langle s(\lambda), \beta \rangle$,
2. $\langle s'(\lambda), \beta \rangle \neq 0$.

These conditions are referred to as *Tuy's conditions*. It can be easily seen why a curve consisting of a circle fails Tuy's conditions. Take Γ to be a circle of radius $R > 0$ on a plane Π. Choose $x \in \Omega \cap (\mathbb{R}^3 \setminus \Pi)$; that is, x is a point in Ω which is not in P. Note that the plane parallel to Π which passes through x does not intersect Γ. Thus, we see that this curve Γ fails to satisfy Condition 1.

Theorem 3.4.1 (Tuy [59])**.** *Let $f \in C_c^\infty(\mathbb{R}^3)$. Then for $x \in \operatorname{supp} f$,*

$$f(x) = -i\,(2\pi)^{-3/2} \int_{\mathbb{S}^2} \frac{1}{\langle s'(\lambda), \beta \rangle}\, \partial_\lambda \left(\widehat{\mathcal{D}_{s(\lambda)} f}(\beta) \right) dQ(\beta), \tag{3.11}$$

where $\lambda = \lambda(x, \beta)$ is such that $\langle x, \beta \rangle = \langle s(\lambda), \beta \rangle$ and $\langle s'(\lambda), \beta \rangle \neq 0$, and dQ is the infinitesimal surface area on $\mathbb{S}^2$.

Proof. Recall that the Fourier transform of $\mathcal{D}_s f$ exists as a tempered distribution and by Theorem 3.3.1, we have

$$\widehat{\mathcal{D}_s f}(\xi) = \lim_{m \to \infty} \int_0^m \rho \widehat{f}(\rho\xi) e^{i\rho\langle s, \xi \rangle}\, d\rho, \quad \xi \in \mathbb{R}^3, \tag{3.12}$$

where the limit is understood in the sense of distributions. It can be shown that $\partial_\lambda(\widehat{\mathcal{D}_{s(\lambda)} f})$, the derivative of $\widehat{\mathcal{D}_{s(\lambda)} f}$ with respect to the source parameter also exists as a tempered distribution, and it can be expressed as the limit of a sequence of regular distributions [59, Proposition. 1]:

$$\partial_\lambda(\widehat{\mathcal{D}_{s(\lambda)} f}(\xi)) = i\langle s'(\lambda), \xi \rangle \lim_{m \to \infty} \int_0^m \rho^2 \widehat{f}(\rho\xi) e^{i\rho\langle s(\lambda), \xi \rangle}\, d\rho. \tag{3.13}$$

Again, the limit above is understood as a distribution. Recall that the 3D Fourier

inversion formula in spherical coordinates reads

$$f(x) = (2\pi)^{-3/2} \int_{\mathbb{S}^2} \int_0^\infty \rho^2 \widehat{f}(\rho\beta) e^{i\rho\langle\beta,x\rangle}\, d\rho\, dQ(\beta), \quad x \in \mathbb{R}^3. \tag{3.14}$$

The scalar product $\langle\beta, x\rangle$ can be replaced with $\langle\beta, s(\lambda)\rangle$ as Tuy's assumptions on the source curve Γ guarantee that there always exists at least one $\lambda \in \Lambda$ such that $\langle x, \beta\rangle = \langle\beta, s(\lambda)\rangle$ for any ordered pair $(x, \beta) \in \operatorname{supp} f \times \mathbb{S}^2$. Using this substitution along with with (3.13) and (3.4), we arrive at Tuy's cone-beam inversion formula:

$$f(x) = -i\,(2\pi)^{-3/2} \int_{\mathbb{S}^2} \frac{1}{\langle s'(\lambda), \beta\rangle}\, \partial_\lambda \left(\widehat{\mathcal{D}}_{s(\lambda)} f(\beta)\right)\, dQ(\beta). \tag{3.15}$$

It should be obvious to the reader why the assumption $\langle s'(\lambda), \beta\rangle \neq 0$ is necessary. □

Remark 3.4.2. One should note that Tuy's cone-beam inversion formula (3.11) holds in the sense of distributions. This means that for each open neighborhood U of $\Omega \equiv \operatorname{supp} f$, the original density function f and the left-hand side of (3.11) denoted by F, satisfy

$$\langle f, \psi\rangle = \langle F, \psi\rangle,$$

for all test function $\psi \in \mathcal{S}(\mathbb{R}^3)$ such that $\operatorname{supp}\psi$ is contained in U. This allows one to conclude that $f = F$ on any open set U contained in Ω. It was observed by Zeng, Clack, and Gullberg [67] more than a decade after Tuy's inversion formula was derived that further modification of the Tuy formula (3.11) leads to an exact cone-beam inverse involving only ordinary functions. We will omit the discussion of Zeng et al's formula as it is theoretically equivalent to Grangeat's cone-beam inversion formula [43] presented in Section 5.2.

3.5 Conditions on the Source Curve

Let us repeat Tuy's conditions on the source curve. For a smooth density $f : \mathbb{R}^3 \to \mathbb{R}$ compactly supported on Ω, a bounded and smooth curve $\Gamma = \{s(\lambda) : \lambda \in \Lambda\}$ where Λ is a finite union of intervals in the real line, the Tuy conditions are

Condition 1: There exists $\lambda = \lambda(x, \beta) \in \Lambda$ such that $\langle x, \beta \rangle = \langle s(\lambda), \beta \rangle$,

Condition 2: $\langle s'(\lambda), \beta \rangle \neq 0$.

In other words, every plane intersecting the support Ω must intersect the source curve Γ non-tangentially at least once. If these conditions are fulfilled, Theorem 3.4.1 guarantees exact recovery of $f(x)$ for all $x \in \Omega$ from the cone-beam transform. For this reason, the source curves Γ which satisfy Tuy's conditions are said to be *complete*.

We have pointed out earlier that circular orbit Γ (Figure 3.2a) surrounding the support Ω fails to be a complete curve in the sense of Tuy as there exist many planes, such as the ones parallel to plane containing the orbit, that intersect Ω without intersecting Γ. Thus, exact reconstruct is not possible from circular cone-beam acquisition. The following are examples of curves that satisfy Tuy's conditions, given that the object Ω is sufficiently small and surrounded by the curve Γ:

- Two perpendicular circles (Figure 3.2b)
- Twin circles connected by straight line segment (Figure 3.2c)
- A circular helix (on the surface of a cylinder) (Figure 3.2d)
- A spherical helix (on the surface of a sphere)

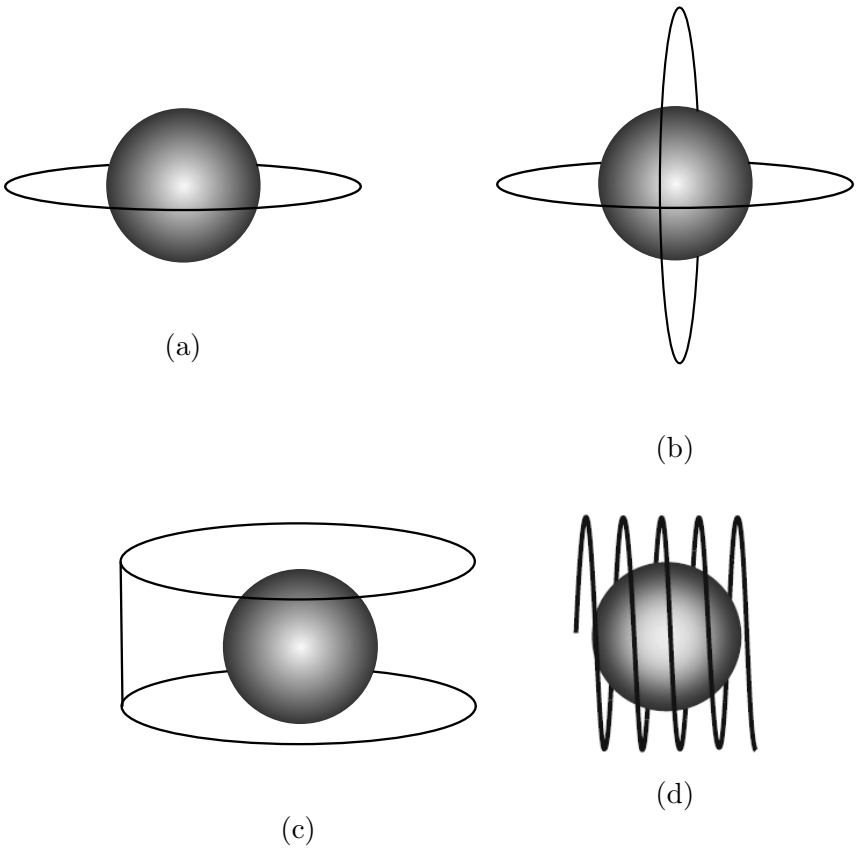

Figure 3.2: Cone-beam source courves: (a) circle, (b) twin circles in orthogonal planes, (c) two parallel circles joined by a line segment, (d) circular helix.

Note that even if the source curve Γ satisfies Tuy's first condition, it may or may not satisfy the second condition for each pair $(x, \beta) \in \Omega \times \mathbb{S}^2$. The second condition of Tuy fails when there exists $\lambda \in \Lambda$ such that $\langle x, \beta \rangle = \langle s(\lambda), \beta \rangle$, but $\langle s'(\lambda), \beta \rangle = 0$. This means that the plane intersecting a point $x \in \Omega$ goes through a cone-beam source $s(\lambda) \in \Gamma$, but the plane is tangent to the curve at this point of intersection. One cannot avoid checking the second condition as it leads to division by zero in Tuy's inversion formula (3.11). Tuy's completeness condition is fulfilled if, in addition to satisfying condition 1, for each tangential intersection $s(\lambda)$ with a

plane passing through $x \in \Omega$ orthogonal to $\beta \in \mathbb{S}^2$, one can find at least one $\tilde{\lambda} \in \Lambda$ such that $s(\tilde{\lambda})$ intersects with the same plane non-tangentially, i.e. $\langle s'(\tilde{\lambda}), \beta \rangle \neq 0$.

3.5.1 Twin-Circular Curve

We shall refer to the curve Γ consisting of two circles of radius $R > 0$ with the same center belonging to orthogonal planes as the *twin-circular curve* (see Figure 3.2b). The twin-circular curve is thus far the simplest cone-beam scanning curve which satisfies Tuy's condition.

Let us demonstrate that a twin-circular curve Γ satisfies Tuy's conditions if the radius $R > 0$ is large enough with respect to the object.. We may explicitly define $\Gamma = \Gamma_H \cup \Gamma_V$, with

$$\Gamma_H = \{s(\lambda) \in \mathbb{R}^3 : s(\lambda) = (R\cos\lambda, R\sin\lambda, 0), \lambda \in [0, 2\pi)\},$$
$$\Gamma_V = \{s(\lambda) \in \mathbb{R}^3 : s(\lambda) = (R\cos\lambda, 0, R\sin\lambda), \lambda \in [2\pi, 4\pi)\},$$

and $\Omega \equiv \operatorname{supp} f$ is the closed ball $||x|| \leq L$. Let us also denote by Π_H and Π_V the planes containing the circles Γ_H and Γ_V, respectively. Note that Γ is continuous on $[0, 4\pi)$ and differentiable everywhere on $[0, 4\pi)$, except for $\lambda \in \{0, 2\pi\}$. The finite number of singularities of Γ can be dismissed since such a set has Lebesgue measure zero, and Tuy's hypothesis requires Γ to be piecewise differentiable. Thus, the regularity conditions of Γ are fulfilled for the twin circles.

Tuy's first condition — every plane intersecting Ω must intersect Γ at least once — is satisfied if and only if the radius R of the two circles Γ_H and Γ_V satisfy $R > \sqrt{2}L$. This condition can be easily verified through geometric arguments.

To verify that Tuy's second condition is fulfilled for Γ, we show here that whenever a plane passing through some $x \in \Omega$ intersects the horizontal circle Γ_H, the intersection is almost always non-tangential, and when the intersection with Γ_H is tangential, one can obtain a non-tangential intersection on the vertical circle Γ_V. Suppose that for some $(x, \beta) \in \Omega \times \mathbb{S}^2$, there exists $\lambda = \lambda(x, \beta) \in [0, 2\pi)$ such that $\langle x, \beta \rangle = \langle s(\lambda(x, \beta)), \beta \rangle$. We write $x = (x_1, x_2, x_3)$ and $\beta(\theta, \phi) = (\cos\theta\cos\phi, \sin\theta\cos\phi, \sin\phi)$ with $\theta \in [0, 2\pi], \phi \in [-\pi/2, \pi/2]$. The planes orthogonal to $\beta(\cdot, \pm\pi/2)$ and passing through all points $x \in \Pi_H \cap \Omega$ intersect Γ in infinitely many locations on the horizontal circle Γ_H with $\langle s'(\lambda), \beta \rangle = 0$ and twice on the vertical circle Γ_V for $\lambda \in \{2\pi, 3\pi\}$ where $s'(\lambda)$ does not exist for $\lambda = 2\pi$. So for pairs of (x, β) in the set $(\Pi_H \cap \Omega) \times \{\beta(\cdot, \pm\pi/2)\}$, there exists only $\lambda = 3\pi$ such that $\langle x, \beta \rangle = \langle s(\lambda), \beta \rangle$ with $\langle s'(\lambda), \beta \rangle \neq 0$. For all other pairs $(x, \beta) \in \Omega \times \mathbb{S}^2$ when there exists a solution $\lambda = \lambda(x, \beta) \in [0, 2\pi)$ to the equation

$$\langle x, \beta(\theta, \phi) \rangle = \langle s(\lambda(x, \beta(\theta, \phi))), \beta(\theta, \phi) \rangle, \tag{3.16}$$

then λ solves the following equation

$$\cos\theta\cos\phi\cos\lambda + \sin\theta\cos\phi\sin\lambda = \frac{x_1\cos\theta\cos\phi + x_2\sin\theta\cos\phi + x_3\sin\phi}{R}. \tag{3.17}$$

Since $\phi \neq \pm\pi/2$ by assumption, dividing both sides of the equation above by $\cos\phi$ and applying a trigonometric identity we obtain

$$\cos(\lambda - \theta) = \frac{x_1\cos\theta + x_2\sin\theta + x_3\tan\phi}{R}. \tag{3.18}$$

Thus, we must have that

$$\left|\frac{x_1\cos\theta + x_2\sin\theta + x_3\tan\phi}{R}\right| < 1, \tag{3.19}$$

by (3.18) and the assumption that $R > \sqrt{2}L$. Let α be the unique angle in $[0, 2\pi)$ such that $\cos\alpha = \frac{x_1\cos\theta + x_2\sin\theta + x_3\tan\phi}{R}$. Then

$$\lambda = \theta \pm \alpha + k\pi \tag{3.20}$$

solves (3.16), where k is some integer such that λ falls within the interval $[0, 2\pi)$. We now have to check that λ given in (3.20) also satisfies $\langle s'(\lambda), \beta(\theta,\phi)\rangle \neq 0$. Note that $\langle s'(\lambda), \beta(\theta,\phi)\rangle = 0$ if and only if

$$-R\cos\theta\cos\phi\sin\lambda + R\sin\theta\cos\phi\cos\lambda = 0 \tag{3.21}$$

if and only if $\tan\theta = \tan\lambda$ if and only if $\theta = \lambda$. Using this in (3.20), we have $\alpha = 0$ or $\alpha = \pi$, which implies $\left|\frac{x_1\cos\theta + x_2\sin\theta + x_3\tan\phi}{R}\right| = 1$. But this cannot be true, by (3.19). Thus, $\langle s'(\lambda), \beta(\theta,\phi)\rangle \neq 0$ when $\lambda \in [0, 2\pi)$ solves $\langle x, \beta(\theta,\phi)\rangle = \langle s(\lambda(x, \beta(\theta,\phi))), \beta(\theta,\phi)\rangle$. By symmetry of the twin circles, it is trivial to realize that whenever planes intersecting Ω intersect the vertical circle Γ_V, the intersections are almost always non-tangential, and whenever a plane does intersect Γ_V tangentially, there exists one source position in Γ_H such that the intersection with the same plane is not tangential.

3.6 Stability of Cone-beam Reconstruction

Image reconstruction problems (from non-truncated or non-restricted data) are not *well-posed* in the sense of Hadamard, which means one of the following [43]

1. They cannot be solved.
2. They can be solved, but not uniquely.
3. They can be solved uniquely, but the solution does not depend continuously on the data.

When one of the above holds true, we call such a problem an *ill-posed* problem. The problem of reconstruction of a 2D density from its line integrals (2D Radon transform) has a unique solution, given by the 2D Radon inversion formula [41,43]. However, the problem is still ill-posed since the inversion procedure does not continuously depend on the projection data. The degree of ill-posedness of a reconstruction problem is usually analyzed by singular value decomposition (SVD) or Sobolev space estimates (see [43]). As the singular values of the 2D Radon transform decay at polynomial speed, the density reconstruction problem from the 2D Radon data is modestly ill-posed. For this reason, the discretized 2D Radon inversion can be implemented without serious numerical instability.

The non-truncated cone-beam reconstruction problem,

$$\text{recover } f, \quad \text{from cone-beam data } g = \mathcal{D}_s f, s \in \Gamma$$

is an ill-posed problem. We have seen that inversion formula (3.11) admits a unique solution if Tuy's conditions on the smooth and bounded source curve Γ are fulfilled.

Finch [17] gave estimates in scales of Sobolev spaces when the source curve Γ satisfies Tuy's conditions to give a degree of ill-posedness of the cone-beam reconstruction problem. Thus, one can conclude that if Γ satisfies Tuy's conditions, that is,

> every plane intersecting the support of f must intersect the source curve Γ transversally at least once,

then a stable reconstruction of f is possible from its cone-beam data, regardless of the exact inversion method used (other exact inversion formulas will be discussed in the next chapter). On the contrary, if the source curve Γ fails Tuy's conditions, i.e. if there is a plane that intersects $\operatorname{supp} f$ which does not pass through Γ, then the reconstruction procedure is unstable [17]. Such instabilities can result in severe artifacts in the digital implementations. For example, most popular cone-beam inversion algorithms use cone-beam data acquired from the circular trajectory, but artifacts in the vertical direction of the reconstructed images are prominent due to the fact that a circular curve fails Tuy's conditions. Various kinds of artifacts associated with the circular trajectory can be found in [35].

The conditions on the source curve discussed in Section 3.5 determines the stability of the cone-beam reconstruction problem. For a stable and exact inverse of the non-truncated cone-beam transform, the source curve Γ must meet Tuy's conditions. The same stability condition also applies for our proposed inversion algorithm of the truncated cone-beam transform in Chapter 6. Truncated cone-beam inversion procedures based on curves violating Tuy's conditions are severely unstable [32].

Chapter 4

The 3D Radon Transform

The Radon transform is one of the most important integral transforms in the field of computerized tomography. In two dimensions, it integrates densities over parallel lines and in three dimensions, it integrates densities over planes. Johan Radon's famous paper from 1917 [49] gave a very simple formula to invert the n-dimensional Radon transform. Radon's inversion formula is very useful in $\mathbb{R}^2$, as it allows one to invert the X-ray transform (X-ray transform and the Radon transform are identical in $\mathbb{R}^2$). In the early CT literature, three-dimensional Radon inversion formula lacked interest from CT researchers. Unlike the X-ray or cone-beam transform, there is no practical realistic means of collecting 3D Radon data (plane integrals of the density). Grangeat [19] first found a link between the cone-beam transform and the 3D Radon transform. One can derive a cone-beam inversion method as follows. First, convert cone-beam data to 3D Radon data. Next, use the 3D Radon inversion formula to recover the density function from the collected Radon data.

In this chapter, we first define the 3D Radon transform. Then we present the well-known Fourier Slice Theorem, and use this theorem to derive the inversion formula

of the 3D Radon transform. Finally, we give an efficient two-stage algorithm to numerically implement the 3D Radon inversion formula. The connection between the non-truncated cone-beam transform and the 3D Radon transform is presented in Chapter 5.

4.1 Definition

The Radon transform is an integral transform which maps a density function f on $\mathbb{R}^n$ to its integrals over hyperplanes in $\mathbb{R}^n$. The two-dimensional Radon transform integrates a function over lines in $\mathbb{R}^2$ and the three-dimensional Radon transform integrates a function over planes in $\mathbb{R}^3$. For the discussion, we only consider the 3D Radon transform and give some important concepts such as the Fourier Slice Theorem and the inversion formula. An in-depth study of the general n dimensional Radon transform can be found in [21,41,43]. Here, we will only concentrate on the 3D Radon transform.

We denote by $\mathbb{S}^2$ the unit sphere in $\mathbb{R}^3$ centered at the origin. In practice, one typically considers the 3D Radon transform of a real-valued function f that belongs to $C_c^\infty(\mathbb{R}^3)$, the class all of functions on $\mathbb{R}^3$ that are infinitely differentiable and compactly supported.

Definition 4.1.1. Let $\Pi(\omega, \rho) = \{x \in \mathbb{R}^3 : \langle x, \omega \rangle = \rho\}$, the plane orthogonal to $\omega \in \mathbb{S}^2$ and signed distance $\rho \in \mathbb{R}$ from the origin. For $f \in C_c^\infty(\mathbb{R}^3)$, the *3D Radon transform* $\mathcal{R}$ of f is defined as

$$\mathcal{R}f(\omega, \rho) = \int_{x \in \Pi(\omega,\rho)} f(x)\, d\Pi(x), \quad \omega \in \mathbb{S}^2, \rho \in \mathbb{R}, \tag{4.1}$$

where $d\Pi$ denotes the two-dimensional Lebesgue measure on the plane.

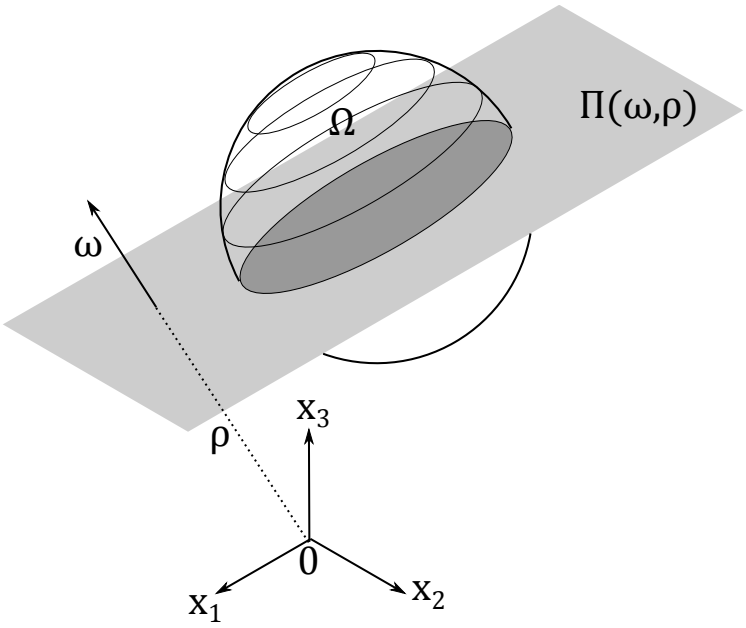

Figure 4.1: The 3D Radon transform integrates a density function f over a plane $\Pi(\omega, \rho)$ orthogonal to $\omega \in \mathbb{S}^2$ and having signed distance ρ from the origin.

The value $\mathcal{R}f(\omega, \rho)$ is simply the integral of f computed over the plane $\Pi(\omega, \rho)$ in $\mathbb{R}^3$. The Radon transform $\mathcal{R}f$ can be viewed as a function on the cylinder $\mathbb{S}^2 \times \mathbb{R}$. It is obvious that $\mathcal{R}f$ is an even function on $\mathbb{S}^2 \times \mathbb{R}$ verifying $\mathcal{R}f(-\omega, -\rho) = \mathcal{R}f(\omega, \rho)$ for all $(\omega, \rho) \in \mathbb{S}^2 \times \mathbb{R}$. Note that the smoothness of f implies the smoothness of $\mathcal{R}f$ on $\mathbb{S}^2 \times \mathbb{R}$ [43].

The Fourier transform of $f \in C_c^\infty(\mathbb{R}^3)$ and its inverse are defined by

$$\widehat{f}(\xi) = (2\pi)^{-3/2} \int_{\mathbb{R}^3} f(x)\, e^{-i\langle x, \xi \rangle}\, dx, \quad \xi \in \mathbb{R}^3, \tag{4.2}$$

$$f(x) = (2\pi)^{-3/2} \int_{\mathbb{R}^3} \widehat{f}(\xi)\, e^{i\langle \xi, x\rangle}\, dx, \quad x \in \mathbb{R}^3. \tag{4.3}$$

If g is a compactly supported smooth function on the cylinder $\mathbb{S}^2 \times \mathbb{R}$, i.e. $g \in C_c^\infty(\mathbb{S}^2 \times \mathbb{R})$, then the partial Fourier transform of g in the second argument is defined as

$$\widehat{g}(\omega, \sigma) = (2\pi)^{-1/2} \int_{-\infty}^{\infty} g(\omega, s)\, e^{-is\sigma}\, ds, \quad \sigma \in \mathbb{R}, \tag{4.4}$$

$$g(\omega, s) = (2\pi)^{-1/2} \int_{-\infty}^{\infty} \widehat{g}(\omega, \sigma)\, e^{i\sigma s}\, d\sigma, \quad s \in \mathbb{R}. \tag{4.5}$$

4.2 3D Fourier Slice Theorem

We begin with an important theorem in CT literature, known as the "Fourier Slice Theorem" which connects the Fourier Transform and the Radon transform. This theorem is also known as the "Central Slice Theorem" or the "Projection Theorem". Here we only present the 3D version of the theorem. The general case of the Fourier Slice Theorem can be found in [41, 43].

If f is smooth and compactly supported, then $\mathcal{R}f$ is a smooth function defined on $\mathbb{S}^2 \times \mathbb{R}$ and it has a well-defined partial Fourier transform. By (4.4), the partial Fourier transform $\mathcal{F}(\mathcal{R}f)_\omega$ of $\mathcal{R}f$ is defined as

$$\mathcal{F}(\mathcal{R}f)_\omega(\sigma) = (2\pi)^{-1/2} \int_{-\infty}^{\infty} \mathcal{R}f(\omega, \rho)\, e^{-i\rho\sigma}\, d\rho, \quad \omega \in \mathbb{S}^2, \sigma \in \mathbb{R}. \tag{4.6}$$

Theorem 4.2.1 (3D Fourier Slice Theorem)**.** *Let f be a smooth and compactly sup-*

ported function on $\mathbb{R}^3$*. Then for* $\omega \in \mathbb{S}^2, \sigma \in \mathbb{R}$*,*

$$\mathcal{F}(\mathcal{R}f)_\omega(\sigma) = 2\pi \widehat{f}(\sigma\omega). \tag{4.7}$$

Proof. See [21, 41]. □

In equation (4.7), $\widehat{f}$ denotes the 3D Fourier transform of f. The theorem basically states that for a fixed unit vector $\omega \in \mathbb{S}^2$, the partial Fourier transform of the Radon transform is equal to the "slice" of the 3D Fourier transform of f (apart from a multiplicative factor 2π), where the slice is precisely the line passing through the origin with direction ω in the Fourier domain.

4.3 Radon's 3D Inversion Formula

Here we present the inversion formula for the 3D Radon transform, derived by Johan Radon in his famous paper [49] in 1917. For a compactly supported smooth function f on $\mathbb{R}^3$, the 3D Radon transform $\mathcal{R}$ maps f to its integrals over planes in $\mathbb{R}^3$.

The three-dimensional Radon inversion formula is given as a backprojection of the second derivative of the Radon transform with respect to its second variable ρ. For a function g defined on $\mathbb{S}^2 \times \mathbb{R}$ and $x \in \operatorname{supp} f$, the *3D backprojection* operator $\mathcal{R}^\sharp$ is defined as

$$\mathcal{R}^\sharp g(x) = \int_{\omega \in \mathbb{S}^2} g(\omega, \langle \omega, x \rangle)\, dQ(\omega), \tag{4.8}$$

where dQ denotes the infinitesimal area element on the unit sphere $\mathbb{S}^2$. Thus, for $g = \mathcal{R}f$, $\mathcal{R}^\sharp g(x)$ is the average value of all integrals of f on planes passing through x [43]. In general, the backprojection operator is a mapping from the space of integrable

functions on the cylinder $\mathbb{S}^{n-1} \times \mathbb{R}$ to the space of integrable functions on $\mathbb{R}^n$

Theorem 4.3.1 (3D Radon Inversion Formula)**.** *Let $f \in C_c^2(\mathbb{R}^3)$. Then for all $x \in \operatorname{supp} f$,*

$$f(x) = -\frac{1}{8\pi^2} \int_{\mathbb{S}^2} \frac{\partial^2}{\partial \rho^2} \mathcal{R}f(\omega, \rho)\Big|_{\rho=\langle x,\omega\rangle} dQ(\omega). \tag{4.9}$$

That is, $f(x) = -\frac{1}{8\pi^2}\mathcal{R}^\sharp(\frac{\partial^2}{\partial\rho^2}\mathcal{R}f(\omega, \langle\omega, x\rangle))$.

Proof. Denote $\widetilde{S}$ to be any half of the unit sphere $\mathbb{S}^2$. The Fourier inversion formula in spherical coordinates reads

$$f(x) = (2\pi)^{-3/2} \int_{\widetilde{S}} \int_{\mathbb{R}} \sigma^2 \widehat{f}(\sigma\omega)\, e^{i\sigma\langle x,\omega\rangle}\, d\sigma\, dQ(\omega). \tag{4.10}$$

Using the Fourier Slice Theorem (4.7), we get

$$\begin{aligned} f(x) &= (2\pi)^{-2} \int_{\widetilde{S}} \int_{\mathbb{R}} \sigma^2 (2\pi)^{-1/2} \widehat{\mathcal{R}f}(\omega, \sigma)\, e^{i\sigma\langle x,\omega\rangle}\, d\sigma\, dQ(\omega) && (4.11)\\ &= -(2\pi)^{-2} \int_{\widetilde{S}} \frac{\partial^2}{\partial\rho^2} \mathcal{R}f(\omega, \rho)\Big|_{\rho=\langle x,\omega\rangle} dQ(\omega) && (4.12)\\ &= -\frac{1}{8\pi^2} \int_{\mathbb{S}^2} \frac{\partial^2}{\partial\rho^2} \mathcal{R}f(\omega, \rho)\Big|_{\rho=\langle x,\omega\rangle} dQ(\omega). && (4.13) \end{aligned}$$

Note that we have used above the fact that the inverse Fourier transform of $\sigma^2\widehat{h}$ is $-h''$ for any twice differentiable function h on $\mathbb{R}$ that is absolutely integrable. □

In equation (4.9), the differential operator $\frac{\partial^2}{\partial\rho^2}$ applies to the second argument of $\mathcal{R}f$. Radon's inversion formula tells us that $f(x)$ can be recovered by backprojection of $(\mathcal{R}f)'' \equiv \frac{\partial^2}{\partial\rho^2}\mathcal{R}f$. That is, $f(x)$ is just an average of $(\mathcal{R}f)''$ over all planes passing through x. The density f can be reconstructed at a point x from the plane integral

values of f in an infinitesimal neighborhood of all planes passing through x. For this reason, the 3D Radon inversion formula is said to be *local*.

4.4 Numerical Implementation of the 3D Radon Inversion

In this section, we explain to how discretize the 3D Radon inversion formula (4.9) to implement a computationally efficient algorithm to reconstruct a 3D density on a discrete 3D grid from a set of sampled Radon data.

Assume that the smooth 3D density $f(x, y, z)$ is supported on Ω, the closed ball of radius r centered at the origin in $\mathbb{R}^3$. In this case, the support of $\mathcal{R}f$ is $\mathbb{S}^2 \times [-r, r]$. Thus, in order to fully reconstruct f on Ω by (4.9), one needs to know $\mathcal{R}f(\omega, \rho)$ for all $\omega \in \mathbb{S}^2$ and $\rho \in [-r, r]$. This is a sufficient condition for reconstruction of f on its support Ω via Radon's inversion formula. We represent $\omega \in \mathbb{S}^2$ in a spherical coordinate system as

$$\omega = \omega(\theta, \phi) = (\cos\theta \sin\phi,\, \sin\theta \sin\phi,\, \cos\phi), \quad 0 \le \theta \le 2\pi,\, 0 \le \phi \le \pi. \tag{4.14}$$

Since $\mathcal{R}f$ is an even function on $\mathbb{S}^2 \times \mathbb{R}$, it is sufficient to know $\mathcal{R}f$ on any hemisphere $\widetilde{S}$. By convention, we choose $\widetilde{S} = \{\omega(\theta, \phi) : 0 \le \theta \le \pi,\, 0 \le \phi \le \pi\}$. Defining the following

$$K(\theta, \phi, \rho) \equiv \mathcal{R}f(\omega(\theta, \phi), \rho)$$
$$K''(\theta, \phi, \rho) \equiv \frac{\partial^2}{\partial \rho^2} \mathcal{R}f(\omega(\theta, \phi), \rho)$$

and observing that $\langle (x,y,z), \omega(\theta,\phi)\rangle = \sin\phi(x\cos\theta + y\sin\theta) + z\cos\phi$, the 3D Radon inversion formula (4.9) becomes the following double integral

$$f(x,y,z) = -\frac{1}{4\pi^2}\int_0^\pi \int_0^\pi K''(\theta,\phi,\rho(x,y,z,\theta,\phi))\,\sin\phi\,d\phi\,d\theta, \tag{4.15}$$

where $\rho(x,y,z,\theta,\phi) = \sin\phi(x\cos\theta + y\sin\theta) + z\cos\phi$.

In practice, one usually considers recovering the values of f on a discrete grid inside the cube $[-L,L]^3$, where $L > r$. Note that the cube actually contains Ω, the support of f. Define a rectangular 3D grid consisting of points (x_i, y_j, z_k), where N is even and

$$x_i = \left(\frac{2L}{N}\right) i, \quad i = -\frac{N}{2},\ldots,\frac{N}{2}, \tag{4.16}$$

$$y_j = \left(\frac{2L}{N}\right) j, \quad j = -\frac{N}{2},\ldots,\frac{N}{2}, \tag{4.17}$$

$$z_k = \left(\frac{2L}{N}\right) k, \quad k = -\frac{N}{2},\ldots,\frac{N}{2}. \tag{4.18}$$

The sampled values $f(x_i, y_j, z_k)$ define a 3D discrete image of size $N \times N \times N$. We suppose that the 3D Radon data K'' are available on a spherical grid of size $N_\theta \times N_\phi \times N_\rho$, consisting of points $(\theta_m, \phi_n, \rho_s)$, where

$$\theta_m = \left(\frac{\pi}{N_\theta}\right) m, \quad m = 1,\ldots,N_\theta, \tag{4.19}$$

$$\phi_n = \left(\frac{\pi}{N_\phi}\right) n, \quad n = 1,\ldots,N_\phi, \tag{4.20}$$

$$\rho_s = \left(\frac{2L}{N_\rho}\right) s, \quad s = -\frac{N_\rho}{2},\ldots,\frac{N_\rho}{2}. \tag{4.21}$$

Note that proper sampling of Radon data is necessary to obtain an accurate recon-

struction. A function defined on $\mathbb{R}^3$ is said to be *band-limited* with *bandwith* $E > 0$ if its Fourier transform vanishes outside the closed ball of radius E centered at the origin. Following Natterer [43], for a 3D density f supported in a ball $||x|| < L$ with bandwidth $E > 0$, one should sample at least $(LE)^2/2$ directions, with stepsizes $\Delta\theta \leq \pi/(LE), \Delta\phi \leq \pi/(LE)$.

One can directly approximate the 3D Radon inversion formula to reconstruct $f(x_i, y_j, z_k)$ by replacing the 2D integral in (4.15) by the double sum:

$$-\frac{1}{4\pi^2}\sum_{m=1}^{N_\theta}\sum_{n=1}^{N_\phi} K''(\theta_m, \phi_n, \rho(x, y, z, \theta_m, \phi_n)) \sin\phi_m, \tag{4.22}$$

where $\rho(x, y, z, \theta_m, \phi_n) = \sin\phi_n(x_i \cos\theta_m + y_j \sin\theta_m) + z_k \cos\phi_n$. Note that 3D interpolation will be necessary to obtain the values of $K''(\theta_m, \phi_n, \rho(x, y, z, \theta_m, \phi_n))$ from the acquired Radon data on the spherical grid, and this can be a computationally demanding task. Ignoring the computational complexity of 3D interpolation, the direct method computes a double sum that requires roughly N^2 operations (assuming $N_\theta = N_\phi = N$) to reconstruct the density at one point. Thus, N^3 points can be reconstructed by the direct method in approximately $N^3 \times N^2 = N^5$ operations. When N is large, we see that approximation of the 3D Radon inversion formula (4.15) by the direct method can be computationally demanding and time consuming.

4.4.1 Two-stage Algorithm

We now present an efficient method to implement the 3D Radon inversion formula (4.15). Marr *et al.* [39] first showed that the 3D Radon inversion formula (4.15) can be implemented more efficiently than by the direct method through splitting the 2D

integrals into two 1D integrals. This method is commonly referred to as the "Two-stage Algorithm".

Let us denote $f_z(x, y) = f(x, y, z)$ and $Q(\theta, \phi, \rho) = K''(\phi, \theta, \rho) \cdot \sin\phi$. The double integral in (4.15) can be decomposed into two successive integrals:

$$P(t, z, \theta) = \frac{1}{2\pi} \int_0^{\pi} Q(\theta, \phi, \rho)\Big|_{\rho = t\sin\phi + z\cos\phi} \quad d\phi, \tag{4.23}$$

$$f_z(x, y) = -\frac{1}{2\pi} \int_0^{\pi} P(t, z, \theta)\Big|_{t = x\cos\theta + y\sin\theta} \quad d\theta. \tag{4.24}$$

The 1D integrals above can be identified as 2D backprojections in parallel-beam geometry. For each θ, the first integral (4.23) can be seen as the 2D backprojection of sinogram data $Q(\theta, \phi, \rho)$ on the vertical plane $x\cos\theta + y\sin\theta = 0$ that generates a 2D density $P(t, z, \theta)$ on the tz-plane, where the t-axis is parallel to the unit vector $(\cos\theta, \sin\theta, 0)$. For each z, the second integral (4.24) can be viewed as the 2D backprojection of sinogram data $P(t, z, \theta)$ that obtains a 2D density $f_z(x, y)$ on the plane through z, parallel to the xy-plane. A number of computationally efficient algorithms for 2D backprojection can be found in [26]. We present step-by-step instructions to implement the two-stage algorithm next.

Algorithm: Two-stage Algorithm for 3D Radon Inverison

Data: 3D Radon data K'' sampled at the points $(\theta_m, \phi_n, \rho_s)$ for $m = 1, \ldots, N_\theta$, $n = 1, \ldots, N_\phi$, $s = 1, \ldots, N_\rho$ as given in equations (4.19) - (4.21).

Result: Reconstructed values of f at the points (x_i, y_j, z_k) for $i = 1, \ldots, N$, $j = 1, \ldots, N$, $k = 1, \ldots, N$. The reconstructed discretized 3D density is obtained as stacks of discretized 2D densities $f_{z_k}(x_i, y_j)$.

Sample t from the interval $[-L, L]$ in the same way as ρ:

$$t_\ell = \left(\frac{2L}{N_\rho}\right)\ell, \quad \ell = -\frac{N_\rho}{2}, \ldots, \frac{N_\rho}{2}.$$

Step 1: For each $m = 1, \ldots, N_\theta$, backproject the 2D sinogram data $Q(\theta_m, \phi_n, \rho_s)$ on the vertical planes $x\cos\theta_m + y\sin\theta_m = 0$ to generate a stack of 2D images $P(t_\ell, z_k, \theta_m)$ indexed by m.

Step 2: For $k = 1, \ldots, N$, backproject the 2D sinogram data $P(t_\ell, z_k, \theta_m)$ on the horizontal plane $z = z_k$ to generate a stack of discretized 2D densities $f_{z_k}(x_i, y_j)$.

4.4.2 Computational Complexity

To determine the computational complexity of the two-stage algorithm, let us suppose that the 3D volume we are interested in reconstructing is of size N^3 and the parameters of the Radon data are sampled at N points in their proper domains using the sampling scheme described earlier. Step 1 of the algorithm performs N backprojections in 2D. It can be shown that each backprojection algorithm requires N^3 operations [26]. Thus, Step 1 can be completed with N^4 operations. Step 2 requires

N backprojections in 2D, so step 2 is also done with N^4 operations. Therefore, the two-step algorithm can be done by $N^4 + N^4 = 2N^4$ operations.

We see that the two-step algorithm reduces the computation required for the direct method by a factor of $N/2$. In addition, it should be noted that the direct method requires 3D interpolation that can be computationally intensive and time consuming, whereas the two-stage algorithm requires simple 1D linear interpolations for its 2D backprojection steps, which can be calculated quite rapidly.

Chapter 5

Practical Inversion Formulas for the Non-truncated Cone-beam Transform

We have already outlined the theory of non-truncated cone-beam reconstruction following the framework of Tuy [59] in Chapter 3. However, Tuy's cone-beam-inversion formula in its original form is purely theoretical and cannot be implemented numerically for practical use. In this chapter, we present the very first exact cone-beam reconstruction formula to be numerically implemented, due to Grangeat [20]. Grangeat's formula deals with acquisition from sources on a very generic piecewise smooth curve satisfying Tuy's condition 1 (see Section 3.5). To this day, Grangeat's formula still serves as one of the few exact cone-beam reconstruction methods which are stable and numerically implementable. In fact, several cone-beam-reconstruction formulas were developed by further modification of Grangeat's original formula. One

of those variant inversion formulas, due to Defrise and Clack [13] and Kudo and Saito [33], is also presented here.

5.1 Link between the Cone-beam Transform and the 3D Radon Transform

Grangeat [19,20] introduced a new formula which relates the first radial derivative of the 3D Radon transform of a density f on $\mathbb{R}^3$ and its cone-beam transform. Grangeat's formula assumes the following about the density f and the source curve Γ:

1. The 3D density f belongs the class $C_c^k(\mathbb{R}^3)$, where $k \geq 2$. That is, the compactly supported density f is at least twice differentiable and all of its partial derivatives up to that order are compactly supported.

2. Every plane that intersects the support of f must intersect the curve Γ at least once.

The second condition of Grangeat is equivalent to Tuy's condition, except the intersection of the plane and the trajectory is not required to be non-tangential, as it is required in Tuy's Condition 2.

Recall that the cone-beam transform $\mathcal{D}_s f$ of a function $f : \mathbb{R}^3 \to \mathbb{R}$ of compact support is defined as

$$\mathcal{D}_s f(\beta) = \int_0^\infty f(s + t\beta)\, dt,$$

where $s \in \mathbb{R}^3$ is the source position and $\beta \in \mathbb{S}^2$ is the direction of the cone-beam ray originating from s.

Theorem 5.1.1 (Grangeat [19, 20]). *Let $f \in C_c^k(\mathbb{R}^3), k \geq 2$ and let Γ be a smooth curve in $\mathbb{R}^3$ satisfying Tuy's condition 1. Then for $\omega \in \mathbb{S}^2$, the 3D Radon transform $\mathcal{R}f$ of f verifies*

$$\frac{\partial}{\partial \rho} \mathcal{R}f(\omega, \rho)\bigg|_{\rho=\langle s,\omega\rangle} = \int_{\beta \in \omega^\perp \cap \mathbb{S}^2} \nabla_\omega \mathcal{D}_s f(\beta)\, d\beta \tag{5.1}$$

where ∇_ω stands for the directional derivative in the direction $\omega \in \mathbb{S}^2$ and $\omega^\perp \cap \mathbb{S}^2$ is the great circle on $\mathbb{S}^2$ with axis of rotation ω.

Proof. See [20]. □

Remark 5.1.2. The left-hand side of (5.1) represents the first derivative of $\mathcal{R}f$ with respect to the radial parameter ρ, computed on the plane $\Pi(\omega, \rho)$ that contains a source position $s \in \Gamma$. The symbol $\nabla_\omega \mathcal{D}_s$ represents the directional derivative of $\mathcal{D}_s f$ in the direction $\omega \in \mathbb{S}^2$. The right-hand side of (5.1) is a line integral of $\nabla_\omega \mathcal{D}_s f$ computed over $\omega^\perp \cap \mathbb{S}^2$, the great circle on the unit sphere $\mathbb{S}^2$ with axis of rotation ω. Note that $\omega^\perp$ denotes the subspace of $\mathbb{R}^3$ that is orthogonal to ω. The symbol $d\beta$ denotes the infinitesimal arclength on the circle $\omega^\perp \cap \mathbb{S}^2$.

5.2 Grangeat's Inversion Method

Grangeat's fundamental relation (5.1) of the first derivative of the 3D Radon transform and the cone-beam transform of a function f can be used to to invert the cone-beam transform. Differentiating both sides of (5.1) with respect to ρ, we get

$$\frac{\partial^2}{\partial \rho^2} \mathcal{R}f(\omega, \rho)\bigg|_{\rho=\langle s,\omega\rangle} = \frac{\partial}{\partial \rho} \left(\int_{\beta \in \omega^\perp \cap \mathbb{S}^2} \nabla_\omega \mathcal{D}_s f(\beta)\, d\beta \right) \bigg|_{\rho=\langle s,\omega\rangle}. \tag{5.2}$$

For any $x \in \operatorname{supp} f$ and $\omega \in \mathbb{S}^2$, Tuy's condition gives us at least one source position $s = s(x,\omega) \in \Gamma$ such that $\langle x,\omega\rangle = \langle s(x,\omega),\omega\rangle$. Using this substitution and the identity (5.2) into the 3D Radon inversion formula (4.9), we obtain Grangeat's cone-beam inversion formula:

$$f(x) = -\frac{1}{8\pi^2}\int_{\mathbb{S}^2}\frac{\partial}{\partial\rho}\left(\int_{\beta\in\omega^\perp\cap\mathbb{S}^2}\nabla_\omega\mathcal{D}_{s(x,\omega)}f(\beta)\,d\beta\right)\Bigg|_{\rho=\langle x,\omega\rangle} dQ(\omega). \tag{5.3}$$

An exact reconstruction of a smooth compactly supported density f is possible by the formula above as long as the source curve Γ fulfills Tuy's completeness conditions.

5.3 Cone-beam Inversion by Filtered Backprojection

For a closed and bounded piecewise smooth curve Γ in $\mathbb{R}^3$, the cone-beam transform $\mathcal{D}$ is a linear mapping from $L^2(\mathbb{R}^3)$ to $L^2(\Gamma\times\mathbb{S}^2)$. The adjoint operator D^* of $\mathcal{D}$ linearly maps a function from the space $L^2(\Gamma\times\mathbb{S}^2)$ to a function in $L^2(\mathbb{R}^3)$. The adjoint D^* is commonly referred to as the *cone-beam backprojection* in the literature. As detailed in [37], the cone-beam backprojection operator $\mathcal{D}^*$ is defined by the formula

$$\mathcal{D}^*g(x) = \int_{\lambda\in\Lambda}\frac{1}{||x-s(\lambda)||^2}\,g\left(\lambda,\frac{x-s(\lambda)}{||x-s(\lambda)||}\right)d\lambda, \quad x\in\mathbb{R}^3, \tag{5.4}$$

for all $g \in L^2(\Gamma\times\mathbb{S}^2)$.

An exact or approximate cone-beam inversion formula is said to be of type *filtered backprojection (FBP)* if it can be expressed as a backprojection of filtered cone-beam data. Suppose f is a compactly supported smooth density function. In operator

notation, any filtered backprojection formula is of the form

$$F = \mathcal{D}^*(\mathcal{D}f * \psi),$$

where $\mathcal{D}f * \psi$ is the convolution of $\mathcal{D}f$ by an appropriate filtering function ψ in $L^2(\Gamma \times \mathbb{S}^2)$. The choice of the source curve Γ determines whether F is *exactly* equal to f, for all $x \in \operatorname{supp} f$. Obviously, if Γ does not fulfill Tuy's condition, the reconstruction F computed by a FBP formula is not exactly equal to f. For this reason, the most popular cone-beam FBP reconstruction method due to Feldkamp *et al.* [**?**] delivers only an approximate reconstruction F of f, since the circular trajectory Γ fails to meet Tuy's conditions.

Grangeat's original inversion method (5.3) can be used to exactly recover a compactly supported and twice differentiable density f as long as the source curve Γ satisfies Tuy's condition 1. However, Grangeat's inversion formula is not a cone-beam FBP type formula. We proceed to show that Grangeat's original inversion formula can be modified by appropriate change of variables to obtain an exact cone-beam FBP inversion formula.

5.3.1 Derivation of an Exact FBP Formula

Grangeat's fundamental relation can be used to derive a filtered backprojection type inversion formula for the non-truncated cone-beam transform. This derivation is due to Defrise and Clack [13]. Let Γ be a curve which satisfies Tuy's conditions, and let $s(\lambda)$ be the parametrization of Γ with $\lambda \in \Lambda$, where Λ is a finite union of intervals in

$\mathbb{R}$. Let us write the cone-beam projection data as

$$g(\lambda, \beta) = \mathcal{D}f(s(\lambda), \beta) = \int_0^\infty f(s(\lambda) + t\beta)\, dt, \tag{5.5}$$

where $\beta \in \mathbb{S}^2$ and $\lambda \in \Lambda \subset \mathbb{R}$. Define the intermediary function $G(\lambda, \omega)$ of cone-beam transform g:

$$G(\lambda, \omega) = \int_{\beta \in \mathbb{S}^2 \cap \omega^\perp} \nabla_\omega g(\lambda, \beta)\, d\beta, \quad \lambda \in \Lambda, \omega \in \mathbb{S}^2. \tag{5.6}$$

Here, ∇_ω stands for directional derivative in the direction $\omega \in \mathbb{S}^2$ acting on the second argument of g, and $\mathbb{S}^2 \cap \omega^\perp$ is the great circle on $\mathbb{S}^2$ with axis of rotation ω. The integral $G(\lambda, \omega)$ is identical to the right-hand side of Grangeat's formula (5.1). For $\lambda \in \Lambda, \omega \in \mathbb{S}^2$, from Grangeat's formula we have

$$G(\lambda, \omega) = \frac{\partial}{\partial \rho} \mathcal{R}f(\omega, \langle s(\lambda), \omega \rangle). \tag{5.7}$$

Note here that the derivative of the 3D Radon transform $\mathcal{R}f$ is computed on the plane orthogonal to ω, passing through a source point $s(\lambda)$.

Recall from earlier that for any $x \in \operatorname{supp} f$, $f(x)$ can be reconstructed via Radon's 3D inversion formula:

$$f(x) = -\frac{1}{4\pi^2} \int_{\widetilde{S}} \frac{\partial^2}{\partial \rho^2} \mathcal{R}f(\omega, \rho) \Big|_{\rho = \langle x, \omega \rangle} dQ(\omega), \tag{5.8}$$

where $\widetilde{S}$ denotes any hemisphere of $\mathbb{S}^2$ and dQ denotes the infinitesimal surface area on $\mathbb{S}^2$. For any function $\psi \in \mathcal{S}(\mathbb{R})$, one has

$$\psi'(\rho_0) = \langle \delta'(\rho_0 - \rho), h(\rho) \rangle = \int_{-\infty}^\infty \delta'(\rho_0 - \rho) h(\rho)\, d\rho, \tag{5.9}$$

by the definition of the distribution δ'. As we have mentioned in Chapter 3 the integral involving the derivative of the delta distribution is purely formal. As $f \in C_c^\infty(\mathbb{R}^3)$, we have $\mathcal{R}f(\omega, \cdot) \in \mathcal{S}(\mathbb{R})$, and the 3D Radon inversion formula can also be written as

$$f(x) = -\frac{1}{4\pi^2} \int_{\widetilde{S}} \int_{-\infty}^{\infty} \delta'(\rho - \langle x, \omega \rangle) \, \frac{\partial}{\partial \rho} \mathcal{R}f(\omega, \rho) \Big|_{\rho = \langle x, \omega \rangle} d\rho \, dQ(\omega). \tag{5.10}$$

Using (5.7), we have

$$f(x) = -\frac{1}{4\pi^2} \int_{\widetilde{S}} \int_{-\infty}^{\infty} \delta'(\rho - \langle x, \omega \rangle) \, G(\lambda(\omega, \rho), \omega) \, d\rho \, dQ(\omega), \tag{5.11}$$

where $\lambda(\omega, \rho)$ is any solution to $\langle s(\lambda), \omega \rangle = \rho$. In other words, the source point $s(\lambda(\omega, \rho)) \in \Gamma$ is on the plane $\langle x, \omega \rangle = \rho$. To write the formula above in the form of a cone-beam backprojection formula, for each $\omega \in \mathbb{S}^2$, we replace the inner integral over ρ as an integral over λ by writing $\rho = \langle s(\lambda), \omega \rangle$. But the mapping $\rho = \langle s(\lambda), \omega \rangle$ (with $\omega \in \mathbb{S}^2$ fixed) is not one-to-one as the plane $\Pi(\omega, \rho)$ may intersect Γ at more that one point. To handle the redundancy, a smooth function $M(\omega, \lambda)$ can be introduced, satisfying the normalization condition

$$\sum_{k=1}^{n(\omega, \rho)} M(\omega, \lambda_k) = 1, \tag{5.12}$$

where $n(\omega, \rho)$ denotes the number of intersections between the plane $\Pi(\omega, \rho)$ and the curve Γ, and $\lambda_1, \ldots, \lambda_{n(\omega,\rho)} \in \Lambda$ are the solutions to $\rho = \langle s(\lambda), \omega \rangle$. An obvious choice for the function $M(\omega, \lambda)$ which satisfies the normalization condition is

$$M(\omega, \lambda) = \frac{1}{n(\omega, \langle s(\lambda), \omega \rangle)}, \tag{5.13}$$

where $n(\omega, \langle s(\lambda), \omega \rangle)$ denotes the number of intersections between the source curve Γ and the plane Π passing through $s(\lambda)$ and orthogonal to ω. However, this trivial choice of M has many discontinuities. In the paper [13], one requires that $M(\omega, \lambda)$ be continuously differentiable in both λ and ω in order to derive a stable reconstruction formula. An appropriate weighting function M is given by [13]

$$M(\omega, \lambda) = \frac{|\langle s'(\lambda), \omega \rangle|^m c(\lambda)}{\sum_{k=1}^{n(\omega, \langle s(\lambda), \omega \rangle)} |\langle s'(\lambda_k), \omega \rangle|^m c(\lambda_k)}, \tag{5.14}$$

where m is a positive integer and $c : \Lambda \to \mathbb{R}$ is a smooth function equal to one everywhere, except near the boundaries of the interval Λ. This choice of M is C^1 in both ω and λ when $m > 2$ (see [13]).

It is proved in [13] that

$$\int_{-\infty}^{\infty} G(\lambda(\omega, \rho), \omega)\, \delta'(\rho - \langle x, \omega \rangle)\, d\rho = \int_{\Lambda} |\langle s'(\lambda), \omega \rangle|\, M(\omega, \lambda)\, G(\lambda, \omega)\, \delta'(\langle x - s(\lambda), \omega \rangle)\, d\lambda, \tag{5.15}$$

where M is an appropriate smooth weight function satisfying (5.12). Using this equality in (5.11), we obtain

$$f(x) = -\frac{1}{4\pi^2} \int_{\widetilde{S}} \int_{\Lambda} |\langle s'(\lambda), \omega \rangle|\, M(\omega, \lambda)\, G(\lambda, \omega)\, \delta'(\langle x - s(\lambda), \omega \rangle)\, d\lambda\, dQ(\omega). \tag{5.16}$$

With the assumption that f has a compact support, the integrand above is absolutely integrable. Thus, we may change the order of integration above and obtain

$$f(x) = -\frac{1}{4\pi^2} \int_{\Lambda} \int_{\widetilde{S}} |\langle s'(\lambda), \omega \rangle|\, M(\omega, \lambda)\, G(\lambda, \omega)\, \delta'(\langle x - s(\lambda), \omega \rangle)\, dQ(\omega)\, d\lambda. \tag{5.17}$$

Note that the inner product can be written as

$$\langle x - s(\lambda), \omega \rangle = ||x - s(\lambda)|| \left\langle \frac{x - s(\lambda)}{||x - s(\lambda)||}, \omega \right\rangle. \tag{5.18}$$

Using the scaling property of the δ' distribution [5]:

$$\delta'(at) = \frac{\delta'(t)}{a^2}, \quad \text{for all } a > 0, \tag{5.19}$$

we obtain

$$\begin{aligned} \delta'(\langle x - s(\lambda), \omega \rangle) &= \delta' \left(||x - s(\lambda)|| \left\langle \frac{x - s(\lambda)}{||x - s(\lambda)||} \right\rangle \right) \\ &= ||x - s(\lambda)||^{-2} \delta' \left(\left\langle \frac{x - s(\lambda)}{||x - s(\lambda)||} \right\rangle \right). \end{aligned}$$

Defining g^F for $\lambda \in \Lambda$ and $\beta \in \mathbb{S}^2$ as follows

$$g^F(\lambda, \beta) = -\frac{1}{4\pi^2} \int_{\mathbb{S}^2/2} |\langle s'(\lambda), \omega \rangle| \, M(\omega, \lambda) \, G(\lambda, \omega) \, \delta'(\langle \beta, \omega \rangle) \, d\mathbb{S}^2(\omega), \tag{5.20}$$

and plugging this into equation (5.17), we arrive at the filtered-backprojection cone-beam inverison formula:

$$f(x) = \int_{\lambda \in \Lambda} \frac{1}{||x - s(\lambda)||^2} \, g^F \left(\lambda, \frac{x - s(\lambda)}{||x - s(\lambda)||} \right) \, d\lambda. \tag{5.21}$$

This formula was derived by Defrise and Clack [13]. A similar formula was derived by Kudo and Saito [33]. However, the formula presented in [33] involves a discontinuous weighting function M (similar to (5.13)), which may lead to numerical instability.

The filtered-backprojection cone-beam inversion formula is summarized as a the-

orem below.

Theorem 5.3.1 (Cone-beam FBP)**.** *Let $f \in C_c^\infty(\mathbb{R}^3)$ and let $\Gamma = \{s(\lambda) \in \mathbb{R}^3 : \lambda \in \Lambda\}$ be a source curve satisfying Tuy's conditions. Then for any $x \in \operatorname{supp} f$,*

$$f(x) = \int_{\lambda\in\Lambda} \frac{1}{||x - s(\lambda)||^2}\, g^F\left(\lambda, \frac{x - s(\lambda)}{||x - s(\lambda)||}\right) d\lambda, \tag{5.22}$$

$$g^F(\lambda, \beta) = -\frac{1}{4\pi^2} \int_{\widetilde{S}} |\langle s'(\lambda), \omega\rangle|\, M(\omega, \lambda)\, G(\lambda, \omega)\, \delta'(\langle \beta, \omega\rangle)\, dQ(\omega), \tag{5.23}$$

$$G(\lambda, \omega) = \int_{\beta\in\mathbb{S}^2\cap\omega^\perp} \nabla_\omega g(\lambda, \beta)\, d\beta, \tag{5.24}$$

where $M(\omega, \lambda)$ is a smooth weight function, as given in (5.14)*.*

5.4 Numerical Feasibility of the Inversion Formulas from Non-truncated Cone-beam Data

We have presented three exact cone-beam inversion formulas from non-truncated data: Tuy's formula, Grangeat's formula, and the cone-beam filtered-backprojection formula. With the assumption that the cone-beam sources are located on a curve Γ fulfilling Tuy's conditions, all three of the formulas deliver exact reconstruction analytically. However, these formulas are very different in nature when it comes to numerical implementation. In fact, only two of the formulas have been implemented numerically.

Tuy's formula in its original form is not numerically implementable. One reason for this is that it requires the Fourier transform of a tempered distribution, followed by a differentiation with respect to the source parameter. Regularizing the divergent integral of Fourier transform of $\mathcal{D}_s f$ can produce heavy artifacts in the reconstruction.

Zeng et al [67] showed that Tuy's formula can be numerically implemented after substantial modification. However, the results for the modified Tuy algorithm are not too promising compared to other reconstruction methods.

Grangeat's method was the first exact inversion for non-truncated cone-beam data to be numerically implemented. The implementation of the algorithm involves three stages. In the first stage, the acquired cone-beam data are converted into $(\mathcal{R}f)'$, the first radial derivative of the 3D Radon transform using Grangeat's formula (5.1). In the second stage, the Radon data are rebinned into an uniform spherical grid and then numerically differentiated to obtain an approximation of the second derivative $(\mathcal{R}f)''$. Finally, the computationally efficient Marr's two-stage algorithm (see Section 4.4.1) is used to invert $(\mathcal{R}f)''$ to reconstruct the density f as stacks of discretized 2D densities.

Although Grangeat's method is numerically implementable, its second step of rebinning 3D data is a computationally intensive procedure, especially when a large number of source positions are sampled. Another shortcoming of this numerical approach is that parallel computing cannot be utilized to handle multiple source positions independently. Marr's two-stage algorithm (see Section 4.4.1) requires all of the discretized Radon data to be available. Thus, one must first process cone-beam data from all source positions before entering the two-stage algorithm based reconstruction phase.

On the other hand, the cone-beam FBP formula is implementable and computationally efficient in its discretized form [12, 44, 46]. Since the inversion formula (5.22) is given as an integral over the source parameter λ, cone-beam projection from each source can be processed and backprojected to the image domain, independent of other

source positions. This method is well-suited for parallel implementation. Due to its computational efficacy and adaptability to a generic source curve, we have chosen this method to make it a part of our ROI-reconstruction algorithm.

Chapter 6

Region-of-Interest Reconstruction from Truncated Cone-beam Projections

The problem of reconstruction of a density function from its non-truncated cone-beam projections is an ill-posed problem. We have seen in Chapter 3 that if Tuy's hypotheses on the density and the source curve are true, then the reconstruction problem is uniquely solvable. If the cone-beam data is partially unknown, that is, if the projections are *truncated*, there can be several difficulties, such as numerical instability or the lack of reconstruction algorithms. In this chapter, we present a novel method for region-of-interest reconstruction from ROI-truncated cone-beam projections acquired from any source curve satisfying Tuy's conditions. ROI-truncated projection is simply a restriction of the usual cone-beam projection, where the only rays effectively acquired must pass through a fixed spherical region of interest (ROI) located within

the support of the density.

6.1 ROI Truncated Cone-beam Transform

Let us assume that $f : \mathbb{R}^3 \to \mathbb{R}$ is smooth function with a compact support Ω. For simplicity, we assume that Ω is a closed ball of radius $\rho > 0$. Denote by $r(s, \beta)$ the ray or half-line originating from $s \in \mathbb{R}^3$ in the direction of $\beta \in \mathbb{S}^2$. For a spherical region of interest $C \subset \Omega$ and for a bounded curve $\Gamma \subset \mathbb{R}^3$ supported outside Ω, we define the set of *active rays* $\mathcal{J}_C$ as

$$\mathcal{J}_C = \{r(s, \beta) \in \Gamma \times \mathbb{S}^2 : r(s, \beta) \cap C \neq \emptyset\}. \tag{6.1}$$

Thus, $\mathcal{J}_C$ is the set of all rays originating from the curve Γ and intersecting the spherical region of interest C.

Definition 6.1.1. Let C be any spherical ROI in $\mathbb{R}^3$ such that $C \subset \Omega$. For $s \in \mathbb{R}^3$ and $\beta \in \mathbb{S}^2$, the *C-truncated cone-beam transform* of f is defined as

$$\mathcal{D}_C f(s, \beta) = \begin{cases} \mathcal{D}f(s, \beta), & \text{if } r(s, \beta) \in \mathcal{J}_C \\ 0, & \text{if } r(s, \beta) \notin \mathcal{J}_C. \end{cases} \tag{6.2}$$

For a source point $s \in \mathbb{R}^3$, the C-truncated cone-beam projection integrates f over only those rays or half-lines which originate from s and intersect the region of interest C. The C-truncated cone-beam transform $\mathcal{D}_C$ is just a restriction of the cone-beam transform $\mathcal{D}$.

Recall that the cone-beam transform $\mathcal{D}f$ is a function on $\mathbb{R}^3 \times \mathbb{S}^2$. More specifically,

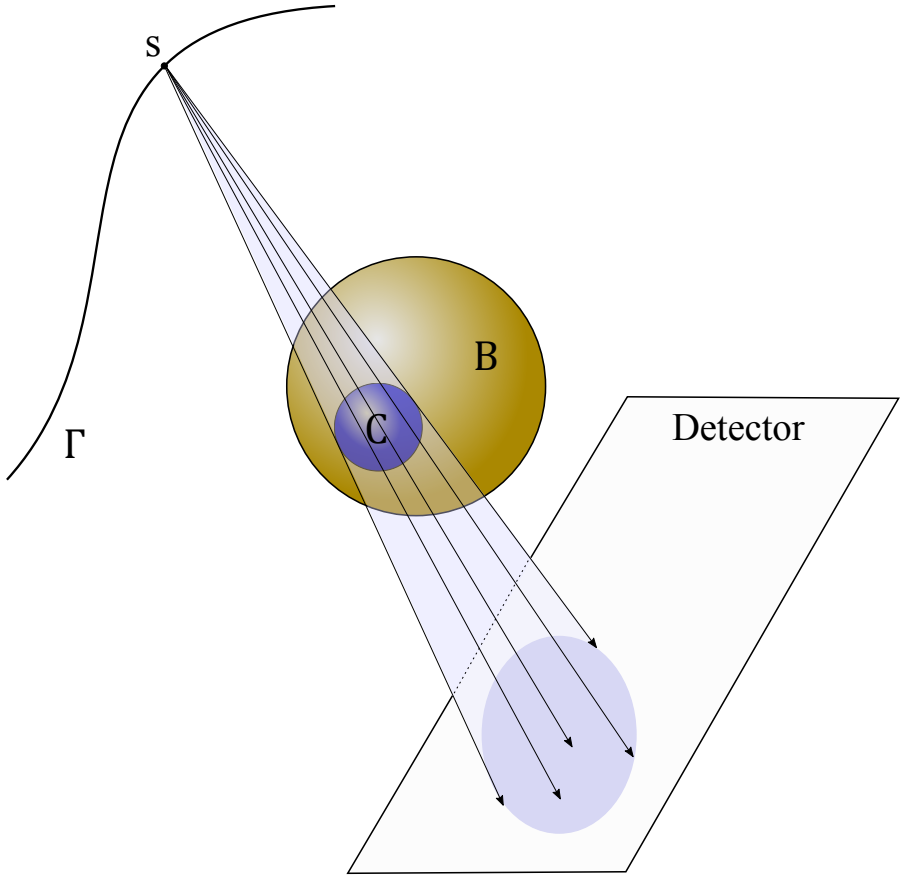

Figure 6.1: Truncated cone-beam transform, the cone-beam rays originating from $s \in \Gamma$ are only allowed to pass through the spherical region-of-interest C contained in the support B.

if the cone-beam data is acquired from sources located on a smooth curve Γ in $\mathbb{R}^3$, then $\mathcal{D}f$ is a function defined on a lower dimensional submanifold $\Gamma \times \mathbb{S}^2$. We have shown earlier that if the 3D density f is smooth and compactly supported and the curve Γ satisfies Tuy's conditions and $\mathcal{D}f(s, \beta)$ is known for all $(s, \beta) \in \Gamma \times \mathbb{S}^2$, then $f(x)$ can be theoretically reconstructed for any $x \in \Omega$ by an exact inversion formula such as Tuy's formula or Grangeat's inversion formula. The problem of ROI reconstruction from truncated projections has been studied in multiple papers, using a variety of

methods (see Chapter 2 for a comprehensive list). In general, the C-truncated cone-beam operator $\mathcal{D}_C$ does not have an exact inverse Z_C to give $Z_C\mathcal{D}_C f = 1_C f$, where $1_C f$ denotes the restriction of f to ROI C. Most ROI reconstruction formulas from truncated projections usually impose restrictions on the region of interest and depend on a specific cone-beam acquisition geometry. In addition, a priori knowledge of the density f within the ROI may be required for a stable and exact reconstruction.

We proceed to present an algorithm to invert the C-truncated cone-beam transform $\mathcal{D}_C f$ to recover $f(x)$ for all $x \in C$. Our algorithm is guaranteed to give an ϵ-accurate inverse of $\mathcal{D}_C$, given that the region of interest C is no smaller than a critical radius.

6.2 Approximate Inverses of the ROI Truncated Cone-beam Transforms

The problem of reconstruction of a density function f inside a fixed region of interest C strictly within the support of f from C-truncated cone-beam projections is called an *interior problem* (see [41, 43]). Natterer showed in [41] that the two-dimensional interior reconstruction problem from ROI restricted line integrals (2D Radon transform) is not uniquely solvable. Indeed, the same can be argued about the three-dimensional interior reconstruction problem from ROI restricted line integrals (i.e., ROI truncated cone-beam transform). Although the uniqueness is lost, one may still seek a method to construct an approximate recovery of f within the ROI C from truncated projections.

We present the notion of ϵ-accurate inverses of the ROI truncated cone-beam

transform. Assume that Ω is a compact subset of $\mathbb{R}^3$. For an integer $k \geq 0$, denote $W^k(\Omega)$ to be the Sobolev space of functions on Ω. Recall that

$$W^k(\Omega) = \left\{ f \in L^2(\Omega) : D^\alpha f \in L^2(\Omega), \quad \forall |\alpha| \leq k \right\}$$

where $\alpha = (\alpha_1, \alpha_2, \alpha_3) \in (\mathbb{Z}^+)^3$, $|\alpha| = |\alpha_1| + |\alpha_2| + |\alpha_3|$, and $D^\alpha f$ is any partial derivative of f of order $|\alpha|$. The space of functions $W^k(\Omega)$ forms a Banach space, endowed with the norm

$$||f||_{W^k(\Omega)} = \left(\int_\Omega \sum_{|\alpha| \leq k} |D^\alpha f(x)|^2 \, dx \right)^{1/2}.$$

The theoretical proof (presented in [3]) of the convergence of our iterative ROI reconstruction requires the density function f to be of class $W^5(\Omega)$.

Definition 6.2.1. Suppose Ω is a bounded open ball of $\mathbb{R}^3$ and let Γ be a smooth curve of $\mathbb{R}^3$ satisfying Tuy's conditions. Let C be a spherical ROI strictly included in Ω. For $\epsilon > 0$, we say that the C-truncated cone-beam transform $\mathcal{D}_C$ admits an *ϵ-accurate inverse* Z_C if Z_C is a bounded linear operator from $L^\infty(\mathcal{J}_C)$ to $L^\infty(\Omega)$ verifying

$$||f - Z_C \mathcal{D}_C f||_{L^\infty(\Omega)} \leq \epsilon ||f||_{W^5(\Omega)}, \tag{6.3}$$

for all $f \in W^5(\Omega)$.

Note that the ϵ-accurate inverse of the truncated cone-beam operator $\mathcal{D}_C$ is not unique. To see this, suppose for $\epsilon > 0$, Z_C is an ϵ-accurate inverse of $\mathcal{D}_C$. Since

$f \in W^5(\Omega)$, one has the estimate

$$||f||_{L^\infty(\Omega)} \leq c_1 ||f||_{W^5(\Omega)},$$

for some positive constant c_1. Since $\mathcal{D}_C$ is a bounded linear mapping from $L^\infty(\Omega)$ to $L^\infty(\mathcal{J}_C)$, there exists a positive constant c_2 such that

$$||\mathcal{D}_C f||_{L^\infty(\mathcal{J}_C)} \leq c_2 ||f||_{L^\infty(\Omega)}.$$

Define $T : L^\infty(\mathcal{J}_C) \to L^\infty(\Omega)$ to be a bounded linear mapping with operator norm $||T|| < \frac{\epsilon}{c_1 c_2}$. Thus, using the inequalities above, we have

$$||T\mathcal{D}_C f||_{L^\infty(\Omega)} \leq \epsilon ||f||_{W^5(\Omega)}.$$

Observing that

$$\begin{aligned} ||f - (Z_C + T)\mathcal{D}_C f||_{L^\infty(\Omega)} &\leq ||f - Z_C \mathcal{D}_C f||_{L^\infty(\Omega)} + ||T\mathcal{D}_C f||_{L^\infty(\Omega)} \\ &\leq 2\epsilon ||f||_{W^5(\Omega)}, \end{aligned}$$

we see that the operator $Z_C + T$ is a 2ϵ-accurate inverse of $\mathcal{D}_C$.

6.3 Regularization Operator

A major component of our ROI Reconstruction Algorithm is the regularization operator σ, which regularizes density functions f. Several variants of the regularization operator σ can be employed. In this section, we only present the average regulariza-

tion operator. Other regularization operators will be presented in Chapter 7.

6.3.1 Local Averaging

Suppose $f : \mathbb{R}^3 \to \mathbb{R}$ has a compact support Ω and C is a spherical region of interest strictly inside Ω. Let $\Omega \backslash C = \cup_j Q_j$, where $\{Q_j\}$ are mutually disjoint and $\text{vol}(Q_j) = v$. That is, $\{Q_j\}$ is a disjoint partition of the complement of ROI C, with each subset Q_j having the same fixed volume v. Define σ_A, the *average regularization operator* as

$$\sigma_A f(x) = \begin{cases} f(x), & \text{if } x \in C \\ \frac{1}{v} \int_{Q_j} f(x)\, dx, & \text{if } x \in Q_j. \end{cases} \tag{6.4}$$

The local averaging method is computationally efficient. If the density f is sampled on a discrete 3D grid of size N^3, then $\sigma_A f$ can be computed with $O(N^3)$ operations.

6.4 A New ROI Reconstruction Algorithm

In this section, we propose an iterative algorithm to reconstruct the density within a spherical region of interest. A similar ROI reconstruction algorithm for truncated cone-beam data appeared in the Ph.D. thesis [51] of our collaborator, Anando Sen. However, Sen's work was particularly tested on specific acquisition geometries, including sources on a sphere and a helix. In this thesis, we have extended Sen's algorithm to handle any smooth curve Γ satisfying Tuy's condition.

Let C be a spherical region in $\mathbb{R}^3$, contained inside the support Ω of f. We assume that the cone-beam scanning curve Γ is any curve in $\mathbb{R}^3$ which satisfies the Tuy's conditions, that is, any plane intersecting the support Ω must intersect the curve Γ at

least once and this intersection must be non-tangential. Let σ be a density regularization operator (for example, one may select $\sigma = \sigma_A$, or any other regularization method discussed in Chapter 7).

Our ROI reconstruction algorithm is initialized by setting $f_0 = \mathcal{D}^{-1}\mathcal{D}_C f$, where $\mathcal{D}^{-1}$ denotes an exact non-truncated inverse cone-beam operator. In Chapters 3 and 5, we presented a few non-truncated cone-beam inversion operators $\mathcal{D}^{-1}$. Successive approximations f_n of f are then iteratively obtained as follows

1. Compute the regularization σf_n of f_n (see Section 6.3).

2. Compute $\mathcal{D}\sigma f_n(s,\cdot)$ for all $s \in \Gamma$ and write

$$\mathcal{D}\sigma f_n = \mathcal{D}_C \sigma f_n + (\mathcal{D}\sigma f_n - \mathcal{D}_C \sigma f_n).$$

3. In the preceding formula, replace $\mathcal{D}_C\sigma f_n$ with the known truncated projection data $\mathcal{D}_C f$ and let

$$f_{n+1} = \mathcal{D}^{-1}\{\mathcal{D}_C f + (\mathcal{D}\sigma f_n - \mathcal{D}_C \sigma f_n)\}.$$

For smooth densities f with compact support, and for large enough spherical ROI C, we expect the sequence of approximate densities f_n generated by our algorithm to converge an ϵ-accurate inverse of the truncated cone-beam transform $\mathcal{D}_C$.

6.5 Convergence of our ROI Reconstruction Algorithm

In this thesis, we will verify through extensive numerical experiments (in Chapters 9 and 11) that for given any $\epsilon > 0$, a sequence of densities (f_j) generated by recursively by our ROI reconstruction algorithm converges at an exponential to an an ϵ-accurate approximate of a smooth density f compactly supported on Ω, given that the radius of the ROI $C \subset \Omega$ is no smaller than a critical radius $\rho(\epsilon)$.

A mathematical proof of the convergence of our ROI reconstruction algorithm appears in the paper [3] written by our research team. The main result proved in [3] is as follows. Assume $f \in W^5(\Omega)$. Let $\mathcal{D}^{-1}$ be an explicit operator inverting the non-truncated cone-beam projection $\mathcal{D}$ for smooth densities, (e.g., the Grangeat inversion operator). Fix any spherical ROI $C \subset \Omega$. Define the operators

$$U_N = \sigma \mathcal{D}^{-1} \tau_N (\mathcal{D} - \mathcal{D}_C), \tag{6.5}$$

where $\{\tau_N\}$ is an approximation of the identity in $L^2(\mathcal{J}_\Omega)$ (see Section 6.5.1 for details) and σ is a regularization operator on $L^2(\Omega)$. Given any $\epsilon > 0$, one can then find $N = N(\epsilon)$ and $\eta(\epsilon)$ such that the operator $U = U_{N(\epsilon)}$ becomes a contraction of $L^\infty(\Omega)$ provided $rad(\Omega) - rad(C) \leq \eta(\epsilon)$.

With $N = N(\epsilon)$ fixed as above and setting $f_0 = \mathcal{D}^{-1}\mathcal{D}_C f$, a sequence (f_j) is defined recursively by

$$f_{j+1} = f_0 + U f_j, \quad j = 1, 2, \ldots \tag{6.6}$$

The main criterion for convergence is the critical radius condition for an ROI

$C \subset \Omega$. It is proved (Theorem 1, [3]) that the sequence (f_j) converges to an ϵ-accurate reconstruction $\hat{f}$ of f, at exponential speed in $L^\infty(C)$, for any spherical ROI $C \subset \Omega$ having a radius satisfying $rad(\Omega) - rad(C) \leq \eta(\epsilon)$. That is, given an accuracy level ϵ and a sufficiently large spherical ROI $C \subset \Omega$, we generate an approximation $\hat{f}$ of f such that

$$||\hat{f} - f||_{L^\infty(C)} \leq \epsilon ||f||_{W^5(\Omega)}.$$

6.5.1 Regularization in the Space of Rays

We briefly explain here the construction of the sequence of linear operators $\{\tau_N\}$ on $\mathcal{J}_\Omega$, the space of Ω-active rays, used in (6.5). Further details of this sequence of linear operators can be found in [3].

Definition 6.5.1. Let $\mathcal{M}$ be a C^∞ Riemannian manifold with volume element $d\mu$ and finite volume. For any integer $r \geq 1$, we call any sequence $\tau_N : L^2(\mathcal{M}) \to C^r(\mathcal{M})$ a C^r *approximation of the identity in* $L^2(\mathcal{M}, \mu)$ if the following conditions hold true:

(i) There is a constant c such that for all $g \in L^2(\mathcal{M})$ and all integers N,

$$||\tau_N g||_{W^r(\mathcal{M})} \leq cN^r ||g||_{L^2(\mathcal{M})}.$$

(ii) For any $g \in L^2(\mathcal{M})$,

$$\lim_{N\to\infty} ||g - \tau_N g||_{L^2(\mathcal{M})} = 0, \quad \text{for each } g \in L^2(\mathcal{M}).$$

(iii) For each integer $2 \leq p \leq (r+1)$, there is a constant c such that for all $g \in$

$W^p(\mathcal{M})$

$$||g - \tau_N g||_{W^{p-1}(\mathcal{M})} \leq \frac{c}{N}||g||_{W^p(\mathcal{M})}.$$

(iv) If $g \in L^2(\mathcal{M})$ has a compact support, then so does $\tau_N g$.

A sequence approximating the identity in $L^2(\mathcal{J}_\Omega)$ can be easily constructed by patching together local small convolutions through appropriate local maps. Since $\mathcal{J}_\Omega$ is a smooth Riemannian manifold, one can select an open finite covering $\{U_j : j \in J\}$ and local maps $h_j : V_j \to U_j$, to construct a finite partition of unity by C^∞ functions u_j with compact supports included in U_j and verifying

$$0 \leq u_j \leq 1, \quad \text{and} \quad \sum_{j \in J} u_j = 1.$$

On each Euclidean ball $V_j \subset \mathbb{R}^k$, select a linear operator $\sigma_N(j)$ in $L^2(V_j)$ as follows. Fix any smooth function $w \geq 0$ in $L^2(V_j)$ such that w is compactly supported and $\int_{V_j} w = 1$. For $f \in L^2(\mathbb{R}^k)$, define the *small convolutions* by

$$\sigma_N(j)f = f * w_N,$$

where $w_N(x) = N^k w(Nx)$. For any $g \in L^2(\mathcal{J}_\Omega)$, let $g_j = gu_j$ and define

$$\tau_N g = \sum_{j \in J} G_j \circ h_j^{-1}, \tag{6.7}$$

where $G_j = \sigma_N(j)(g_j \circ h_j)$. For an appropriate index $\widetilde{N}$, $\tau = \tau_{\widetilde{N}}$ defines a regularization operator in $L^2(\mathcal{J}_\Omega)$.

Chapter 7

Regularization Operators

A major step in our ROI reconstruction of densities from ROI truncated cone-beam data involves regularization of densities outside the region of interest C. In Chapter 6, we have used a very simple regularization technique that locally averages a density over boxes of a fixed size. In this chapter we introduce two sophisticated wavelets based density regularization methods, called *hard thresholding* and *soft thresholding*. We begin with a brief review of wavelets.

7.1 A Short Review of Wavelets

Before explaining several wavelets based regularization techniques, we briefly review the theory of wavelets in one dimension, which can be naturally extended to higher dimensions. Recall that a *Multiresolution Analysis* (MRA) is defined to be a sequence of closed linear subspaces $(V_j)_{j\in\mathbb{Z}} \subset L^2(\mathbb{R})$ which satisfies the following properties:

1. $\{0\} \subset \cdots \subset V_{-1} \subset V_0 \subset V_1 \subset V_2 \subset \ldots$

2. $\cup_{j\in\mathbb{Z}} V_j$ is dense in $L^2(\mathbb{R})$.

3. $\cap_{j\in\mathbb{Z}} V_j = \{0\}$.

4. $f(x) \in V_j$ if and only if $f(2^{-j}x) \in V_0$.

5. There exists a scaling function $\phi \in L^2(\mathbb{R})$ such that $\{T_m\phi : m \in \mathbb{Z}\}$ is an orthonormal basis (ONB) for V_0, where $T_m\phi(t) = \phi(t-m)$.

The MRA decomposes functions into different *resolution* levels associated with the *wavelet spaces* $W_j, j \in \mathbb{Z}$, where each W_j is the orthogonal complement of V_j in V_{j+1}, i.e., $W_j = V_{j+1} \ominus V_j$. Thus, the space $L^2(\mathbb{R})$ is the direct sum of wavelet spaces W_j. A function in $\psi \in L^2(\mathbb{R})$ can always be chosen such that the collection

$$\{\psi_{j,k}(x) = 2^{j/2}\psi(2^j x - kx) : j,k \in \mathbb{Z}\}$$

forms an ONB for $L^2(\mathbb{R})$. We call such a function $\psi \in L^2(\mathbb{R})$ a *mother wavelet* function. Thus, for any $f \in L^2(R)$, we have the following *wavelet expansion* in $L^2(\mathbb{R})$

$$f = \sum_{j\in\mathbb{Z}}\sum_{k\in\mathbb{Z}} \langle f, \psi_{j,k}\rangle \psi_{j,k},$$
$$\langle f, \psi_{j,k}\rangle = \int_{-\infty}^{\infty} f(x)\psi_{j,k}(x)\,dx.$$

Since the wavelet ψ is chosen in such a way so that each $\psi_{j,k}$ has a support of size 2^{-j}, the wavelet expansion of f can be viewed as a decomposition of f into its components associated with various scales 2^{-j} and locations $2^{-j}k$.

An MRA for $L^2(\mathbb{R}^n)$ is generated by a multi-wavelet $(\psi_1, \ldots, \psi_L)$. For each $f \in L^2(\mathbb{R}^n)$, we have the wavelet expansion

$$f = \sum_{j\in\mathbb{Z}} \sum_{k\in\mathbb{Z}} \sum_{\ell=1}^{L} \langle f, \psi_{j,k}\rangle \psi_{j,k},$$

where $L = 2^n - 1$.

7.2 Wavelets-based Regularization

Regularization methods based on wavelets have shown to be very effective in applications of signal processing and image processing. Intuitively, the wavelets coefficients of large magnitudes correspond to the main features of the density f, whereas the coefficients of smaller magnitudes are associated with noisy features of the density. We present here two different wavelets based regularization methods.

For $f \in L^2(\mathbb{R}^3)$, we have the wavelet expansion

$$f = \sum_{j\in\mathbb{Z}} \sum_{k\in\mathbb{Z}} \sum_{\ell=1}^{L} \langle f, \psi^{\ell}_{j,k}\rangle \, \psi^{\ell}_{j,k}, \tag{7.1}$$

where $\psi^{\ell}_{j,k}$ is an orthonormal wavelet basis for $L^2(\mathbb{R}^3)$ and $L = 2^3 - 1 = 7$. We define a *hard thresholding regularization operator* σ_H as

$$\sigma_H f = \sum_{j\in\mathbb{Z}} \sum_{k\in\mathbb{Z}} \sum_{\ell=1}^{L} c_{j,k,\ell}(f) \, \psi^{\ell}_{j,k}, \tag{7.2}$$

where

$$c_{j,k,\ell}(f) = \begin{cases} \langle f, \psi^{\ell}_{j,k} \rangle & \text{if } j \leq j_0, \\ \langle f, \psi^{\ell}_{j,k} \rangle & \text{if } j > j_0 \text{ and } |\langle f, \psi^{\ell}_{j,k} \rangle| \geq Th_j, \\ 0 & \text{if } j > j_0 \text{ and } |\langle f, \psi^{\ell}_{j,k} \rangle| < Th_j. \end{cases} \tag{7.3}$$

The hard thresholding wavelet operator σ_H retains all coarse scale coefficients at scale $j \leq j_0$. We do not apply any shrinkage in the coarser scales as it is important to preserve some of the global features of the density. The *threshold* parameters Th_j are user selected, taking account of the noise at resolution level j.

One may also apply the wavelets based soft-thresholding method to regularize densities. For $f \in L^2(\mathbb{R}^3)$, a *soft thresholding regularization operator* σ_S is given by

$$\sigma_S f = \sum_{j \in \mathbb{Z}} \sum_{k \in \mathbb{Z}} \sum_{\ell=1}^{L} c_{j,k,\ell}(f)\, \psi^{\ell}_{j,k}, \tag{7.4}$$

where

$$c_{j,k,\ell}(f) = \begin{cases} \langle f, \psi^{\ell}_{j,k} \rangle & \text{if } j \leq j_0, \\ \langle f, \psi^{\ell}_{j,k} \rangle - Th_j & \text{if } j > j_0 \text{ and } |\langle f, \psi^{\ell}_{j,k} \rangle| \geq Th_j, \\ \langle f, \psi^{\ell}_{j,k} \rangle + Th_j & \text{if } j > j_0 \text{ and } |\langle f, \psi^{\ell}_{j,k} \rangle| \leq -Th_j, \\ 0 & \text{if } j > j_0 \text{ and } |\langle f, \psi^{\ell}_{j,k} \rangle| < Th_j. \end{cases} \tag{7.5}$$

Note that the operators σ_H and σ_S are non-linear. However, these non-linear operators can be well approximated by linearized versions which implement smooth shrinkage of the wavelet coefficients instead of abrupt truncation (see [51] for details).

7.2.1 Selection of Threshold Parameters

Whether the hard thresholding σ_H or soft thresholding σ_S is to be used, one must choose the threshold parameters Th_j carefully for effective regularization of densities. The choice of the threshold parameters Th_j depend on the type of problem one is interested in solving.

In [51], an iterative ROI reconstruction algorithm was tested exhaustively with regularization operators σ_H and σ_S to find the best threshold parameters Th_j. The ROI reconstruction algorithm in [51] is similar to our algorithm presented in Chapter 6, but is set in a restrictive setting with spherical acquisition. To generate the wavelet decomposition, Daubechies wavelets Daub4 was used. It was found that the best performance in the case of the hard thresholding operator σ_H is achieved when 9% of the highest magnitude wavelet coefficients are kept at the resolution level j. In the case of soft thresholding σ_S, the threshold parameters Th_j were chosen in such a way that approximately 90% of the coefficients were set to zero. The heuristic study in [51] concluded that the hard thresholding operator σ_H performed much better compared with the soft thresholding operator σ_S and the local-average operator σ_A introduced in Chapter 6.

Chapter 8

Numerical Implementation of the Truncated Cone-beam Inverse

In this chapter, we first give the details of the numerical implementation of the two exact non-truncated cone-beam transform inversion formulas presented in Chapter 5: Grangeat's method and the shift-variant filtered backprojection (FBP) algorithm. Although these methods are theoretically equivalent, their discretized versions appear to be different. One characteristic both of these methods have in common is that they can be used with projections acquired on arbitrary source curves satisfying Tuy's conditions. Next, we discuss the numerical implementation of our ROI reconstruction algorithm from truncated cone-beam projections, using as an essential building block the classical non-truncated inversion algorithms which are presented below.

8.1 Data Acquisition with a Planar Detector

Assume that the 3D density function $f(x_1, x_2, x_3)$ has its support in Ω, a closed ball in $\mathbb{R}^3$ centered at the origin. Denote by L the radius of the ball Ω. Thus, we have

$$\Omega = \{(x_1, x_2, x_3) \in \mathbb{R}^3 : x_1^2 + x_2^2 + x_3^2 \leq L^2\}. \tag{8.1}$$

We assume that f is a smooth function. Let Γ be the smooth cone-beam scanning curve satisfying Tuy's conditions, parametrized by $s(\lambda), \lambda \in \Lambda$, with

$$s(\lambda) = (s_1(\lambda), s_2(\lambda), s_3(\lambda)), \quad \lambda \in \Lambda, \tag{8.2}$$

where Λ is a finite union of intervals of the real line and s_1, s_2, s_3 are smooth functions defined on Λ.

We define the *virtual 2D detector* corresponding to the source position $s(\lambda)$ to be the tangent plane to Γ spanned by the unit vectors e_u^λ and e_v^λ, where

$$e_v^\lambda = e_w^\lambda \times e_u^\lambda, \quad e_w^\lambda = \frac{s(\lambda)}{||s(\lambda)||}, \quad e_u^\lambda = \frac{s'(\lambda)}{||s'(\lambda)||}, \tag{8.3}$$

for $\lambda \in \Lambda$. With our definition, the virtual detector is orthogonal to e_w^λ and at distance $D_\lambda \equiv ||s(\lambda)||$ from the source $s(\lambda)$. For $u, v \in \mathbb{R}$, each point $ue_u^\lambda + ve_v^\lambda$ on the virtual detector plane has local coordinates (u, v). We define the unit vector $\beta_\lambda(u, v)$ by

$$\beta_\lambda(u, v) = \frac{ue_u^\lambda + ve_v^\lambda - s(\lambda)}{\sqrt{u^2 + v^2 + D_\lambda^2}}. \tag{8.4}$$

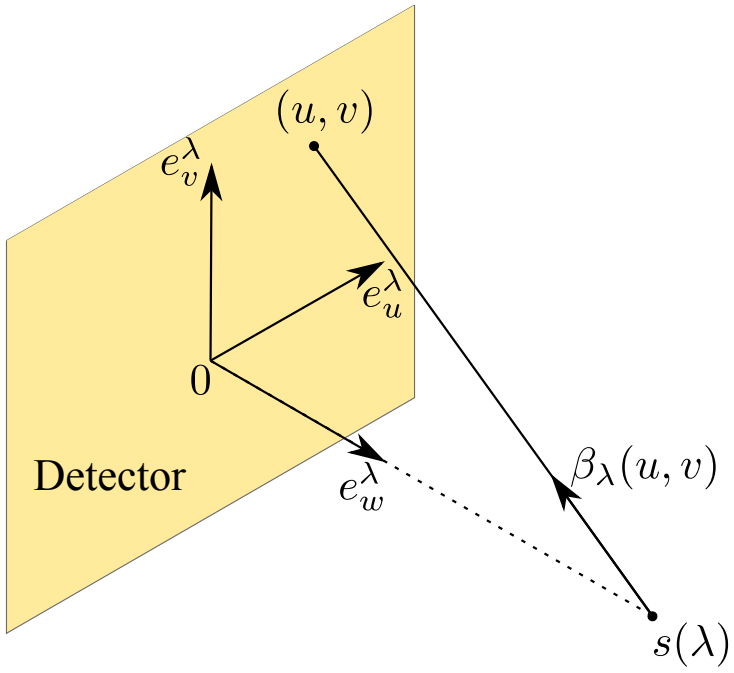

Figure 8.1: Cone-beam data acquisition with a planar detector. Each ray β_λ originating from source $s(\lambda)$ is associated with a pair of local coordinates (u, v) on the detector plane.

Thus, $\beta_\lambda(u, v)$ is the unit direction vector of the cone-beam ray which originates from the source $s(\lambda)$ and goes through the point (u, v) on the detector. Note that the origin on the detector and the origin of the global coordinate system coincide. Let us define the *cone-beam projection data* of the density f by a function g_d,

$$g_d(\lambda, u, v) = \int_0^\infty f(s(\lambda) + t\beta_\lambda(u, v))\, dt, \quad \lambda \in \Lambda, (u, v) \in \mathbb{R}^2. \tag{8.5}$$

Our earlier definition of the cone-beam transform and the function g_d are related by

$\mathcal{D}f(s(\lambda), \beta_\lambda(u,v)) = g_d(\lambda, u, v)$. In a practical medical imaging setting, a physical detector is always placed on one side of the object Ω at a fixed distance, and the source $s(\lambda)$ is placed on the other side of Ω. The impractical virtual detector that intersects the object Ω is introduced only for the sake of simpler numerical algorithms. Physically acquired cone-beam data can be immediately converted to virtual detector "acquisition data" by simple homothetic rescaling of the coordinates. Without any ambiguity, we can thus restrict our discussions to "data acquired" by the virtual detector, which we will simply call the *detector* from now on.

Since f has support in the closed ball Ω of radius $L > 0$, we note that the cone-beam rays from $s(\lambda)$ in the direction $\beta_\lambda(u,v)$ for all (u,v) such that $u^2 + v^2 > L^2$ do not penetrate Ω. Hence, we have $g_d(\lambda, u, v) = 0$ for all (u,v) such that $u^2 + v^2 > L^2$, and the support of $g_d(\lambda, u, v)$ is contained in the closed disk $u^2 + v^2 \leq L^2$.

8.2 Grangeat's Reconstruction from Non-truncated Cone-beam Data

In Chapter 5, we have presented Grangeat's analytical inversion formula for non-truncated cone-beam data. However, further modification to the theoretical Grangeat's formula is necessary in order to develop a stable algorithm which can be implemented numerically.

8.2.1 Connection between the 3D Radon Transform and the Cone-beam Transform

We proceed to express Grangeat's fundamental relation in terms of the detector coordinates. Although Grangeat's original work [20] presents the fundamental relation in detector geometry, his derivation of the inversion is not fully precise. We follow Defrise and Clack [13] to derive Grangeat's fundamental relation in detector geometry.

Let us denote $g(\lambda, \beta)$ to be the non-truncated cone-beam transform (3.1) of the density f from source position $s(\lambda), \lambda \in \Lambda$, in the direction $\beta \in \mathbb{S}^2$. That is, $g(\lambda, \beta) = \mathcal{D}_{s(\lambda)} f(\beta)$. Recall that Grangeat's fundamental relation makes a connection between the first radial derivative of the 3D Radon transform $\mathcal{R}f$ of f (4.1) and the non-truncated cone-beam transform g by

$$\frac{\partial}{\partial \rho} \mathcal{R}f(\omega, \rho)\bigg|_{\rho = \langle s(\lambda), \omega \rangle} = \int_{\beta \in \mathbb{S}^2 \cap \omega^\perp} \nabla_\omega g(\lambda, \beta) f(\beta)\, d\beta, \tag{8.6}$$

where the symbol ∇_ω stands for directional derivative in the direction $\omega \in \mathbb{S}^2$ acting on the second argument of g and $\mathbb{S}^2 \cap \omega^\perp$ is the great circle on $\mathbb{S}^2$ with axis of rotation ω. Note that (8.6) holds only when a cone-beam source $s(\lambda)$ lies on the plane $\Pi(\omega, \rho)$ orthogonal to $\omega \in \mathbb{S}^2$ at signed distance ρ from the origin. Assuming that Tuy's conditions on the curve Γ and the smoothness assumptions on the density f are fulfilled, Grangeat's relation (8.6) permits each source position $s(\lambda)$ to deliver the values of $\frac{\partial}{\partial \rho} \mathcal{R}f$ for all planes Π that contain the source $s(\lambda)$ and intersect the density support Ω.

On each detector plane, a line having signed distance τ from the origin and orthogonal to the two-dimensional unit vector $(\cos \vartheta, \sin \vartheta)$ (see Figure 8.2) satisfies the

equation

$$u\cos\vartheta + v\sin\vartheta = \tau. \tag{8.7}$$

Such lines on a detector plane can be represented by polar coordinates (ϑ, τ) with $\tau \in \mathbb{R}, \vartheta \in [0, \pi]$. For a fixed source $s(\lambda) \in \Gamma$ at distance D_λ from the origin, the intersection between a plane $\Pi(\omega, \rho)$ containing $s(\lambda)$ and the detector plane is the line (ϑ, τ) (see Figure 8.3), where (ω, ρ) and (ϑ, τ) are related by the formulas (proved in [13])

$$\omega(\vartheta, \tau) = \frac{D_\lambda \cos\vartheta e_u^\lambda + D_\lambda \sin\vartheta e_v^\lambda + \tau e_w^\lambda}{\sqrt{D_\lambda^2 + \tau^2}}, \tag{8.8}$$

$$\rho(\vartheta, \tau) = \frac{D_\lambda \tau}{\sqrt{D_\lambda^2 + \tau^2}}. \tag{8.9}$$

Thus, for a fixed source $s(\lambda)$ on the curve Γ, there is a one-to-one correspondence between the lines (ϑ, τ) on the detector and the planes containing $s(\lambda)$ and intersecting the density support Ω.

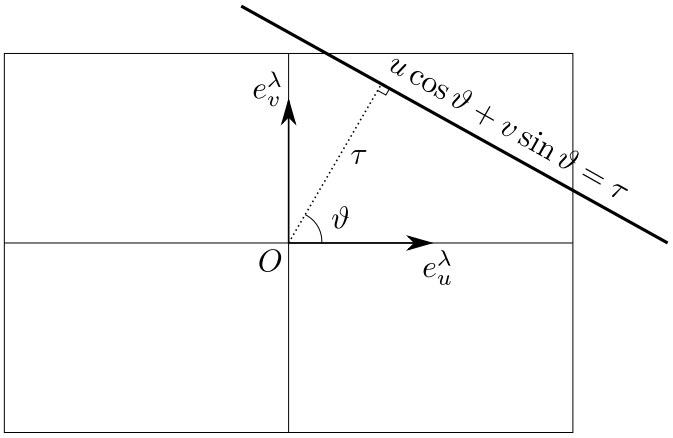

Figure 8.2: Parametrization of lines in the planar detector.

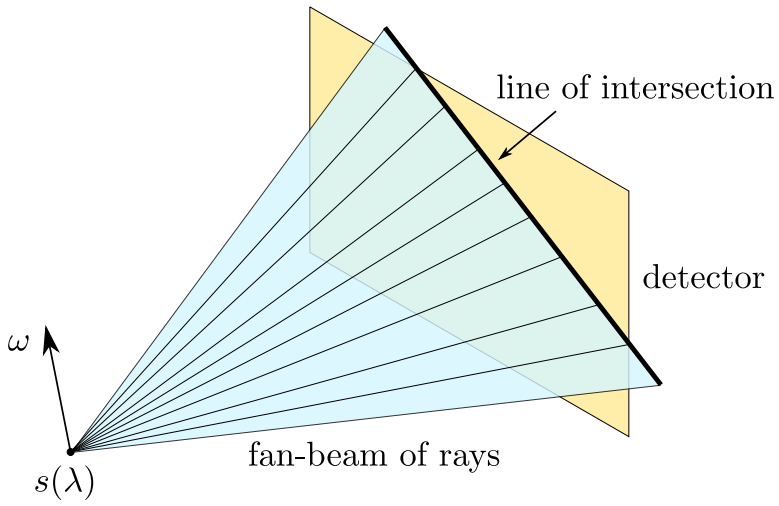

Figure 8.3: The fan-beam of rays on the plane $\Pi(\omega, \rho)$ orthogonal to $\omega \in \mathbb{S}^2$ and containing the source $s(\lambda)$ intersects the detector at an oriented line (ϑ, τ).

In the geometric setup defined by the object Ω, the curve Γ, and the planar virtual

detectors, the one-to-one correspondence between the planes $\Pi(\omega, \rho)$ containing $s(\lambda)$ and the lines (ϑ, τ) on the detector (given in (8.8)-(8.9)) allows one to re-formulate the integral on the right-hand side of Grangeat's fundamental relation (8.6) in terms of the detector's local coordinates. Let us define an intermediate function G by the expression

$$G(\lambda, \omega) = \int_{\beta \in \mathbb{S}^2 \cap \omega^\perp} \nabla_\omega g(\lambda, \beta)\, d\beta, \quad \lambda \in \Lambda, \omega \in \mathbb{S}^2. \tag{8.10}$$

Using the δ'-distribution (see Section 3.2), one may write

$$G(\lambda, \omega) = -\int_{\mathbb{S}^2} g(\lambda, \beta) \delta'(\langle \beta, \omega \rangle)\, dQ(\beta), \quad \lambda \in \Lambda, \omega \in \mathbb{S}^2. \tag{8.11}$$

Denote by $\widetilde{S} \subset \mathbb{S}^2$ to be the hemisphere on which $g(\lambda, \cdot)$ is defined. Define an auxiliary spherical coordinate system where each point $\beta \in \widetilde{S}$ is represented by the pair (ϕ_1, ϕ_2) such that $\phi_1 \in [-\pi/2, \pi/2]$ is the angle of elevation between ω and $-e_w^\lambda$ and $\phi_2 \in [0, \pi]$ is the angle between ω and the plane spanned by e_w^λ and e_u^λ. Using this angular coordinate system, we have

$$G(\lambda, \omega) = -\int_0^\pi \int_{-\frac{\pi}{2}}^{\frac{\pi}{2}} \sin\phi_1\, g(\lambda, \beta(\phi_1, \phi_2)) \delta'(\langle \beta(\phi_1, \phi_2), \omega \rangle)\, d\phi_1\, d\phi_2. \tag{8.12}$$

We define a similar function $G_d(\lambda, \vartheta, \tau) \equiv G(\lambda, \omega(\vartheta, \tau))$ using the coordinates of the lines. The spherical coordinates ϕ_1 and ϕ_2 of $\beta = \beta_\lambda(u, v)$ are related to the local detector coordinates (u, v) by

$$\cos\phi_1(u, v) = \langle \beta_\lambda(u, v), e_w^\lambda \rangle = -\frac{D_\lambda}{\sqrt{u^2 + v^2 + \mathcal{D}_\lambda^2}},$$

$$\phi_2(u, v) = \arctan(v/u).$$

The Jacobian of the transformation $(\phi_1, \phi_2) \to (u, v)$ is

$$\left|\begin{matrix} \frac{\partial\phi_1}{\partial u} & \frac{\partial\phi_1}{\partial v} \\ \frac{\partial\phi_2}{\partial u} & \frac{\partial\phi_2}{\partial v} \end{matrix}\right| = \left|\begin{matrix} -\frac{1}{\sqrt{u^2+v^2}}\frac{D_\lambda u}{(u^2+v^2+D_\lambda^2)} & -\frac{1}{\sqrt{u^2+v^2}}\frac{D_\lambda v}{(u^2+v^2+D_\lambda^2)} \\ -\frac{v}{u^2+v^2} & \frac{u}{u^2+v^2} \end{matrix}\right| = \frac{D_\lambda}{\sqrt{u^2+v^2}(u^2+v^2+D_\lambda^2)}.$$

Using the fact that $\sin\phi_1 = \frac{\sqrt{u^2+v^2}}{\sqrt{u^2+v^2+D_\lambda^2}}$, for $\tau = \tau_0$ we have

$$\begin{aligned} &G_d(\lambda, \vartheta, \tau_0) \\ &= -\int_0^{\pi}\int_{-\frac{\pi}{2}}^{\frac{\pi}{2}} \sin\phi_1\, g(\lambda, \beta(\phi_1,\phi_2))\delta'(\langle\beta(\phi_1,\phi_2), \omega(\vartheta,\tau_0)\rangle)\, d\phi_1\, d\phi_2 \\ &= -\int_{-\infty}^{\infty}\int_{-\infty}^{\infty} D_\lambda(u^2+v^2+D_\lambda^2)^{-3/2} g_d(\lambda,u,v)\delta'\left(\frac{D_\lambda(u\cos\vartheta + v\sin\vartheta - \tau_0)}{\sqrt{u^2+v^2+D_\lambda^2}\sqrt{\tau_0^2+D_\lambda^2}}\right) du\, dv \\ &= -\frac{\tau_0^2+D_\lambda^2}{D_\lambda}\int_{-\infty}^{\infty}\int_{-\infty}^{\infty} \frac{g_d(\lambda,u,v)}{\sqrt{u^2+v^2+D_\lambda^2}}\delta'(u\cos\vartheta + v\sin\vartheta - \tau_0)\, du\, dv, \end{aligned}$$

where we have used the scaling property of δ'. Introducing the variables τ and τ' related to u and v by

$$\tau = u\cos\vartheta + v\sin\vartheta, \quad \tau' = -u\sin\vartheta + v\cos\vartheta, \tag{8.13}$$

and using the main property of the δ'-distribution, we have

$$\begin{aligned} &G_d(\lambda, \vartheta, \tau_0) \\ &= -\frac{\tau_0^2+D_\lambda^2}{D_\lambda}\int_{-\infty}^{\infty}\int_{-\infty}^{\infty} \frac{g_d(\lambda, \tau\cos\vartheta - \tau'\sin\vartheta, \tau\sin\vartheta + \tau'\cos\vartheta)}{\sqrt{\tau^2+(\tau')^2+D_\lambda^2}}\delta'(\tau-\tau_0)\, d\tau\, d\tau' \\ &= \frac{\tau_0^2+D_\lambda^2}{D_\lambda}\int_{-\infty}^{\infty}\frac{\partial}{\partial\tau}\left(\frac{g_d(\lambda, \tau\cos\vartheta - \tau'\sin\vartheta, \tau\sin\vartheta + \tau'\cos\vartheta)}{\sqrt{\tau^2+(\tau')^2+D_\lambda^2}}\right)\Bigg|_{\tau=\tau_0} d\tau' \end{aligned}$$

$$= \frac{\tau_0^2 + D_\lambda^2}{D_\lambda} \frac{\partial}{\partial \tau} \left(\int_{-\infty}^{\infty} \frac{g_d(\lambda, \tau \cos\vartheta - \tau' \sin\vartheta, \tau \sin\vartheta + \tau' \cos\vartheta)}{\sqrt{\tau^2 + (\tau')^2 + D_\lambda^2}} \, d\tau' \right) \Bigg|_{\tau=\tau_0}.$$

Note that the absolute integrability of the integrand allows the change of the order of integration and differentiation. We define $\mathcal{L}$ to be the operator which integrates compactly supported two-dimensional densities over lines (ϑ, τ). That is, $\mathcal{L}$ is the *2D Radon transform* and for any compactly supported function h over $\mathbb{R}^2$, we have

$$\mathcal{L}h(\vartheta, \tau) = \int_{-\infty}^{\infty} h(\tau \cos\vartheta - \tau' \sin\vartheta, \tau \sin\vartheta + \tau' \cos\vartheta) \, d\tau', \tag{8.14}$$

for $\vartheta \in [0, \pi]$ and $\tau \in \mathbb{R}$. Realizing that the integral with respect to τ' is a 2D Radon transform value of the weighted density $g_d(\lambda, u, v)$, for each $\vartheta \in [0, \pi]$ and for each $\tau \in \mathbb{R}$, we have

$$G_d(\lambda, \vartheta, \tau) = \frac{\tau^2 + D_\lambda^2}{D_\lambda} \frac{\partial}{\partial \tau} \left(\mathcal{L} \left(\frac{g_d(\lambda, u, v)}{\sqrt{u^2 + v^2 + D_\lambda^2}} \right) (\vartheta, \tau) \right). \tag{8.15}$$

This intermediary functional $G_d(\lambda, \vartheta, \tau)$ of the cone-beam data $g_d(\lambda, u, v)$ is equal to the first radial derivative of the 3D Radon transform of the density f, i.e.

$$G_d(\lambda, \vartheta, \tau) = \frac{\partial}{\partial \rho} \mathcal{R}f(\omega(\vartheta, \tau), \rho(\vartheta, \tau)), \tag{8.16}$$

where $\omega(\vartheta, \tau)$ and $\rho(\vartheta, \tau)$ are defined as in (8.8) and (8.9).

8.2.2 Backprojection of the 3D Radon Data

Assume that the function $G_d(\lambda, \vartheta, \tau)$ of (8.15) is known for all $\lambda \in \Lambda$, $\vartheta \in [0, \pi]$, and $\tau \in [-L, L]$, where $L = rad(\Omega)$. Since G_d is the first radial derivative of the 3D Radon

transform, we may differentiate G_d with respect to ρ to obtain $\frac{\partial^2}{\partial \rho^2}\mathcal{R}f$ and use the 3D Radon inversion formula (4.15) to reconstruct f. One problem with the computation of the discretized derivative of $\frac{\partial}{\partial \rho}\mathcal{R}f$ is the irregular sampling of the Radon data on the points $(\lambda, \omega(\vartheta, \tau), \rho(\vartheta, \tau))$. Due to the same reason, one cannot implement the 3D Radon inversion using the computationally efficient two-stage algorithm (see Section 4.4.1) as it requires the Radon data to be on a spherical grid. This problem can be solved by first *rebinning* or *resampling* of the irregular Radon data to a spherical grid via 3D linear interpolation. An accurate and computationally efficient rebinning algorithm of Radon data is given in [45]. Once the Radon data have been rebinned to a spherical grid and $\frac{\partial}{\partial \rho}\mathcal{R}f(\theta, \phi, \rho)$ is known, $\frac{\partial}{\partial \rho}\mathcal{R}f$ can be numerically differentiated with respect to ρ and then be inverted using the two-stage algorithm given in Section 4.4.1 to reconstruct the density f from its Radon transform.

8.2.3 Summary of Grangeat's Inversion Algorithm from Non-truncated Cone-beam Data

We assume that the 3D density f of interest is *band-limited*, with bandwidth $E > 0$. That is, $f \in L^2(\mathbb{R}^3)$ and its Fourier transform $\widehat{f}(\xi) = 0$ for all $\xi \in \mathbb{R}^3$ such that $||\xi|| > E$. Suppose f is to be reconstructed on a discrete 3D equispaced rectangular grid of size N^3. It is difficult to determine an effective sampling of the sources on the curve and the parameters of the flat 2D detector. The analysis of proper sampling in cone-beam tomography, especially pertaining to exact reconstruction algorithms, has not been explored thoroughly in the literature. A heuristic study of Grangeat's inversion algorithm in [35], applied to the incomplete circular source curve, suggests the following sampling scheme. Let N_λ be the number of equally spaced source

parameters to be sampled from the interval Λ. Recall that for a fixed source $s(\lambda)$, each ray $\beta_\lambda(u,v)$ is associated with a sensor (u,v) on the detector. Let N_{ray} be the number of sensors (u,v) on each 2D array detector. For an accurate numerical implementation of Grangeat's formula, choose $N_{ray} = \lceil((2L)/\Delta x)^2\rceil$ and $N_\lambda = \lceil(\pi L)/\Delta x\rceil$, where $\Delta x = 1/(2E)$ is the sampling interval of the density f [35]. The sampling of Radon domain parameters θ, ϕ, ρ can be done along the lines of the two-stage 3D Radon algorithm discussed in Section 4.4.1. One may use these considerations as a guideline to implement Grangeat's inversion algorithm.

Grangeat's inversion algorithm to reconstruct f from non-truncated cone-beam data is summarized below.

Step 1: Compute Radon Data

For each sampled source position $\lambda_\ell, \ell = 1, \ldots, N_\lambda$:

1.1 Pre-weight the cone-beam projection data by the factor $1/\sqrt{u^2+v^2+D_{\lambda_\ell}^2}$ to obtain $h_d(\lambda_\ell, u, v) := \frac{g_d(\lambda_\ell,u,v)}{\sqrt{u^2+v^2+D_{\lambda_\ell}^2}}$, where D_{λ_ℓ} is the distance between $s(\lambda_\ell)$ and the origin.

1.2 Compute $\mathcal{L}h_d(\lambda_\ell, \vartheta, \tau)$, the 2D Radon transform (line integration of 2D image) of the weighted cone-beam data $h_d(\lambda_\ell, u, v)$. Efficient methods for discrete implementation of the 2D Radon transform $\mathcal{L}$ can be found in [25].

1.3 Differentiate numerically with respect to τ and obtain $\frac{\partial}{\partial\tau}\mathcal{L}h_d(\lambda_\ell, \vartheta, \tau)$. Higher order finite-difference scheme is recommended for the numerical evaluation of the derivative with respect to τ (our numerical experiments in Chapter 9 used 3-point finite-difference formulas of order 2).

1.4 Post-weight by the factor $(\tau^2 + D_{\lambda_\ell}^2)/D_{\lambda_\ell}^2$ to obtain

$$G_d(\lambda_\ell, \vartheta, \tau) = \frac{\tau^2 + D_{\lambda_\ell}^2}{D_{\lambda_\ell}} \frac{\partial}{\partial \tau} \mathcal{L} h_d(\lambda_\ell, \vartheta, \tau).$$

Proceed to Step 2 once $G_d(\lambda_\ell, \vartheta, \tau)$ is available for $\ell = 1, \ldots, N_\lambda$.

Step 2: Rebinning and Differentiation

2.1 Rebin $G_d(\lambda, \vartheta, \tau) = \frac{\partial}{\partial \rho} \mathcal{R} f(\omega(\vartheta, \tau), \rho(\vartheta, \tau))$ to a spherical grid (θ, ϕ, ρ) by trilinear interpolation, or by a numerically efficient method presented in [45].

2.2 Differentiate numerically with respect to ρ and obtain $\frac{\partial^2}{\partial \rho^2} \mathcal{R} f(\theta, \phi, \rho)$.

Step 3: Backprojection via Two-stage Algorithm

Apply the two-stage algorithm from Section 4.4.1 to invert $\frac{\partial^2}{\partial \rho^2} \mathcal{R} f(\theta, \phi, \rho)$ and reconstruct the density function f.

8.2.4 Computational Complexity

Following [1, 2, 23], we briefly discuss the computational complexity of Grangeat's inversion algorithm from non-truncated data. Assume that f is to be reconstructed as a voxel volume of size $N \times N \times N$, the cone-beam projections are 2D images of size $N \times N$, and total number of sources is N. Step 1 of the algorithm requires $O(N^4)$ operations, where 2D discrete Radon transform is the most costly operation, requiring $O(N)$ operations per line. The rebinning of Radon data to a spherical grid via trilinear interpolation in Step 2 requires $O(N^3)$ operations. The two-stage

algorithm requires $O(N^4)$ operations, as we have discussed earlier in Section 4.4.1. Thus, the computational complexity of Grangeat's inversion algorithm is $O(N^4)$.

8.3 Cone-beam FBP Algorithm

In Theorem 5.3.1, we have presented a non-truncated cone-beam inversion formula implementable by filtered backprojection (FBP) which can be numerically implemented for a generic smooth curves satisfying Tuy's conditions. Following Defrise and Clack [13], we discuss the implementation of this cone-beam FBP formula in terms of the detector coordinates.

8.3.1 Shift-Variant Filtering

We proceed to express filtered non-truncated cone-beam data $g^F(\lambda, \beta)$ (see (5.23) in Theorem 5.3.1) in terms of detector coordinates so that it can be practically implemented. Define the function

$$K(\lambda, \omega) = \frac{1}{4\pi^2} |\langle s'(\lambda), \omega \rangle| \, M(\omega, \lambda) \, G(\lambda, \omega), \tag{8.17}$$

so that we may write

$$g^F(\lambda, \beta) = -\int_{\widetilde{S}} K(\lambda, \omega) \, \delta'(\langle \beta, \omega \rangle) \, dQ(\omega). \tag{8.18}$$

Recall that the source weighting function M is a smooth function in both ω and

λ, satisfying the normalization condition

$$\sum_{k=1}^{n(\omega,\rho)} M(\omega, \lambda_k) = 1, \tag{8.19}$$

where $n(\omega, \rho)$ denotes the number of intersections between the plane $\Pi(\omega, \rho)$ and the curve Γ, and $\lambda_1, \ldots, \lambda_{n(\omega,\rho)} \in \Lambda$ are the solutions to $\rho = \langle s(\lambda), \omega \rangle$. If M is defined appropriately as above and the source curve Γ meets Tuy's conditions, then K is a smooth function with respect to λ and ω. Writing each point $\omega \in \widetilde{S}$ using spherical coordinates (ϕ_1, ϕ_2) as in Section 8.2, we obtain

$$g^F(\lambda, \beta) = -\int_0^{\pi} \int_{-\pi/2}^{\pi/2} \sin\phi_1 K(\lambda, \omega(\phi_1, \phi_2)) \delta'(\langle \beta, \omega(\phi_1, \phi_2) \rangle)\, d\phi_1\, d\phi_2. \tag{8.20}$$

Each line (ϑ, τ) on the detector corresponds the plane Π passing through $s(\lambda)$ and orthogonal to $\omega \in \mathbb{S}^2$, where

$$\omega(\vartheta, \tau) = \frac{D_\lambda \cos\vartheta e_u^\lambda + D_\lambda \sin\vartheta e_v^\lambda + \tau e_w^\lambda}{\sqrt{D_\lambda^2 + \tau^2}}. \tag{8.21}$$

The relations between the line (ϑ, τ) and the spherical coordinates (ϕ_1, ϕ_2) of $\omega(\vartheta, \tau)$ are given by

$$\cos(\phi_1(\vartheta, \tau)) = \frac{\tau}{\sqrt{D_\lambda^2 + \tau^2}}, \quad \phi_2(\vartheta, \tau) = \vartheta. \tag{8.22}$$

Realizing that the Jacobian of the mapping $(\phi_1, \phi_2) \to (\vartheta, \tau)$ is $D_\lambda/(\tau^2 + D_\lambda^2)$ and since $\sin(\phi_1(\vartheta, \tau)) = D_\lambda/\sqrt{\tau^2 + D_\lambda^2}$, we have

$$g^F(\lambda, \beta) = -\int_0^{\pi} \int_{-\infty}^{\infty} \frac{D_\lambda^2}{(\tau^2 + \mathcal{D}_\lambda^2)^{3/2}} K(\lambda, \omega(\vartheta, \tau)) \delta'(\langle \beta, \omega(\vartheta, \tau) \rangle)\, d\tau\, d\vartheta. \tag{8.23}$$

Let us define $K_d(\lambda,\vartheta,\tau) \equiv K(\lambda,\omega(\vartheta,\tau))$, and observe that

$$K_d(\lambda,\vartheta,\tau) = \frac{1}{4\pi^2}|\langle s'(\lambda),\omega(\vartheta,\tau)\rangle|\, M_d(\lambda,\vartheta,\tau)\, G_d(\lambda,\vartheta,\tau), \tag{8.24}$$

where we denote $M_d(\lambda,\vartheta,\tau) \equiv M(\omega(\vartheta,\tau),\lambda)$ and $G_d(\lambda,\vartheta,\tau)$ is the same intermediate function used above in equation (8.15). For $\beta = \beta_\lambda(u,v)$ as in (8.4), we have

$$\langle \beta_\lambda(u,v),\omega(\vartheta,\tau)\rangle = \frac{D_\lambda(u\cos\vartheta + v\sin\vartheta - \tau)}{\sqrt{u^2+v^2+D_\lambda^2}\sqrt{\tau^2+\mathcal{D}_\lambda^2}}. \tag{8.25}$$

Thus,

$$\begin{aligned}
&g^F(\lambda,\beta_\lambda(u,v)) = \\
&= -\int_0^\pi \int_{-\infty}^\infty \frac{D_\lambda^2}{(\tau^2+\mathcal{D}_\lambda^2)^{3/2}} K_d(\lambda,\vartheta,\tau)\delta'(\langle\beta_\lambda(u,v),\omega(\vartheta,\tau)\rangle)\, d\tau\, d\vartheta \\
&= -\int_0^\pi \int_{-\infty}^\infty \frac{D_\lambda^2}{(\tau^2+\mathcal{D}_\lambda^2)^{3/2}} K_d(\lambda,\vartheta,\tau)\delta'\left(\frac{D_\lambda(u\cos\vartheta + v\sin\vartheta - \tau)}{\sqrt{u^2+v^2+D_\lambda^2}\sqrt{\tau^2+\mathcal{D}_\lambda^2}}\right) d\tau\, d\vartheta \\
&= -(u^2+v^2+D_\lambda^2)\int_0^\pi \int_{-\infty}^\infty \frac{K_d(\lambda,\vartheta,\tau)}{\sqrt{\tau^2+\mathcal{D}_\lambda^2}}\delta'(u\cos\vartheta + v\sin\vartheta - \tau)\, d\tau\, d\vartheta \\
&= (u^2+v^2+D_\lambda^2)\int_0^\pi \frac{\partial}{\partial\tau}\left(\frac{K_d(\lambda,\vartheta,\tau)}{\sqrt{\tau^2+\mathcal{D}_\lambda^2}}\right)\Bigg|_{\tau=u\cos\vartheta+v\sin\vartheta} d\vartheta,
\end{aligned}$$

where we have used the scaling property of the δ' distribution. Finally, defining the function $g_d^F(\lambda,u,v) \equiv g^F(\lambda,\beta_\lambda(u,v))$, we obtain

$$g_d^F(\lambda,u,v) = (u^2+v^2+D_\lambda^2)\int_0^\pi \frac{\partial}{\partial\tau}\left(\frac{K_d(\lambda,\vartheta,\tau)}{\sqrt{\tau^2+\mathcal{D}_\lambda^2}}\right)\Bigg|_{\tau=u\cos\vartheta+v\sin\vartheta} d\vartheta. \tag{8.26}$$

The function $g_d^F(\lambda,u,v)$ is called the *shift-variant filtered cone-beam projection.* We

use the term "filtering" here formally just as an analogy with true FBP backprojections algorithms that use convolutions, such as the FDK algorithm [16] or Katsevich's spiral cone-beam FBP algorithm [27, 27]. The operations used to compute $g_d^F(\lambda, u, v)$ do not reduce to a convolution in the general case, when the weighting function $M_d(\lambda, \vartheta, \tau)$ is not a constant with respect to the source parameter λ [46]. However, if the function $M_d(\lambda, \vartheta, \tau)$ is a constant with respect to λ for a source curve Γ satisfying Tuy's conditions, then the filtering operations can be efficiently implemented via 2D convolutions of the cone-beam projection data [46] to obtain a *true* cone-beam filtered-backprojection inversion algorithm.

Let us summarize the steps needed to compute the filtered cone-beam data. Assume that $G_d(\lambda, \vartheta, \tau)$ has been computed using the steps we have shown earlier in Section 8.2. We also assume that the values of the weight function $M_d(\lambda, \vartheta, \tau)$ have been pre-computed or can be calculated without requiring intensive numerical effort.

1. Compute $K_d(\lambda, \vartheta, \tau) = \frac{1}{4\pi^2} |\langle s'(\lambda), \omega(\vartheta, \tau) \rangle| \, M_d(\lambda, \vartheta, \tau) \, G_d(\lambda, \vartheta, \tau)$.

2. Compute the weighted data $\widetilde{K}_d(\lambda, \vartheta, \tau) := \frac{K_d(\lambda, \vartheta, \tau)}{\sqrt{\tau^2 + D_\lambda^2}}$.

3. Differentiate numerically to compute $\widetilde{K}'_d(\lambda, \vartheta, \tau) := \frac{\partial}{\partial \tau} \widetilde{K}_d(\lambda, \vartheta, \tau)$.

4. Perform 2D backprojection (see [26]) on the uv-plane to efficiently compute the integral
$$J(\lambda, u, v) := \int_0^\pi \widetilde{K}'_d(\lambda, \vartheta, \tau)|_{\tau = u \cos\vartheta + v \sin\vartheta} \, d\vartheta.$$

5. Compute $g_d^F(\lambda, u, v) := (u^2 + v^2 + D_\lambda^2) J(\lambda, u, v)$.

One advantage of this filtering procedure is that each projection $g_d(\lambda_\ell, u, v)$ obtained from source $s(\lambda_\ell)$ can be processed by the steps outlined above independently of

the data acquisitions obtained from other source positions. Thus, the shift-variant filtering step can be digitally implemented using parallel computing schemes.

8.3.2 Voxel-driven Backprojection of Filtered Cone-beam Projections

One can reconstruct f by the filtered backprojection inversion formula

$$f(x) = \int_{\lambda\in\Lambda} \frac{1}{||x-s(\lambda)||^2}\, g^F\left(\lambda, \frac{x-s(\lambda)}{||x-s(\lambda)||}\right) d\lambda, \quad x\in\Omega, \tag{8.27}$$

where g^F is the properly filtered cone-beam data. Let us explain how the cone-beam FBP formula can be numerically implemented by a voxel-driven procedure, similar to the one commonly used in the FDK algorithm [16].

In numerical image reconstruction, the density function f is usually sampled on a 3D discrete grid contained in a cube $[-L,L]^3$. Note that the cube $[-L,L]^3$ actually contains Ω, the support of f. Define a rectangular 3D grid Ψ consisting of points $(x_1(i), x_2(j), x_3(k))$, where N is even and

$$x_1(i) = \left(\frac{2L}{N}\right) i, \quad i = -\frac{N}{2}, \ldots, \frac{N}{2}, \tag{8.28}$$

$$x_2(j) = \left(\frac{2L}{N}\right) j, \quad j = -\frac{N}{2}, \ldots, \frac{N}{2}, \tag{8.29}$$

$$x_3(k) = \left(\frac{2L}{N}\right) k, \quad k = -\frac{N}{2}, \ldots, \frac{N}{2}. \tag{8.30}$$

The sampled values $f(x_1(i), x_2(j), x_3(k))$ define a 3D discrete image of size $N\times N\times N$. We assume that the cone-beam projections are acquired from a discrete set of sources $\{s(\lambda_\ell)\}$ sampled from Tuy's curve Γ, with $\ell = 1, \ldots, N_\Lambda$ and $\lambda_\ell - \lambda_{\ell-1} = \Delta\lambda$.

The projection data acquired from each $s(\lambda_\ell)$ are gathered in the 2D discrete image $g_d(\lambda_\ell, u_i, v_j)$ of size $N_u \times N_v$ with

$$u_i = \left(\frac{2L}{N}\right) i, \quad i = -\frac{N_u}{2}, \ldots, \frac{N_u}{2}, \tag{8.31}$$

$$v_j = \left(\frac{2L}{N}\right) j, \quad j = -\frac{N_v}{2}, \ldots, \frac{N_v}{2}, \tag{8.32}$$

where we can assume that N_u and N_v are even.

We can rewrite the FBP formula in terms of the local detector coordinates (u, v) as

$$f(x) = \int_{\lambda \in \Lambda} \frac{1}{||x - s(\lambda)||^2}\, g_d^F(\lambda, u(\lambda, x), v(\lambda, x))\, d\lambda, \quad x \in \Omega, \tag{8.33}$$

where the detector coordinates $(u(\lambda, x), v(\lambda, x))$ correspond to the direction vector $\beta_\lambda(u(\lambda, x), v(\lambda, x)) = (x - s(\lambda))/||x - s(\lambda)||$. One can easily verify that

$$u(\lambda, x) = \frac{D_\lambda \langle x, e_u^\lambda \rangle}{D_\lambda - \langle x, e_w^\lambda \rangle}, \tag{8.34}$$

$$v(\lambda, x) = \frac{D_\lambda \langle x, e_v^\lambda \rangle}{D_\lambda - \langle x, e_w^\lambda \rangle}, \tag{8.35}$$

by solving for the intersection of the line passing through $s(\lambda)$ and $x \in \Omega$ and the planar detector. The voxel-driven backprojection procedure can be implemented as follows:

1. For each $\lambda_\ell, \ell = 1, \ldots, N_\Lambda$

   1.1 For each $x \in \Psi$ (reconstruction grid in (8.28))

      1.1.1 Compute $g_d(\lambda_\ell, u(\lambda_\ell, x), v(\lambda_\ell, x))$ by bilinear interpolation, where $u(\lambda_\ell, x)$, $v(\lambda_\ell, x))$ are as in (8.34).

1.1.2 Set $F^{\ell}(x) := g_d(\lambda_\ell, u(\lambda_\ell, x), v(\lambda_\ell, x))/||x - s(\lambda_\ell)||^2$

2. For each $x \in \Psi$ (reconstruction grid in (8.28))

2.1 Set $f_{rec}(x) := \Delta\lambda \sum_{\ell=1}^{N_\Lambda} F^{\ell}(x)$, where $f_{rec}(x)$ is the reconstructed value of $f(x)$.

8.3.3 Summary of the Exact Cone-beam FBP Algorithm

In the numerical implementation of the cone-beam FBP algorithm, the sampling of parameters is the same as for Grangeat's inversion algorithm. In fact, Step 1 of the cone-beam FBP algorithm is identical to Step 1 of Grangeat's method.

The exact cone-beam FBP algorithm to reconstruct f from cone-beam data is summarized below.

Step 1: Compute Radon Data

For each sampled source position $\lambda_\ell, \ell = 1, \ldots, N_\lambda$:

1.1 Pre-weight the cone-beam projection data by the factor $1/\sqrt{u^2 + v^2 + D_{\lambda_\ell}^2}$ to obtain $h_d(\lambda_\ell, u, v) := \frac{g_d(\lambda_\ell, u, v)}{\sqrt{u^2+v^2+D_{\lambda_\ell}^2}}$, where D_{λ_ℓ} is the distance between $s(\lambda_\ell)$ and the origin.

1.2 Compute $\mathcal{L}h_d(\lambda_\ell, \vartheta, \tau)$, the 2D Radon transform (line integration of 2D image) of the weighted cone-beam data $h_d(\lambda_\ell, u, v)$. Efficient methods for discrete implementation of the 2D Radon transform $\mathcal{L}$ can be found in [25].

1.3 Differentiate numerically with respect to τ and obtain $\frac{\partial}{\partial\tau}\mathcal{L}h_d(\lambda_\ell, \vartheta, \tau)$. Higher order finite-difference scheme is recommended for the numerical evaluation of

the derivative with respect to τ (our numerical experiments in Chapter 9 used 3-point finite-difference formulas of order 2).

1.4 Post-weight by the factor $(\tau^2 + D_{\lambda_\ell}^2)/D_{\lambda_\ell}^2$ to obtain

$$G_d(\lambda_\ell, \vartheta, \tau) = \frac{\tau^2 + D_{\lambda_\ell}^2}{D_{\lambda_\ell}} \frac{\partial}{\partial \tau} \mathcal{L} h_d(\lambda_\ell, \vartheta, \tau).$$

Step 2: Shift-variant Filtering

For each sampled source position $\lambda_\ell, \ell = 1, \ldots, N_\lambda$:

2.1 Compute $K_d(\lambda, \vartheta, \tau) = \frac{1}{4\pi^2} |\langle s'(\lambda), \omega(\vartheta, \tau) \rangle| \, M_d(\lambda, \vartheta, \tau) \, G_d(\lambda, \vartheta, \tau)$.

2.2 Compute the weighted data $\widetilde{K}_d(\lambda, \vartheta, \tau) := \frac{K_d(\lambda, \vartheta, \tau)}{\sqrt{\tau^2 + D_\lambda^2}}$.

2.3 Differentiate $\widetilde{K}_d$ with respect to τ and obtain $\widetilde{K}'_d(\lambda, \vartheta, \tau) := \frac{\partial}{\partial \tau} \widetilde{K}_d(\lambda, \vartheta, \tau)$.

2.4 Perform 2D backprojection (see [26]) on the uv-plane to efficiently compute the integral

$$J(\lambda, u, v) := \int_0^\pi \widetilde{K}'_d(\lambda, \vartheta, \tau)|_{\tau = u \cos\vartheta + v \sin\vartheta} \, d\vartheta.$$

2.5 Compute $g_d^F(\lambda, u, v) := (u^2 + v^2 + D_\lambda^2) J(\lambda, u, v)$.

Step 3: Cone-beam Backprojection

Backproject the filtered cone-beam data $g_d^F(\lambda, u, v)$ onto the 3D reconstruction grid (8.28), using the voxel-driven method discussed in 8.3.2, to reconstruct f.

8.3.4 Computational Complexity

Let us briefly discuss the complexity of the cone-beam FBP algorithm. Assume that we are interested in reconstructing f on a discrete 3D grid of size $N \times N \times N$, from cone-beam projections images of size $N \times N$, measured from N sources. According to [13], the filtering steps (Steps 1 and 2) in the algorithm require $O(N^4)$ operations, mainly due to the complexity of 2D line-integration and backprojection. A modified shift-variant filtering, where line-integration is performed via the linogram method [14,15], can reduce the filtering complexity down to $O(N^3 \log N)$. However, the voxel-driven 3D cone-beam backprojection requires $O(N^4)$ operations. Thus, the complexity of the exact cone-beam FBP algorithm is $O(N^4)$.

8.4 ROI Reconstruction Algorithm

We presented in Chapter 6 a novel algorithm to compute the ϵ-accurate inverse of the C-truncated cone-beam transform $\mathcal{D}_C$, where C is a spherical region of interest. There are three main tasks involved in each iteration of our ROI reconstruction algorithm:

1. Forward cone-beam projection
2. Inversion of cone-beam data by a non-truncated inverse $\mathcal{D}^{-1}$
3. Density regularization

It is very important to use an accurate yet fast forward cone-beam projection model in our iterative algorithm. The forward projection step can be accomplished by a number of ray-tracing methods, where each sampled ray is traced through individual voxel-volumes while accumulating the line integral value associated with the ray.

There exist a number of accurate and fast ray-tracing forward cone-beam projection methods, including Joseph's method [25] and Siddon's method [54].

We have presented two computationally efficient and theoretically exact non-truncated cone-beam inverse operator $\mathcal{D}^{-1}$ in Sections 8.2 and 8.3. Virtually any numerically implementable inverse $\mathcal{D}^{-1}$ can be incorporated with our reconstruction from ROI truncated cone-beam data outlined in Section 6.4. However, to retain numerical stability, we recommend the use of a non-truncated cone-beam inverse operator $\mathcal{D}^{-1}$ that is both theoretically exact and stable. Recall from Section 3.6 that for non truncated cone-beam data, there is an inverse operator $\mathcal{D}^{-1}$ which is both theoretically exact and stable if and only if the source curve Γ satisfies Tuy's conditions.

The density regularization method was discussed in explicit details in Section 6.3. Although any of the regularization methods we presented will assure convergence of our algorithm, through numerical experiments we found that the hard thresholding regularization method gives the best results.

8.4.1 Summary of our ROI Reconstruction Algorithm

Our ROI reconstruction algorithm from ROI C-truncated cone-beam data is initialized by setting $f_0 = \mathcal{D}^{-1}\mathcal{D}_C f$, where $\mathcal{D}^{-1}$ denotes an exact inverse of the non truncated cone-beam transform. In Chapters 3 and 5, we presented a few non-truncated cone-beam inverison operators $\mathcal{D}^{-1}$. Successive approximations f_n of f are then iteratively obtained as follows

1. Compute the regularization σf_n of f_n (see Section 6.3).

2. Compute $\mathcal{D}\sigma f_n(s,\cdot)$ for all $s \in \Gamma$ and write

$$\mathcal{D}\sigma f_n = \mathcal{D}_C\sigma f_n + (\mathcal{D}\sigma f_n - \mathcal{D}_C\sigma f_n).$$

3. In the preceding formula, replace $\mathcal{D}_C\sigma f_n$ with the known truncated projection data $\mathcal{D}_C f$ and let

$$f_{n+1} = \mathcal{D}^{-1}\{\mathcal{D}_C f + (\mathcal{D}\sigma f_n - \mathcal{D}_C\sigma f_n)\}.$$

For smooth densities f with compact support, and for large enough spherical ROI C, we expect the sequence of approximate densities f_n generated by our algorithm to converge an ϵ-accurate inverse of the truncated cone-beam transform $\mathcal{D}_C$.

8.4.2 Stopping Criterion

Let C be the spherical region of interest. As a stopping criterion for our ROI reconstruction algorithm, we adopted a standard rule to stop the iteration when f_j and f_{j+1} become close enough within C. For some small tolerance $b > 0$, we iterate the ROI reconstruction algorithm for all j satisfying

$$||f_{j+1} - f_j||_{L^1(C)} \leq b. \tag{8.36}$$

Chapter 9

Numerical Results for ROI Reconstruction with Twin-Circular Acquisition

In this chapter, we analyze the performance of our ROI reconstruction algorithm through extensive numerical experiments with simulated truncated cone-beam data acquired from the twin-circular acquisition geometry. The conditions imposed on the density function $f : \mathbb{R}^3 \to \mathbb{R}$ and the cone-beam source curve Γ are to be assumed as before. Assume that f has a compact support on the closed ball Ω of $\mathbb{R}^3$. We will denote by f_{rec} the reconstruction of f.

Let us first define a few classical metrics to analyze the fidelity of reconstructed images.

Definition 9.0.1. Let f be the real valued density function on $\mathbb{R}^3$ and f_{rec} be the reconstruction of f. For a spherical region of interest C inside Ω, the *ROI relative*

L^1-error (RLE) of the reconstruction of f within C is defined by

$$RLE = \frac{||f - f_{rec}||_{L^1(C)}}{||f||_{L^1(C)}}, \tag{9.1}$$

where $||f||_{L^1(C)} = \int_C |f(x)|dx$.

Definition 9.0.2. Let f be the real valued density function on $\mathbb{R}^3$ and f_{rec} be the reconstruction of f. For a spherical region of interest C inside Ω, the *peak signal-to-noise ratio (PSNR)* of the reconstruction of f within C is defined by

$$PSNR = 10 \cdot \log_{10} \left(\frac{\sup_{x \in C} |f(x)|}{\frac{1}{vol(C)}||f - f_{rec}||_{L^1(C)}} \right). \tag{9.2}$$

Definition 9.0.3. Let the set of N_λ points $\{s(\lambda_i) \in \mathbb{R}^3 : \lambda_1, \ldots, \lambda_{N_\lambda} \in \Lambda\}$ be a discretization of the cone-beam acquisition curve Γ. Assume that each discretized non-truncated cone-beam projection image is of size $N_u \times N_v$. For a spherical region of interest C inside Ω, denote by $P(\lambda_i, C)$ the number of sampled rays that intersect C. Define the *truncation level* $\tau(C)$ as

$$\tau(C) = 1 - \sum_{i=1}^{N_\lambda} \frac{P(\lambda_i, C)}{N_\lambda N_u N_v}. \tag{9.3}$$

9.1 Reconstruction Setup

For our numerical experiments, we have implemented the ROI reconstruction algorithm using the non-truncated cone-beam inverse operator $\mathcal{D}^{-1}$, which is based on the shift-variant cone-beam FBP formula presented in Chapter 8. The reconstruction was set on cone-beam acquisition geometry consisting of a source curve Γ formed by

two orthogonal circles of the same radius and a flat panel detector. The parameters of the reconstruction geometry are outlined below.

3D image size	=	256^3 voxels
Radius of each circle	=	1472 voxels
Number of sources per circle	=	360
Detector size	=	256 rows, 256 columns
Detector spacing	=	1 voxel
Source to detector distance	=	1472 voxels

The center of the 3D image and the center twin-circles coincide. It is assumed that each density is supported in a ball of radius 128 voxels. The radius 1472 voxels was selected after performing intensive numerical simulations; it gave the most accurate reconstruction for the inversion of non-truncated cone-beam data. As we have used a virtual detector centered at the origin, the source to detector distance is equal to the radii of the circles. To process the cone-beam projection data for the shift-variant cone-beam FBP algorithm following the methods outlined in Chapter 8, we have sampled $180 \times 256 = 46,080$ parametric lines per detector, where 180 is the number of direction angles ϑ and 256 is the number of sampled lines per direction ϑ. For the regularization step of the ROI reconstruction algorithm, we chose *hard-thresholding* regularization method, as we found this method to be more efficient when compared with other density regularization methods (see Chapter 7 for details). We used Daubechies wavelets Daub4 (see [38]) in $\mathbb{R}^3$ to generate the wavelet decomposition of the density function of interest, and discarded 90% of the wavelets coefficients of smaller magnitudes.

9.2 ROI Reconstruction of the Shepp-Logan Phantom

We have tested ROI reconstruction using our algorithm on the 3D Shepp-Logan head phantom [52, 53]. The head phantom is sampled on a 3D discrete grid of size $256 \times 256 \times 256$. The three middle planar slices of the Shepp-Logan phantom are shown in Figure 9.1.

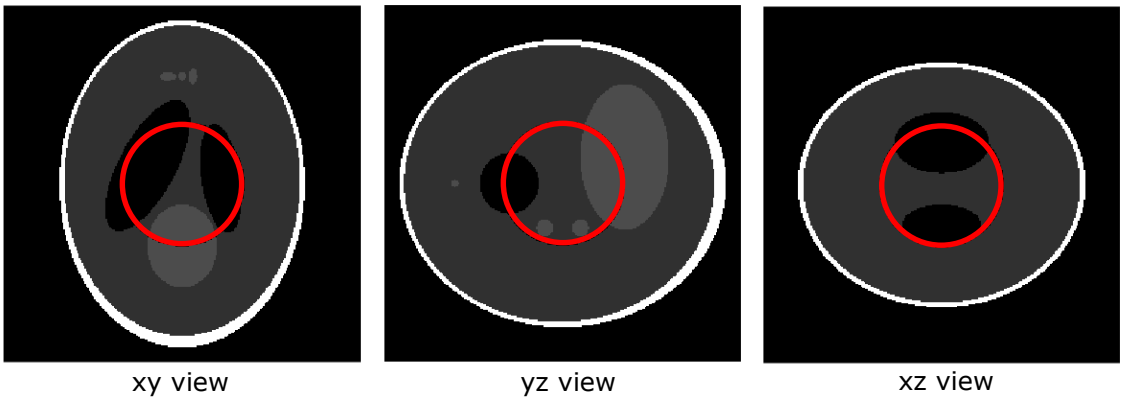

Figure 9.1: The mid-planar slices of the 3D Shepp-Logan Phantom and a spherical region of interest C (boundary shown in red).

We have selected various spherical regions of interest C of varying radii between 45 and 90 voxels, arbitrarily located strictly within the support of the density. One specific spherical ROI C located within the density image is shown in Figure 9.1.

As expected, direct application of the shift-variant cone-beam FBP to the ROI-truncated projections give unacceptable inaccuracies. As can be seen in Figure 9.2, severe artifacts such as heavy blurring and false edges are present in the naive ROI reconstruction method, whereas our algorithm gives far superior results. The comparison of the naive method and our ROI reconstruction method, along with the

true density are presented in Figure 9.2. Superior quality of our ROI reconstruction method is evident from the line intensity profiles of the mid-planar slices of the images reconstructed by the two methods and the ground truth, shown in Figure 9.3. Compared to the ground truth, although our ROI reconstructions are highly accurate, the reconstructed densities are slightly blurred. This is because the non-truncated cone-beam inverse operator $\mathcal{D}^{-1}$ (exact cone-beam FBP) used in our ROI reconstruction algorithm requires the density f of interest to be smooth. The 3D Shepp-Logan density has a number of discontinuities. Our ROI reconstructions appear to be smooth especially in the regions where the Shepp-Logan phantom has discontinuities.

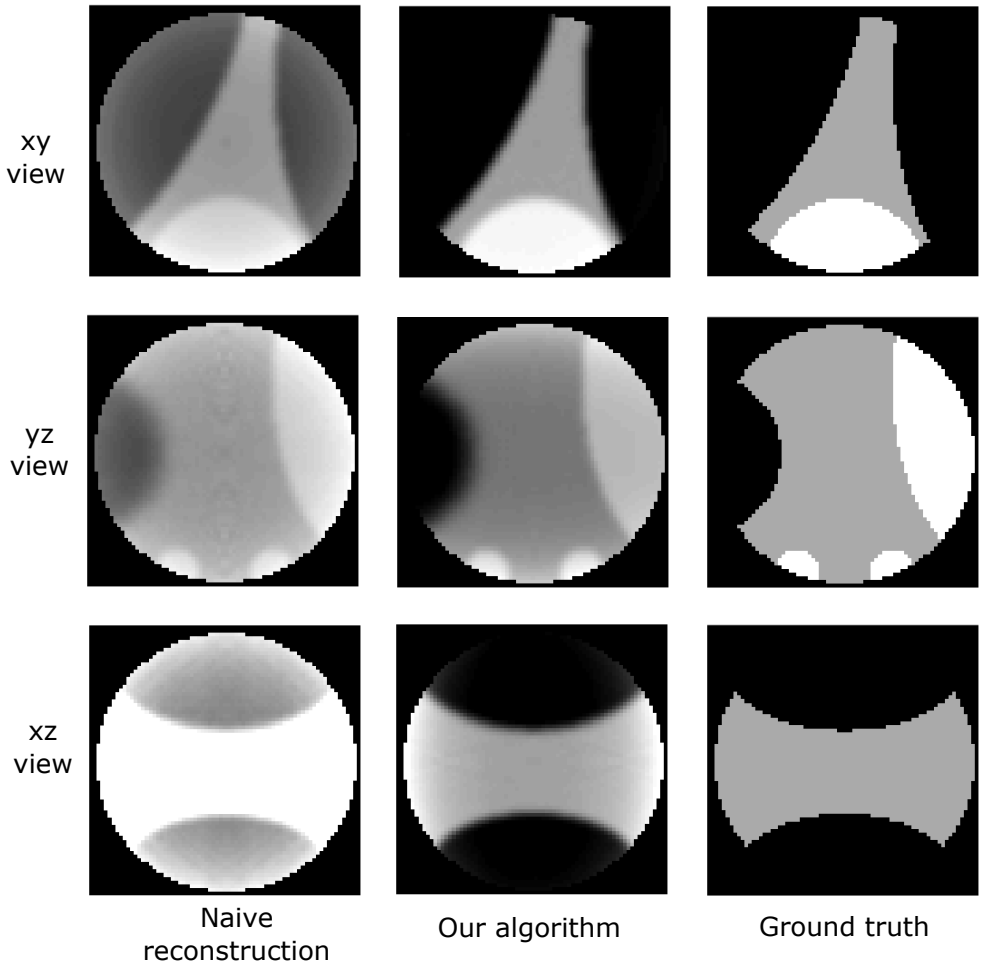

Figure 9.2: Visual comparison of ROI reconstruction for 3D Shepp-Logan phantom using Twin-circular acquisition and ROI-truncated projections. ROI radius = 45 voxels. Middle slices are shown from the xy, yz, and xz planes. From left to right: direct application of shift-variant cone-beam FBP; our iterative ROI reconstruction; ground truth.

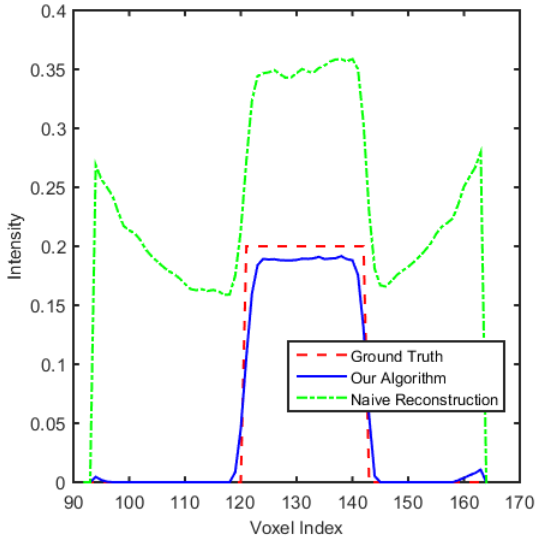

(a) xy slice

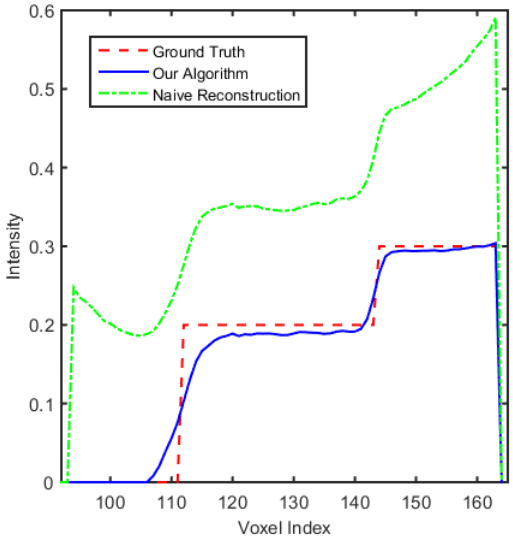

(b) yz slice

Figure 9.3: Visual comparison of ROI reconstruction for 3D Shepp-Logan phantom using Twin-circular acquisition and ROI-truncated projections. ROI radius = 45 voxels. Intensity profiles for a fixed row corresponding to the mid-planar slices are shown.

We will assess the performance of our ROI-reconstruction method and compare

it to the performance of the naive method quantitatively using the two metrics RLE and $PSNR$ introduced in the beginning of this chapter. When a region of interest C of radius 75 voxels is chosen, a direct application of the cone-beam FBP method to the truncated projection data yields $RLE = 46.2\%$ and $PSNR = 10.95$ dB, whereas our iterative ROI reconstruction method performs clearly better with $RLE = 8.9\%$ and $PSNR = 22.3$ dB after only 9 iterations. Additional ROI reconstruction results for the Shepp-Logan phantom are given for different ROI radii in Table 9.1.

It is obvious that smaller size ROIs yield larger degree of cone-beam truncations τ. From the perspective of medical imaging, large truncation τ in the X-ray projections means the body to be imaged undergoes less radiation exposure than usual. Our ROI reconstruction method achieves reconstruction error $RLE = 14.8\%$ with ROI truncation level $\tau = 89.6\%$. This is a significant gain the world of medical imaging. The relationship between the degree of truncation τ and the relative reconstruction error RLE is evident from Figure 9.4.

Table 9.1: Performance of our ROI reconstruction of Shepp-Logan Phantom for various spherical ROI radii.

ROI radius	**Truncation level**	**RLE**	**PSNR**
45 voxels	89.6%	14.8%	19.7 dB
60 voxels	81.8%	14.7%	19.8 dB
75 voxels	71.9%	8.9%	22.3 dB
90 voxels	59.9%	4.8%	25.6 dB

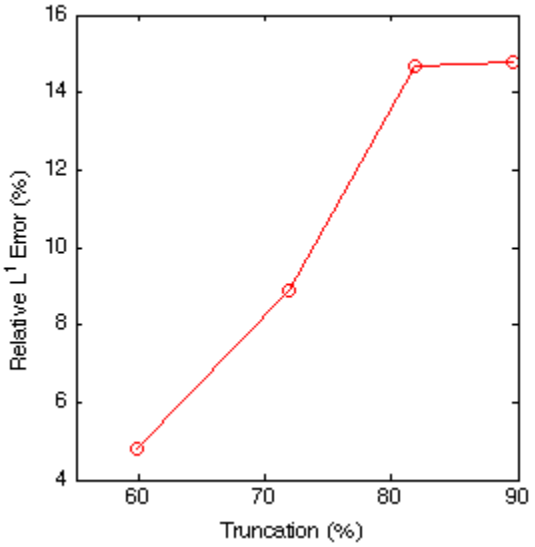

Figure 9.4: Relation between the degree of truncation level τ and the relative reconstruction error RLE for ROI reconstruction of the Shepp-Logan phantom.

9.3 ROI Reconstruction of Biological Data

A reconstruction method benchmarked by simulated phantoms such as the Shepp-Logan head phantom does not necessarily prove the robustness of the method in handling real data problems. In this section, our ROI reconstruction algorithm is validated by region of interest reconstruction of biological data. It is a challenging task to obtain real C-truncated cone-beam projection data, especially with arbitrary source curves. In order to obtain as close to real biological projection data, we start from 3D densities reconstructed previously by classical methods from real non-truncated cone-beam X-ray projection data. The 3D densities are tested to make sure that they are free of severe artifacts. We then simulate ROI-truncated cone-beam projections with discretized sources lying on the twin-circular trajectory from

these 3D densities.

Our first 3D density data was a previously reconstructed density from a full non-truncated X-ray CT scan of a mouse. The planar slices of the mouse data are shown in Figure 9.5. The original image was of size $512 \times 768 \times 512$. We extracted a sub-cube Ω of size 256^3 located near the brain of the mouse. For ROI-reconstruction tests, we selected small spherical regions of interest C of varying radii between 45 and 90 voxels arbitrarily placed strictly within Ω. A visual comparison of the direct application of cone-beam FBP method to truncated data and our ROI reconstruction algorithm is shown in Figure 9.6. Line intensity profiles of the ROI reconstructions by both methods and the ground truth are presented in Figure 9.7. A summary of quantitative performance for various ROIs is given in Table 9.2.

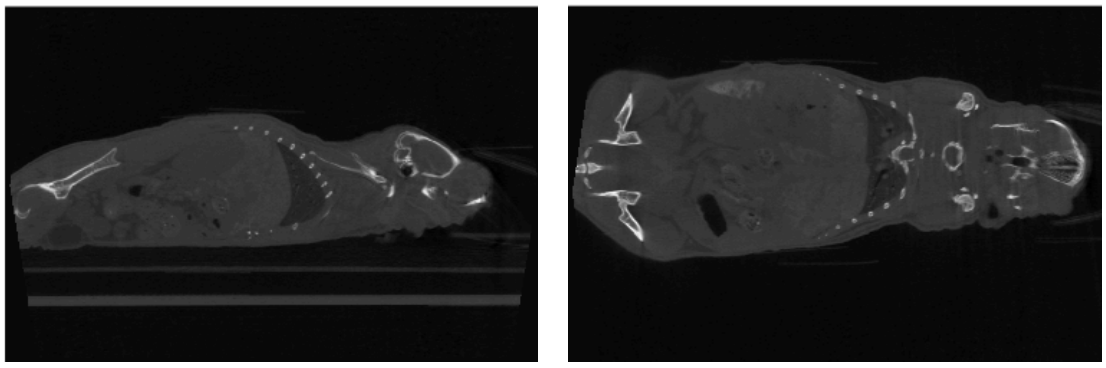

Figure 9.5: Planar slices of full body scan of a mouse.

It is interesting to note that with substantial truncation level $\tau = 81.8\%$, our ROI reconstruction achieves $RLE = 9.4\%$ and $PSNR = 29.3$ dB. This demonstrates how useful our method can be in radiology to produce high quality ROI reconstructions with smaller dosage of radiation.

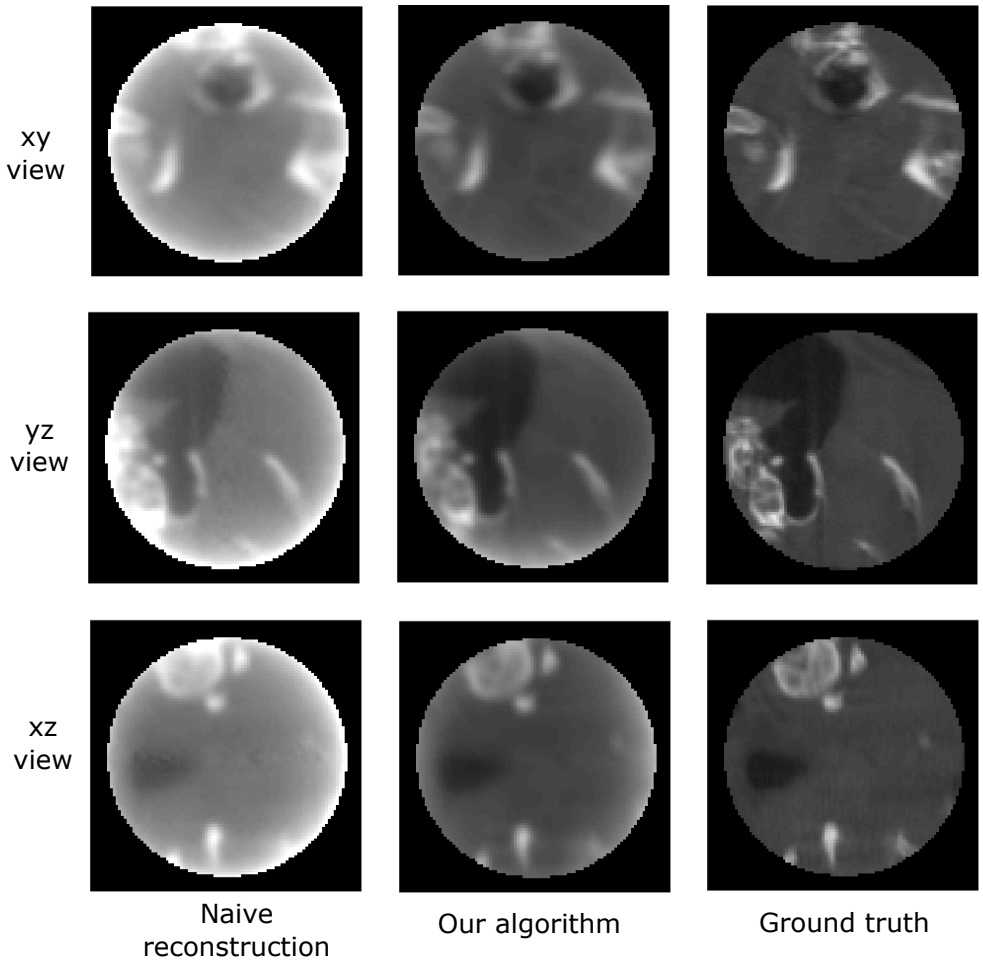

Figure 9.6: Visual comparison of ROI reconstruction for Mouse Tissue using Twin-circular acquisition and ROI-truncated projections. ROI radius = 45 voxels. Middle slices are shown from the xy, yz, and xz planes. From left to right: direct application of shift-variant cone-beam FBP; our iterative ROI reconstruction; ground truth.

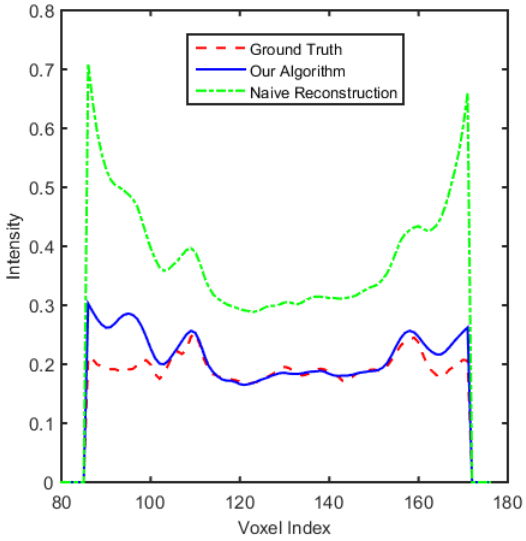

(a) xy slice

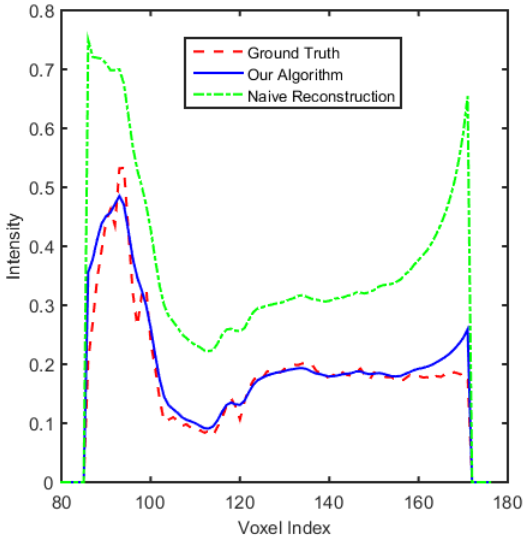

(b) yz slice

Figure 9.7: Visual comparison of ROI reconstruction for Mouse Tissue using Tuncircular acquisition and ROI-truncated projections. ROI radius = 45 voxels. Intensity profiles for a fixed row corresponding to the mid-planar slices are shown.

Our second biological image data set was a previously reconstructed density from

Table 9.2: Performance of the ROI reconstruction of Mouse Tissue for various spherical ROI radii.

ROI radius	**Truncation level**	**RLE**	**PSNR**
45 voxels	89.6%	12.5%	26.8 dB
60 voxels	81.8%	9.4%	29.3 dB
75 voxels	71.9%	8.3%	30.1 dB
90 voxels	59.9%	7.8%	31.4 dB

non-truncated CT scans of a human jaw. The whole 3D data set is of size $536 \times 536 \times 440$. The planar slices of the image are shown in Figure 9.8.

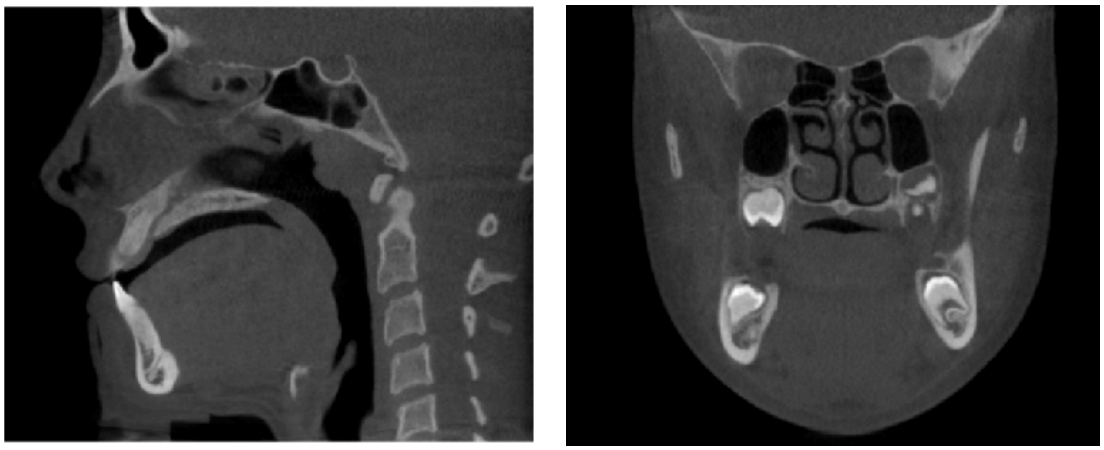

Figure 9.8: Planar slices of full scan of a human jaw.

As we have done for the mouse data, we extracted a discretized sub-cube Ω of size 256^3 from the full data set to test ROI reconstruction. The spherical ROIs C of various radii between 45 and 90 voxels were strictly included within Ω. Visual comparison of ROI reconstructions by naive cone-beam FBP formula and our iterative reconstruction method are shown in Figure 9.9. The quantitative performance of our method is given in Table 9.3.

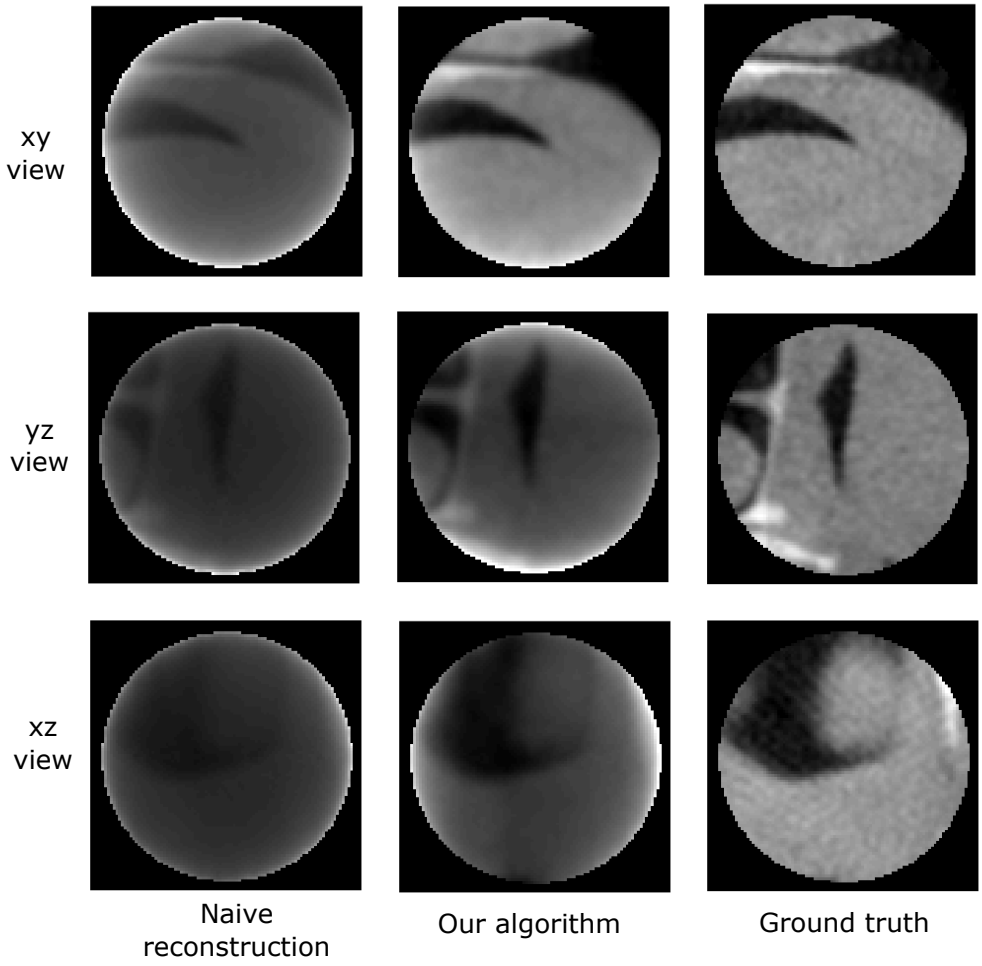

Figure 9.9: Visual comparison of ROI reconstruction for Human Jaw using Twin-circular acquisition and ROI-truncated projections. ROI radius = 45 voxels. Middle slices are shown from the xy, yz, and xz planes. From left to right: direct application of shift-variant cone-beam FBP; our iterative ROI reconstruction; ground truth.

Table 9.3: Performance of the ROI reconstruction of Human Jaw for various spherical ROI radii.

ROI radius	**Truncation level**	**RLE**	**PSNR**
45 voxels	89.6%	15.0%	21.2 dB
60 voxels	81.8%	13.3%	26.5 dB
75 voxels	71.9%	10.2%	29.0 dB
90 voxels	59.9%	9.8%	29.4 dB

9.4 Numerical Analysis of the Convergence our ROI Reconstruction Algorithm

In this section, we present the critical radius condition for ϵ-accurate ROI reconstruction from C-truncated cone-beam projections and the rate of convergence of our algorithm.

9.4.1 Critical Radius

We have stated in Chapter 6 that for $\epsilon > 0$, there exists a *critical radius* $\rho(\epsilon)$ such that our ROI reconstruction algorithm converges to an ϵ-accurate inverse within a ROI C strictly within Ω, given that the radius of C is no smaller than the critical radius $\rho(\epsilon)$. The statement was proved using rigorous mathematics by our research team (see [3] for details).

Based on our extensive numerical experiments of ROI reconstruction of the three images on several regions of interest C of various radii, we estimated the critical radius $\rho(\epsilon)$ of ROI reconstruction for each image. We fixed an accuracy level $\epsilon = 10\%$. The critical radius ρ of ROI reconstruction of the Shepp-Logan is 73 voxels. The critical radius ρ for the Mouse Tissue and the Human Jaw are 49 and 82 voxels, respectively.

The relative reconstruction error REL vs. ROI radius plots of the three images is shown in Figure 9.10.

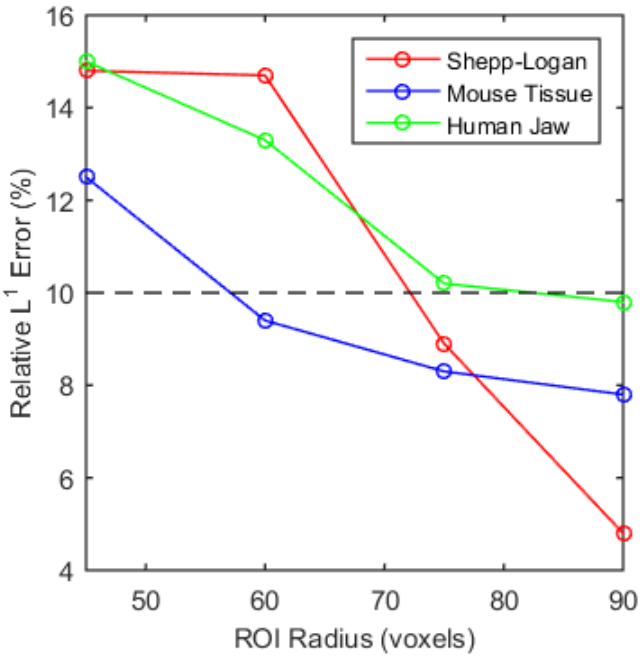

Figure 9.10: Relative L^1 Error (RLE) vs ROI radius for ROI reconstruction of three images: Shepp-Logan (red), Mouse Tissue (blue), and Human Jaw (green). The black dashed line represents a fixed ROI reconstruction accuracy level $\epsilon = 10\%$. The radius value corresponding to the intersection between the dashed line and an error curve of an image gives the critical radius $\rho(\epsilon)$ of ROI reconstruction of that image.

9.4.2 Rate of Convergence

It is proved theoretically in [3] that our ROI reconstruction algorithm converges to an ϵ-accurate at an exponential speed, given that the radius of the region of interest C is no smaller than a critical radius $\rho(\epsilon)$. It is evident from the plots presented in Figure 9.11 and Figure 9.12 that the relative reconstruction error decays exponentially after 4 to 5 iterations. This means that the decay of the relative L^1 error RLE with respect

to iteration k can be modeled by

$$RLE(k) = ae^{-bk},$$

where $a > 0$ is a constant and $b > 0$ is the *rate of decay*. Based on our numerical experiments of ROI reconstructions of the three discretized densities on various ROIs, we estimated the exponential rate of convergence for each case by linear regression. As the first 4 to 5 iterations involve dealing with severely noisy data, we used relative errors obtained between for $k \geq 6$ to estimate of the rate of decay for each case. We found that the exponential rate of convergence to be between 0.22 and 0.34. The estimated convergence rates of our algorithm for individual cases are presented in Table 9.4.

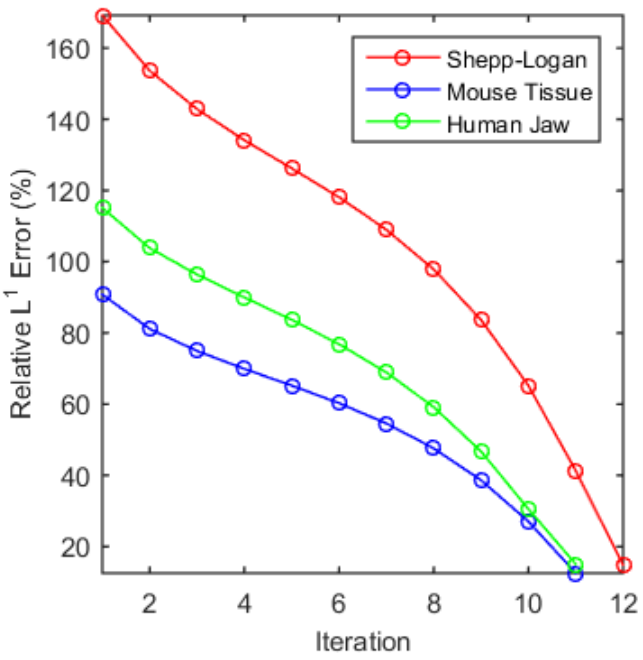

Figure 9.11: Relative L^1 Error (RLE) vs iteration of our algorithm for ROI reconstruction of three images: Shepp-Logan (red), Mouse Tissue (blue), and Human Jaw (green). Spherical ROI radius = 45 voxels.

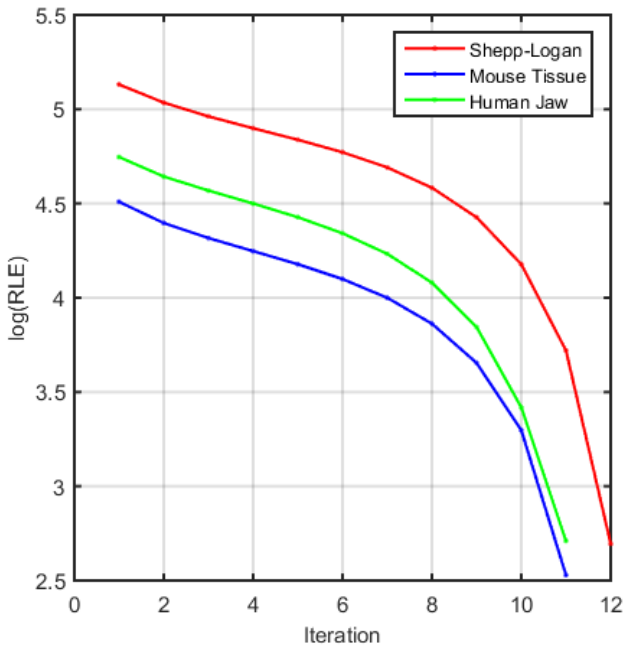

Figure 9.12: Relationship between logarithm of the Relative L^1 Error (RLE) and iterations of our algorithm for ROI reconstruction of three images: Shepp-Logan (red), Mouse Tissue (blue), and Human Jaw (green). Spherical ROI radius = 45 voxels. After 4-5 iterations, the logarithm of the error curves tend to be linear.

Table 9.4: Exponential rate of convergence of our ROI reconstruction algorithm. The table shows rates of convergence for ROI reconstructions of three images (Shepp-Logan, Mouse Tissue, and Human Jaw) on several spherical regions of interest C of radii between 45 and 90 voxels.

ROI radius	**Shepp-Logan**	**Mouse Tissue**	**Human Jaw**
45 voxels	0.25	0.22	0.23
60 voxels	0.28	0.24	0.26
75 voxels	0.30	0.24	0.27
90 voxels	0.34	0.23	0.24

Chapter 10

Non-truncated Cone-beam Inversion with Acquisition from a Generic Source Curve

In this chapter, we present a non-standard source curve (spherical spiral) for non-truncated cone-beam reconstruction which satisfies Tuy's condition. In CT literature, there exist a number of exact non-truncated cone-beam inversion algorithms. For example, Katsevich [27,28] proved a theoretically exact Spiral CT non-truncated cone-beam inversion formula, which can be numerically implemented using shift-invariant filtering. However, the Katsevich algorithm requires the source curve Γ to be a circular helix. To our knowledge, Grangeat's method, or its variant cone-beam FBP inversion (see Chapter 5), are the only exact and stable algorithms for non-truncated cone-beam acquisition with any source curve Γ satisfying Tuy's conditions. In this chapter, we focus our discussion to spherical spiral curves satisfying Tuy's conditions.

10.1 Spherical Spiral Source Curve

A *circular spiral* source curve Γ is parametrically expressed by

$$s(\lambda) = \left(R\cos\lambda, R\sin\lambda, \frac{Rh\lambda}{2\pi} \right), \quad -2\pi T \leq \lambda \leq 2\pi T, \tag{10.1}$$

where $R > 0$ is the radius, $T > 0$ is the number of turns, and $h > 0$ is the pitch of the spiral, i.e., the vertical height between two turns (see Figure 10.1). Note that Γ lies on the surface of a finite cylinder Z with radius $R > 0$ and height $2hT$. The circular spiral Γ will satisfy Tuy's conditions (see Chapter 3) if the support of the density f is a relatively small compact set Ω contained inside of Z. Thus, to implement an exact and stable non-truncated cone-beam inversion of densities supported in Ω, one must find appropriate parameters R, T, and h of the circular spiral Γ so that Tuy's conditions are fulfilled.

Assume that the virtual planar detector is defined as in Chapter 8. For a fixed source $s(\lambda)$, the *cone angle* of the beam of x-rays originating from $s(\lambda)$ and passing through the object Ω depends on the distance between the detector and the source position $s(\lambda)$. The sizes of the finite planar detectors depend on the cone angles, as the detectors should be large enough to contain the non-truncated cone-beam projections. One disadvantage of the the circular spiral Γ is that as the source moves along the spiral, the distance D_λ between the source $s(\lambda)$ and the origin (that is, the distance between $s(\lambda)$ and the virtual detector) is not constant. Thus, the cone angle or the size of the detector will always change, depending on $s(\lambda)$. Using detectors of different sizes may lead to degraded numerical reconstructions from non-truncated cone-beam projections. In fact, for generic source curve reconstruction algorithms

such as Grangeat's method, or its variant cone-beam FBP algorithm, choosing different sized detectors mean irregularly sampling non-truncated cone-beam data, which can generate unpredictable inaccuracies in the reconstructions.

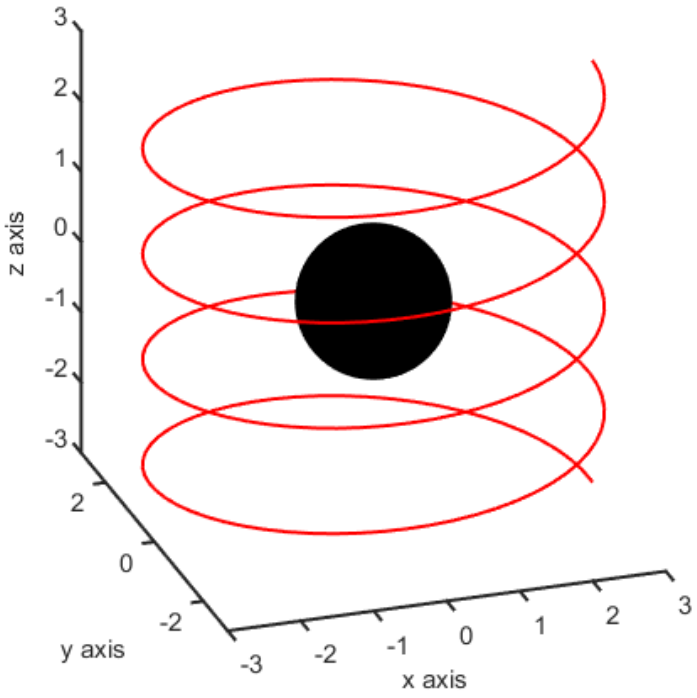

Figure 10.1: A circular spiral trajectory Γ, typically used in cone-beam CT. The spiral Γ clearly satisfies Tuy's condition as the spiral radius $R = 3$, pitch $h = 0.5$, vertical height $v = 3$ and the object radius $L = 1$.

The circular spiral may be modified so that the source $s(\lambda)$ is always at a fixed distance from the origin. We define the *spherical spiral* curve Γ to be

$$s(\lambda) = \left(\frac{2\pi R \cos\lambda}{\sqrt{4\pi^2 + (h\lambda)^2}}, \frac{2\pi R \sin\lambda}{\sqrt{4\pi^2 + (h\lambda)^2}}, \frac{Rh\lambda}{\sqrt{4\pi^2 + (h\lambda)^2}} \right), \quad -2\pi T \leq \lambda \leq 2\pi T, \tag{10.2}$$

with T turns which lie on the sphere of radius $R > 0$ (see Figure 10.2). Note that the parameter $h > 0$ does not necessarily represent a fixed pitch of the spiral. The vertical height v of the spherical spiral Γ is

$$v = ||s(2\pi T) - s(-2\pi T)|| = \frac{2hRT}{\sqrt{1 + (hT)^2}}. \tag{10.3}$$

The curve Γ defined in (10.2) will satisfy Tuy's condition 1 if and only if the radius R and the vertical height v are sufficiently large compared to the radius of the closed ball containing the density support Ω.

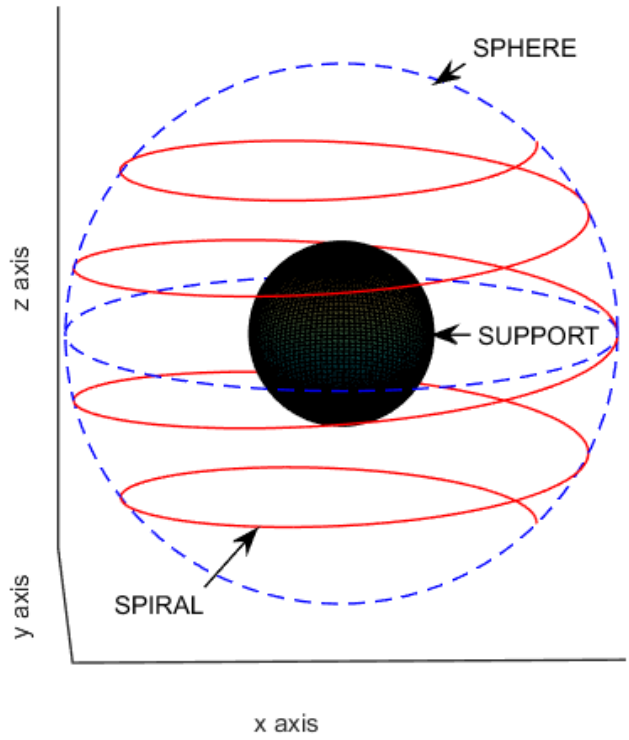

Figure 10.2: A non-standard spherical spiral trajectory Γ. The spiral Γ clearly satisfies Tuy's condition as the spiral radius $R = 3$, parameter $h = 0.5$, vertical height $v \approx 4.2$ and the object radius $L = 1$.

10.2 Non-truncated Cone-beam FBP Inversion

We now present in detail the implementation of the non-truncated cone-beam FBP inversion formula with spherical spiral acquisition. Most of the implementation details have already been presented in Section 8.3. However, we need to choose a specific weighting function particularly associated with the spherical spiral curve Γ.

10.2.1 Geometry and Data Acquisition

Assume that the 3D density function $f(x_1, x_2, x_3)$ is smooth and has its support in Ω, a closed ball in $\mathbb{R}^3$ centered at the origin. Denote by L the radius of the ball Ω. Thus, we have

$$\Omega = \{(x_1, x_2, x_3) \in \mathbb{R}^3 : x_1^2 + x_2^2 + x_3^2 \leq L^2\}. \tag{10.4}$$

Let Γ be the spherical spiral cone-beam scanning curve defined as in (10.2). One must choose the parameters R, T, and h of the curve Γ appropriately to fulfill Tuy's conditions. The following inequalities

$$R > \sqrt{2}L, \quad L < \frac{2hRT}{\sqrt{1 + (hT)^2}}, \tag{10.5}$$

must hold simultaneously in order to guarantee Tuy's completeness condition of the spherical spiral curve Γ.

As in Chapter 8, we define the planar virtual detector corresponding to the source position $s(\lambda)$ to be the tangent plane to Γ spanned by the unit vectors e_u^λ and e_v^λ, where

$$e_v^\lambda = e_w^\lambda \times e_u^\lambda, \quad e_w^\lambda = \frac{s(\lambda)}{||s(\lambda)||}, \quad e_u^\lambda = \frac{s'(\lambda)}{||s'(\lambda)||}, \tag{10.6}$$

for $-2\pi T \leq \lambda \leq 2\pi T$. With our definition, the virtual detector is orthogonal to e_w^λ and at distance $D_\lambda \equiv ||s(\lambda)||$ from the source $s(\lambda)$. For $u, v \in \mathbb{R}$, each point $ue_u^\lambda + ve_v^\lambda$ on the virtual detector plane has local coordinates (u, v). The unit vector $\beta_\lambda(u, v)$ defined by

$$\beta_\lambda(u, v) = \frac{ue_u^\lambda + ve_v^\lambda - s(\lambda)}{\sqrt{u^2 + v^2 + D_\lambda^2}}. \tag{10.7}$$

is parallel to the cone-beam ray which originates from the source $s(\lambda)$ and goes through the point (u, v) on the detector. The cone-beam projection data of the density f is

$$g_d(\lambda, u, v) = \int_0^\infty f(s(\lambda) + t\beta_\lambda(u, v))\, dt, \quad \lambda \in \Lambda, (u, v) \in \mathbb{R}^2. \tag{10.8}$$

10.2.2 Weighting Function

Recall the source weighting function M required by the non-truncated cone-beam FBP formula from Chapter 5. In a typical situation a plane $\Pi(\omega, \rho)$, orthogonal to $\omega \in \mathbb{S}^2$ at distance ρ from the origin, may contain more than just one source in Γ. In such cases, non-truncated cone-beam data acquired from a number of sources can be used to compute the same 3D Radon data. To handle this redundancy, a smooth function $M(\omega, \lambda)$ can be introduced, satisfying the normalization condition

$$\sum_{k=1}^{n(\omega,\rho)} M(\omega, \lambda_k) = 1, \tag{10.9}$$

where $n(\omega, \rho)$ denotes the number of intersections between the plane $\Pi(\omega, \rho)$ and the curve Γ, and $\lambda_1, \ldots, \lambda_{n(\omega,\rho)} \in \Lambda$ are the solutions to $\rho = \langle s(\lambda), \omega \rangle$. An obvious choice

for the function $M(\omega, \lambda)$ which satisfies the normalization condition is

$$M(\omega, \lambda) = \frac{1}{n(\omega, \langle s(\lambda), \omega \rangle)}, \tag{10.10}$$

where $n(\omega, \langle s(\lambda), \omega \rangle)$ denotes the number of intersections between the source curve Γ and the plane Π passing through $s(\lambda)$ and orthogonal to ω. However, this trivial choice of M has many discontinuities. An appropriate weighting function M is given by [13]

$$M(\omega, \lambda) = \frac{|\langle s'(\lambda), \omega \rangle|^m c(\lambda)}{\sum_{k=1}^{n(\omega, \langle s(\lambda), \omega \rangle)} |\langle s'(\lambda_k), \omega \rangle|^m c(\lambda_k)}, \tag{10.11}$$

where m is a positive integer and $c : \Lambda \to \mathbb{R}$ is a smooth function equal to one everywhere, except near the boundaries of the interval Λ. This choice of M is C^1 in both ω and λ when $m > 2$ (see [13]).

In order to compute the values of a weighting function $M(\omega, \lambda)$ (similar to the one given in (10.11)) for the spherical spiral curve Γ, for each source position $\lambda \in \Lambda$, first we need to compute $n(\omega, \rho)$, the number of intersections between the plane $\Pi(\omega, \rho)$ and the curve Γ, for all $\omega \in \mathbb{S}^2$ and all $\rho \in \mathbb{R}$. There is at least one intersection between the plane $\Pi(\omega, \rho)$ and the spherical spiral curve Γ if and only if there exists a $\lambda \in \Lambda$ satisfying $\langle \omega, s(\lambda) \rangle = \rho$. In other words, writing $\omega = (\omega_1, \omega_2, \omega_3)$, the number of $\lambda \in \Lambda$ satisfying

$$\omega_1 \frac{2\pi R \cos \lambda}{\sqrt{4\pi^2 + (h\lambda)^2}} + \omega_2 \frac{2\pi R \sin \lambda}{\sqrt{4\pi^2 + (h\lambda)^2}} + \omega_3 \frac{Rh\lambda}{\sqrt{4\pi^2 + (h\lambda)^2}} = \rho, \tag{10.12}$$

will give us the exact number of intersections between $\Pi(\omega, \rho)$ and Γ. However, it is not feasible to solve (10.12) analytically. Thus, we solve this nonlinear equation

numerically. Let us define the function F by

$$F(\omega, \rho, R, h, \lambda) = 2\pi R(\omega_1 \cos\lambda + \omega_2 \sin\lambda) + R\omega_3 h\lambda - \rho\sqrt{4\pi^2 + (h\lambda)^2}. \qquad (10.13)$$

It can be shown that for fixed ω, ρ, R, h, the zeros of the function F in λ solve the nonlinear problem (10.12). There exists a number of fast iterative algorithms in the numerical analysis literature that can be used to find the roots of a smooth function, such as the bisection Method and the Newton's method (see [11, 58]). To effectively solve for every root of the function $F(\omega, \rho, R, h; \cdot)$ lying on the interval Λ using an iterative method, we propose the following scheme. Partition the interval Λ into a sufficiently large number of sub-intervals $\{\Lambda_j\}$, with each sub-interval Λ_j having the same length. Next, for each sub-interval Λ_j, evaluate $F(\omega, \rho, R, h; \cdot)$ at the end points of Λ_j. If the signs of $F(\omega, \rho, R, h; \cdot)$ are different at the end-points of Λ_j, apply an iterative root finding algorithm to find $\lambda \in \Lambda_j$ such that $F(\omega, \rho, R, h, \lambda) = 0$; otherwise, move on to the next sub-interval Λ_{j+1}. As this process of computing $n(\omega, \rho)$ is computationally very intensive, to save computation time, one most pre-compute and store the values of $n(\omega, \rho)$ and the roots of the function $F(\omega, \rho, R, h; \cdot)$.

Once we have computed $n(\omega, \rho)$, the number of intersections between the plane $\Pi(\omega, \rho)$ and the spherical spiral curve Γ, for all $\omega \in \mathbb{S}^2$ and all $\rho \in \mathbb{R}$, the values of an appropriate weighting function $M(\omega, \lambda)$ can be computed by (10.11). Again, to save computation time, the values of $M(\omega, \lambda)$ should be pre-computed and stored for later use.

10.3 Cone-beam FBP with Acquisition from a Generic Source Curve

In Chapter 8, we discussed in detail the numerical implementation of the cone-beam FBP algorithm for an arbitrary source curve Γ satisfying Tuy's condition. One can simply follow the algorithm outlined in Section 8.3.3 to implement the non-truncated numerical inverse of the cone-beam transform with acquisition from any generic Tuy's source curve, such as the spherical spiral. In the shift-variant filtering stage of the FBP algorithm, a weighting function M should be chosen appropriately for an exact and stable reconstruction.. The weighting function for the spherical spiral is presented in Section 10.2.2.

Chapter 11

Numerical Results for ROI Tomography with Spherical Spiral Acquisition

In this chapter, we analyze the performance of our ROI reconstruction algorithm through extensive numerical experiments with simulated truncated cone-beam data acquired from the spherical spiral acquisition geometry discussed in Chapter 10. The conditions imposed on the density function $f : \mathbb{R}^3 \to \mathbb{R}$ and the cone-beam source curve Γ are to be assumed as before. Assume that f has a compact support on the closed ball Ω of $\mathbb{R}^3$. We will denote by f_{rec} the reconstruction of f.

11.1 Reconstruction Setup

For our numerical experiments, we have implemented the ROI reconstruction algorithm using the non-truncated cone-beam inverse operator Z, which is based on the

shift-variant cone-beam FBP formula presented in Chapter 8. The reconstruction was set on cone-beam acquisition geometry consisting of a spherical spiral (10.2) and a flat planar detector. The parameters of the reconstruction geometry are outlined below.

3D image size	=	256^3 voxels
Radius of the spherical spiral	=	3200 voxels
Number of turns T of the spiral	=	3
Value of h	=	0.35
Number of sources	=	720
Detector size	=	256 rows, 256 columns
Detector spacing	=	1 voxel
Source to detector distance	=	3200 voxels

The center of the 3D image and the center of the spherical spiral coincide. The large radius 3200 voxels for the spherical spiral curve Γ was selected after performing intensive numerical simulations; it gave the most accurate reconstruction in the cases of non-truncated cone-beam inversion. To process the cone-beam projection data for the shift-variant cone-beam FBP algorithm following the methods outlined in Chapter 8, we have sampled $180 \times 256 = 46,080$ parametric lines per detector, where 180 is the number of direction angles ϑ and 256 is the number of sampled lines per direction ϑ.

For the regularization step of the ROI-reconstruction algorithm, we chose *hard-thresholding* regularization method, as we found this method to be superior when compared with other density regularization methods (see Chapter 6 for details). We

used Daubechies wavelets (Daub4) (see [38] for details) in $\mathbb{R}^3$ to generate the wavelet decomposition of the density function of interest, and discarded 90% of the wavelets coefficients of smaller magnitudes.

11.2 Performance of our ROI-Reconstruction Algorithm

We have tested ROI reconstruction using our algorithm on the discretized densities of the 3D Shepp-Logan (Figure 9.1) head phantom and the Mouse tissue (Figure 9.5). We have selected several spherical regions of interest C of varying radii between 60 and 90 voxels, arbitrarily located strictly within the support of the density.

We see that direct application of the shift-variant cone-beam FBP to the ROI-truncated projections gives slightly better results with spherical spiral acquisition than twin-circular acquisition. This is largely due to the fact that the spherical spiral curve Γ makes more redundant cone-beam measurements than the twin-circular curve. Regardless of this fact, as can be seen in Figure 11.1 and Figure 11.3, severe artifacts such as heavy blurring and ring artifacts are present in the naive ROI-reconstruction method, whereas our algorithm gives far superior results. The line intensity profiles of the mid-planar slices of the images reconstructed by the two methods and the ground truth are shown in Figure 11.2 and Figure 11.4. We see that our ROI reconstruction follows the true density much closely than the naive reconstruction, especially on the boundaries of the ROI.

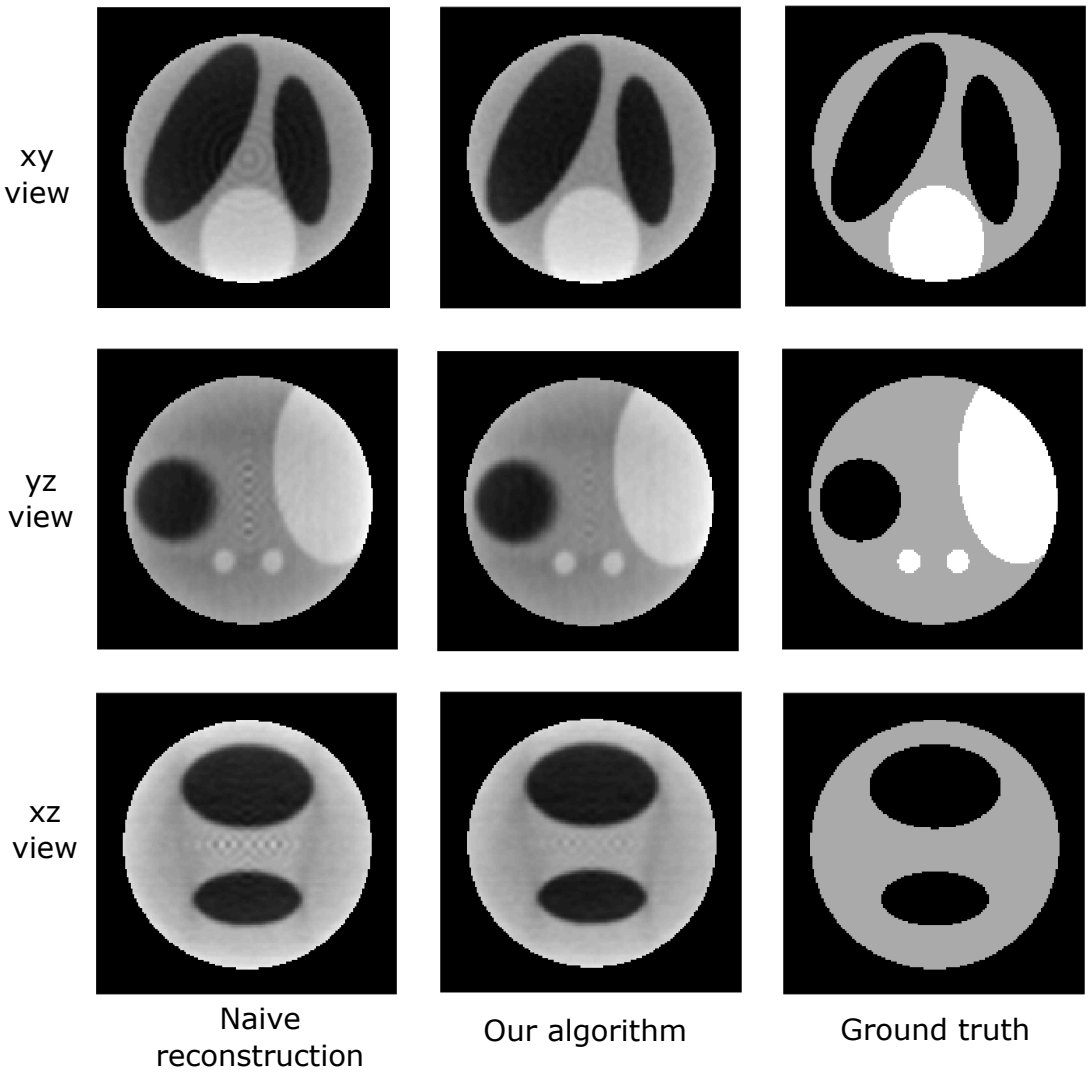

Figure 11.1: Visual comparison of ROI reconstruction for 3D Shepp-Logan phantom using Spherical Spiral acquisition and ROI-truncated projections. ROI radius = 75 voxels. Middle slices are shown from the xy, yz, and xz planes. From left to right: direct application of shift-variant cone-beam FBP; our iterative ROI reconstruction; ground truth.

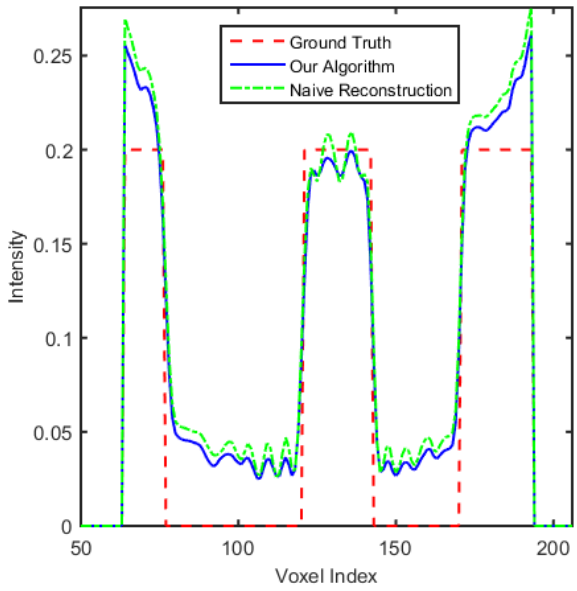

(a) xy slice

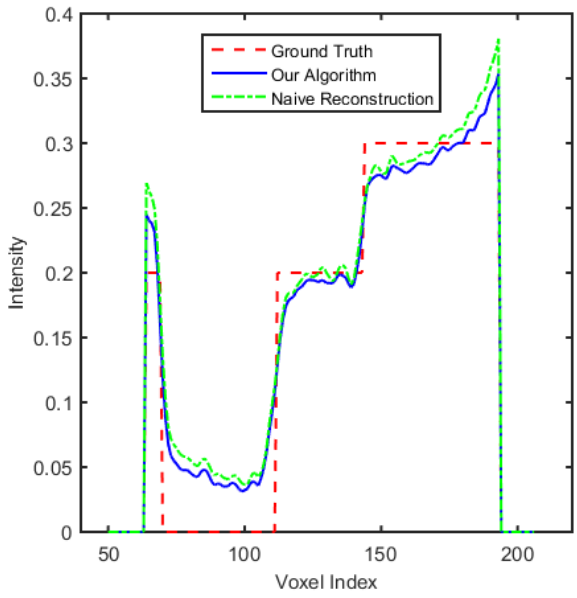

(b) yz slice

Figure 11.2: Visual comparison of ROI reconstruction for 3D Shepp-Logan phantom using Spherical Spiral acquisition and ROI-truncated projections. ROI radius = 75 voxels. Intensity profiles for a fixed row corresponding to the mid-planar slices are shown.

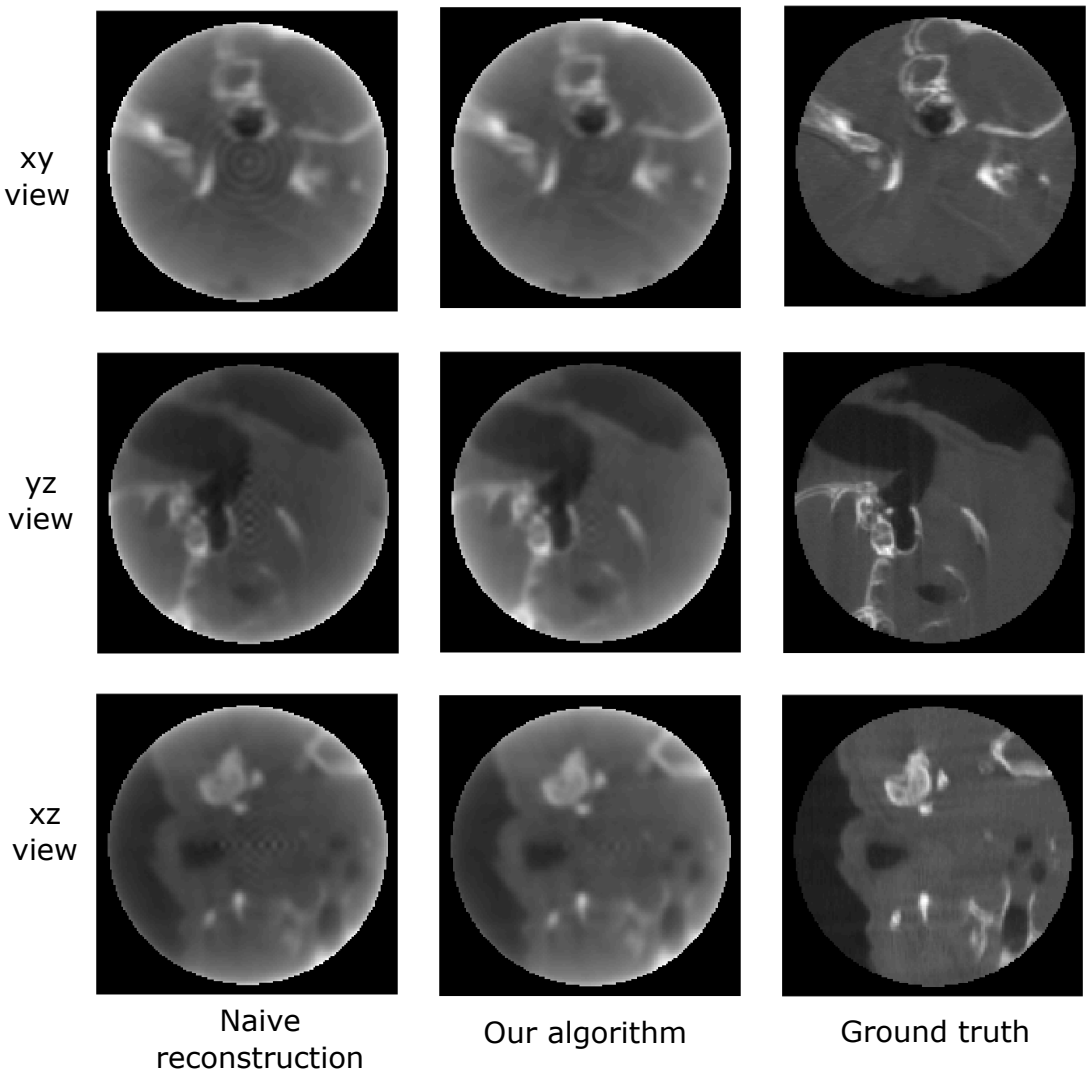

Figure 11.3: Visual comparison of ROI reconstruction for Mouse Tissue using Spherical Spiral acquisition and ROI-truncated projections. ROI radius = 75 voxels. Middle slices are shown from the xy, yz, and xz planes. From left to right: direct application of shift-variant cone-beam FBP; our iterative ROI reconstruction; ground truth.

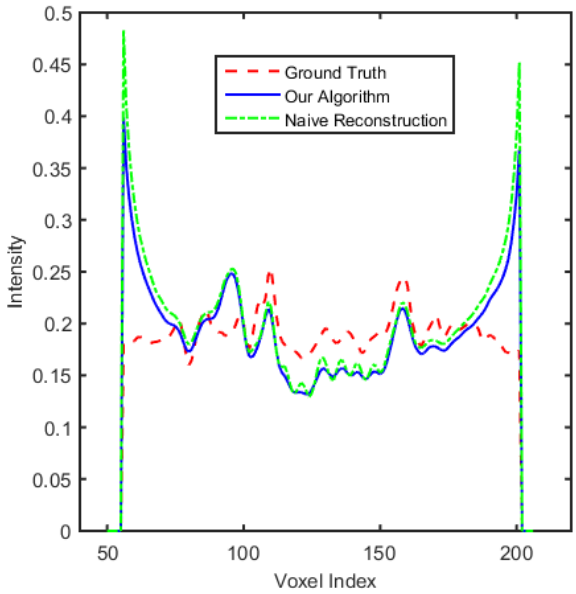

(a) xy slice

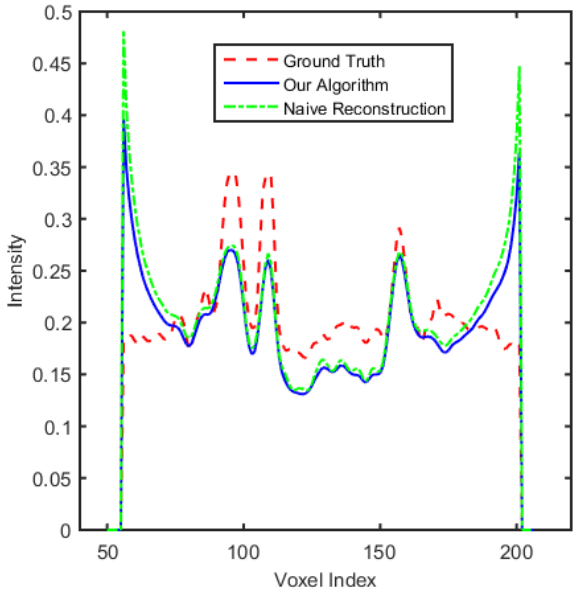

(b) yz slice

Figure 11.4: Visual comparison of ROI reconstruction for Mouse Tissue using Spherical Spiral acquisition and ROI-truncated projections. ROI radius = 75 voxels. Intensity profiles for a fixed row corresponding to the mid-planar slices are shown.

We will assess the performance of our ROI reconstruction method and compare it to the performance of the naive method quantitatively using the two metrics RLE and $PSNR$ introduced in the in Chapter 9. The truncation level $\tau(C)$ from (9.3) is also presented for each ROI C to quantify the dose-reduction associated with each C-truncated cone-beam acquisition. When a region of interest C of radius 60 voxels is chosen for ROI reconstruction of the Mouse Tissue, a direct application of the cone-beam FBP method to the truncated projection data yields $RLE = 25.2\%$, whereas our iterative ROI reconstruction method performs better with $RLE = 19.2\%$ and $PSNR = 22.3$ dB after 18 iterations. For ROI reconstruction of the Shepp-Logan phantom with an ROI of radius 75 voxels, after 16 iterations our iterative algorithm yields $RLE = 15.7\%$ and $PSNR = 18.9$ dB, whereas a direct application of cone-beam FBP to truncated data gives $RLE = 19.4\%$. Additional ROI reconstruction results for the Shepp-Logan phantom are given for different ROI radii in Table 11.1 and Table 11.2.

Table 11.1: Performance of our ROI reconstruction of Shepp-Logan Phantom for various spherical ROI radii.

ROI radius	**Truncation level**	**RLE**	**PSNR**
60 voxels	81.8%	48.5%	11.9 dB
75 voxels	71.9%	15.7%	18.9 dB
90 voxels	59.9%	18.8%	20.3 dB

Table 11.2: Performance of our ROI reconstruction of Mouse Tissue for various spherical ROI radii.

ROI radius	**Truncation level**	**RLE**	**PSNR**
60 voxels	81.8%	19.2%	23.7 dB
75 voxels	71.9%	13.9%	26.5 dB
90 voxels	59.9%	14.7%	26.4 dB

11.3 Numerical Analysis of the Convergence our ROI-Reconstruction Algorithm

In this section, we present the critical radius condition for ϵ-accurate ROI reconstruction from C-truncated cone-beam projections and the rate of convergence of our algorithm.

11.3.1 Critical Radius

We have stated in Chapter 6 that for $\epsilon > 0$, there exists a *critical radius* $\rho(\epsilon)$ such that our ROI reconstruction algorithm converges to an ϵ-accurate inverse within a ROI C strictly within Ω, given that the radius of C is no smaller than the critical radius $\rho(\epsilon)$. The statement was proved rigorously by our research team (see [3] for details).

Based on our extensive numerical experiments of ROI reconstruction of the two discretized densities (Shepp-Logan and Mouse Tissue) on several regions of interest C of various radii, we estimated the critical radius $\rho(\epsilon)$ of ROI reconstruction for each image. With a fixed accuracy level $\epsilon = 14\%$, the estimated the critical radiii ρ of ROI reconstruction of the Shepp-Logan and the Mouse Tissue densities were 83 and 68 voxels, respectively. It is interesting to note that the Mouse Tissue gives a smaller critical radius, due to its smoothness.

11.3.2 Convergence Speed

It is proved theoretically in [3] that our ROI reconstruction algorithm converges to an ϵ-accurate at an exponential speed, given that the radius of the region of interest

C is no smaller than a critical radius $\rho(\epsilon)$.

It is evident from the error plots presented in Figure 11.5 and Figure 11.6 that the relative reconstruction error decays exponentially after just a iterations. Extensive experimental results are necessary to numerically estimate the rate at which the error of our ROI-reconstruction algorithm decreases. However, we can conclude based on our experiments that the algorithm will always converge, given the density is sufficiently regular and the radius of the ROI is no smaller than a critical radius.

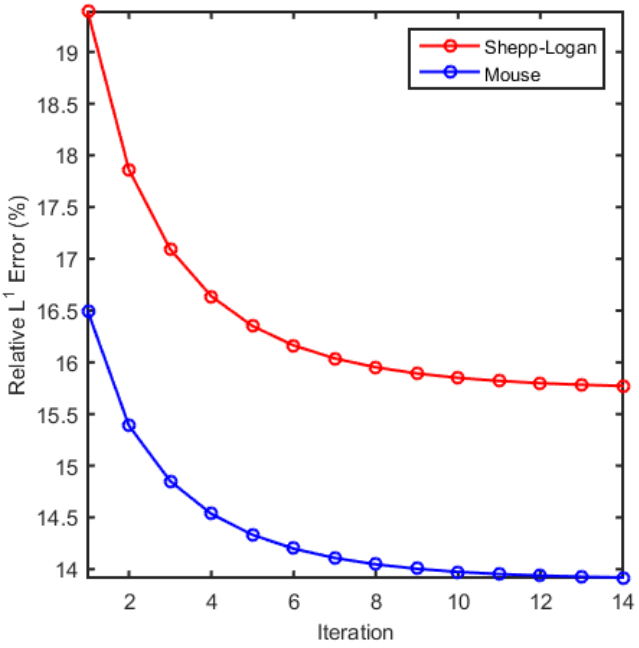

Figure 11.5: Relative L^1 Error (RLE) vs iteration of our algorithm for ROI reconstruction of two images: Shepp-Logan (red) and Mouse Tissue (blue). Spherical ROI radius = 75 voxels.

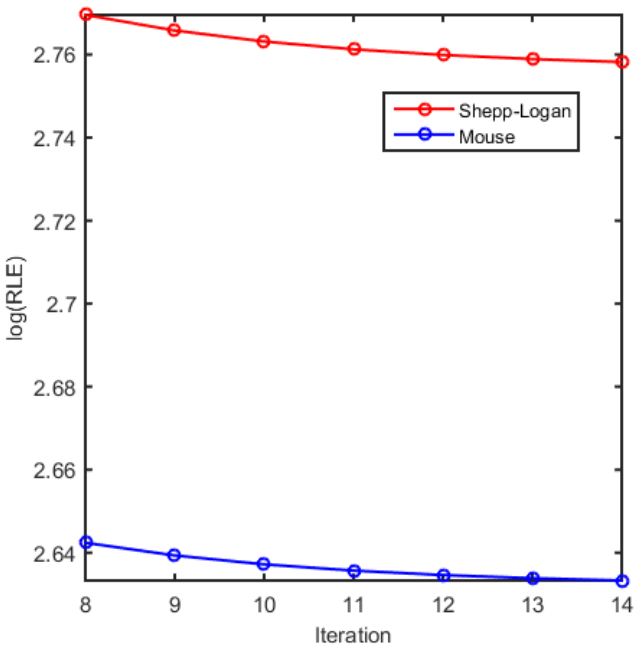

Figure 11.6: Linear relationship between the logarithm of the Relative L^1 Error (RLE) and iterations of our algorithm for ROI reconstruction of two images: Shepp-Logan (red) and Mouse Tissue (blue). Spherical ROI radius = 75 voxels. Between iterations 8 and 14, the logarithm of the error curves tend to be linear.

Chapter 12

Conclusion

In this thesis, we have examined the problem of three-dimensional region-of-interest tomographic reconstruction using ROI-truncated cone-beam data. The ROI reconstruction from truncated projections is useful for cases which require several follow up scans, for example scans to monitor the progress of a tumor. If only a specific region of interest C needs to be monitored, our iterative ROI-reconstruction algorithm can be used to reconstruct this region. Our method greatly reduces the radiation exposure of a patient to harmful x-rays.

Our iterative ROI-reconstruction algorithm is used with fairly generic cone-beam acquisition setups, with sources located on arbitrary bounded smooth curves $\Gamma \in \mathbb{R}^3$ satisfying classical Tuy's condition. Our algorithm was validated with simulation of truncated cone-beam data acquired on the twin-circular curve and the spherical spiral curve. In both of these acquisition geometries, our algorithm successfully computed ϵ-accurate inverses for sufficiently small regions of interest, from ROI-truncated cone-beam data, with less than 20 iterations.

There are a few advantages to using our ROI-reconstruction algorithm by com-

parison to other algorithms available in the current literature (see Chapter 2). Our ROI-reconstruction method imposes no local restriction on the density f, aside from the fact that f must be compactly supported and sufficiently regular. Many existing methods in the ROI CT literature require the density of f restricted to the region of interest C to be piecewise constant or piecewise polynomial, which can be a very strong condition to impose in practical medical imaging situations. Secondly, our method gives a critical radius condition for the ROIs, ensuring the convergence of our algorithm.

12.1 Future Research

Novel Cone-beam CT Geometries

Our ROI-reconstruction method was validated through numerical experiments of ROI-reconstruction with acquisition on two different source curves: the twin-circular curve and the spherical spiral. However, one may seek the best cone-beam acquisition curve that can be used for practical applications of both full and region of interest reconstruction.

Computational Improvement

For our numerical experiments, our iterative ROI-reconstruction algorithm using Grangeat's variant cone-beam FBP was written entirely in Matlab, using some parallelization in the filtering stages. As well-known, Matlab codes run significantly slower than codes written in a lower level languages such as C. For faster computations, we need to implement our ROI-reconstruction algorithm using a low-level language,

using parallelization where applicable.

Recently, a number of researchers studied graphical processing unit (GPU) based implementations of cone-beam CT algorithms [24,63] for faster acquisition and reconstruction time. Modern GPUs are very efficient at manipulating computer graphics and image processing, and their highly parallel structure makes them more effective than general-purpose CPUs for algorithms where the processing of large blocks of visual data is done in parallel. Our ROI-reconstruction needs to be modified to be implementable with a GPU unit.

Bibliography

[1] C. Axelsson and P. Danielsson, "Three-dimensional reconstruction from cone-beam data in $o(n^3 \log n)$ time," *Physics in Medicine and Biology*, vol. 39, no. 3, p. 477, 1994.

[2] C. Axelsson-Jacobson, R. Guillemaud, P.-E. Danielsson, P. Grangeat, M. Defrise, and R. Clack, "Comparison of three 3D-reconstruction methods from cone-beam data," in *Three-Dimensional Image Reconstruction in Radiology and Nuclear Medicine*. Springer, 1996, pp. 3–18.

[3] R. Azencott, B. G. Bodmann, T. Chowdhury, D. Labate, A. Sen, and D. Vera, "Region-of-interest reconstruction from truncated cone-beam projections," *arXiv*, 2016. [Online]. Available: `http://arxiv.org/abs/1502.01114v3`

[4] J. Barros-Neto, *An introduction to the theory of distributions*. M. Dekker, 1973, vol. 14.

[5] R. Bracewell, "The Fourier transform and its applications," *New York*, vol. 5, 1965.

[6] D. Brenner, "Minimising medically unwarranted computed tomography scans," *Annals of the ICRP*, vol. 41, no. 3, pp. 161–169, 2012.

[7] T. M. Buzug, *Computed tomography: from photon statistics to modern cone-beam CT*. Springer Science & Business Media, 2008.

[8] T. Chowdhury, A. Sen, and R. Azencott, "An iterative algorithm for region-of-interest reconstruction with cone-beam acquisitions on a generic source trajectory," in *13th International Meeting on Fully Three-Dimensional Image Reconstruction in Radiology and Nuclear Medicine (Fully3D 2015)*, 2015.

[9] R. Clackdoyle and M. Defrise, "Tomographic reconstruction in the 21st century," *Signal Processing Magazine, IEEE*, vol. 27, no. 4, pp. 60–80, 2010.

[10] M. Courdurier, F. Noo, M. Defrise, and H. Kudo, "Solving the interior problem of computed tomography using a priori knowledge," *Inverse problems*, vol. 24, no. 6, p. 065001, 2008.

[11] G. Dahlquist and Å. Björck, "Numerical methods in scientific computing, volume I," *SIAM, Philadelphia*, vol. 55, 2007.

[12] M. Defrise and R. Clack, "Filtered backprojection reconstruction of combined parallel beam and cone beam spect data," *Physics in medicine and biology*, vol. 40, no. 9, p. 1517, 1995.

[13] ——, "A cone-beam reconstruction algorithm using shift-variant filtering and cone-beam backprojection," *Medical Imaging, IEEE Transactions on*, vol. 13, no. 1, pp. 186–195, 1994.

[14] P. Edholm, G. T. Herman, and D. A. Roberts, "Image reconstruction from linograms: implementation and evaluation," *Medical Imaging, IEEE Transactions on*, vol. 7, no. 3, pp. 239–246, 1988.

[15] P. R. Edholm and G. T. Herman, "Linograms in image reconstruction from projections," *Medical Imaging, IEEE Transactions on*, vol. 6, no. 4, pp. 301–307, 1987.

[16] L. Feldkamp, L. Davis, and J. Kress, "Practical cone-beam reconstruction," *J. Opt. Soc. Am. A*, vol. 1, no. 6, pp. 612–619, 1984.

[17] D. V. Finch, "Cone beam reconstruction with sources on a curve," *SIAM Journal on Applied Mathematics*, vol. 45, no. 4, pp. 665–673, 1985.

[18] I. M. Gelfand, I. Gel'fand, and G. Evgen'evič, *Generalized functions. Vol. 1, Properties and operations.* Academic Press, 1969.

[19] P. Grangeat, "Reconstruire les structures tridimensionnelles internes de l'organisme humain," Ph.D. dissertation, 1990.

[20] ——, "Mathematical framework of cone beam 3D reconstruction via the first derivative of the Radon transform," in *Mathematical methods in tomography.* Springer, 1991, pp. 66–97.

[21] S. Helgason, *The Radon transform on R^n.* Springer, 2011.

[22] W. Huda, W. Randazzo, S. Tipnis, G. D. Frey, and E. Mah, "Embryo dose estimates in body CT," *American Journal of Roentgenology*, vol. 194, no. 4, pp. 874–880, 2010.

[23] C. Jacobson, "Fourier methods in 3D reconstruction from cone-beam data: Department of electrical engineering," Ph.D. dissertation, Dissertation, 1996.

[24] X. Jia, Y. Lou, R. Li, W. Y. Song, and S. B. Jiang, "GPU-based fast cone beam CT reconstruction from undersampled and noisy projection data via total variation," *Medical physics*, vol. 37, no. 4, pp. 1757–1760, 2010.

[25] P. M. Joseph, "An improved algorithm for reprojecting rays through pixel images," *Medical Imaging, IEEE Transactions on*, vol. 1, no. 3, pp. 192–196, 1982.

[26] A. C. Kak and M. Slaney, *Principles of computerized tomographic imaging*. IEEE press, 1988.

[27] A. Katsevich, "Theoretically exact filtered backprojection-type inversion algorithm for spiral CT," *SIAM Journal on Applied Mathematics*, vol. 62, no. 6, pp. 2012–2026, 2002.

[28] ——, "An improved exact filtered backprojection algorithm for spiral computed tomography," *Advances in Applied Mathematics*, vol. 32, no. 4, pp. 681–697, 2004.

[29] E. Katsevich, A. Katsevich, and G. Wang, "Stability of the interior problem with polynomial attenuation in the region of interest," *Inverse problems*, vol. 28, no. 6, p. 065022, 2012.

[30] E. Klann, E. T. Quinto, and R. Ramlau, "Wavelet methods for a weighted sparsity penalty for region of interest tomography," *Inverse Problems*, vol. 31, no. 2, p. 025001, 2015.

[31] P. Kuchment, *The Radon transform and medical imaging*. SIAM, 2014, vol. 85.

[32] H. Kudo and T. Saito, "Feasible cone beam scanning methods for exact reconstruction in three-dimensional tomography," *JOSA A*, vol. 7, no. 12, pp. 2169–2183, 1990.

[33] ——, "Derivation and implementation of a cone-beam reconstruction algorithm for nonplanar orbits," *Medical Imaging, IEEE Transactions on*, vol. 13, no. 1, pp. 196–211, 1994.

[34] M. Lee, Y. Han, J. P. Ward, M. Unser, and J. C. Ye, "Interior tomography using 1D generalized total variation. Part II: Multiscale implementation," *SIAM Journal on Imaging Sciences*, vol. 8, no. 4, pp. 2452–2486, 2015.

[35] S. W. Lee, G. Cho, and G. Wang, "Artifacts associated with implementation of the Grangeat formula," *Medical physics*, vol. 29, no. 12, pp. 2871–2880, 2002.

[36] M. J. Lighthill, "Fourier analysis and generalized functions," *Cambridge University Fluid Mech*, vol. 1960, pp. 9–305, 1960.

[37] A. K. Louis, "Development of algorithms in computerized tomography," in *Proceedings of Symposia in Applied Mathematics*, vol. 63, 2006, p. 25.

[38] S. Mallat, *A wavelet tour of signal processing*. Academic press, 1999.

[39] R. B. Marr, C.-N. Chen, and P. C. Lauterbur, "On two approaches to 3D reconstruction in NMR zeugmatography," in *Mathematical aspects of computerized tomography*. Springer, 1981, pp. 225–240.

[40] J. D. Mathews, A. V. Forsythe, Z. Brady, M. W. Butler, S. K. Goergen, G. B. Byrnes, G. G. Giles, A. B. Wallace, P. R. Anderson, T. A. Guiver, P. McGale,

T. M. Cain, J. G. Dowty, A. C. Bickerstaffe, and S. C. Darby, "Cancer risk in 680,000 people exposed to computed tomography scans in childhood or adolescence: data linkage study of 11 million australians," *BMJ*, vol. 346, 2013. [Online]. Available: `http://www.bmj.com/content/346/bmj.f2360`

[41] F. Natterer, *The mathematics of computerized tomography*. SIAM, 1986, vol. 32.

[42] ——, "Numerical methods in tomography," *Acta Numerica*, vol. 8, pp. 107–141, 1999.

[43] F. Natterer and F. Wübbeling, *Mathematical methods in image reconstruction*. SIAM, 2001.

[44] F. Noo, M. Defrise, and R. Clack, "FBP reconstruction of cone-beam data acquired with a vertex path containing a circle," in *Nuclear Science Symposium, 1996. Conference Record., 1996 IEEE*, vol. 3. IEEE, 1996, pp. 1698–1702.

[45] F. Noo, R. Clack, and M. Defrise, "Cone-beam reconstruction from general discrete vertex sets using Radon rebinning algorithms," *Nuclear Science, IEEE Transactions on*, vol. 44, no. 3, pp. 1309–1316, 1997.

[46] F. Noo, M. Defrise, R. Clack, T. Roney, T. White, and S. Galbraith, "Stable and efficient shift-variant algorithm for circle-plus-lines orbits in cone-beam CT," in *Image Processing, 1996. Proceedings., International Conference on*, vol. 3. IEEE, 1996, pp. 539–542.

[47] T. Olson, "Optimal time-frequency projections for localized tomography," *Annals of biomedical engineering*, vol. 23, no. 5, pp. 622–636, 1995.

[48] T. Olson and J. DeStefano, "Wavelet localization of the Radon transform," *Signal Processing, IEEE Transactions on*, vol. 42, no. 8, pp. 2055–2067, 1994.

[49] J. Radon, "Über die bestimmung von funktionen durch ihre integralwerte längs gewisser mannigfaltigkeiten," *Classic papers in modern diagnostic radiology*, vol. 5, 2005.

[50] F. Rashid-Farrokhi, K. Liu, C. A. Berenstein, and D. Walnut, "Wavelet-based multiresolution local tomography," *Image Processing, IEEE Transactions on*, vol. 6, no. 10, pp. 1412–1430, 1997.

[51] A. Sen, "Searchlight CT: A new regularized reconstruction method for highly collimated x-ray tomography," Ph.D. dissertation, University of Houston, Houston, Texas, May 2012.

[52] L. A. Shepp, "Computerized tomography and nuclear magnetic resonance." *Journal of computer assisted tomography*, vol. 4, no. 1, pp. 94–107, 1980.

[53] L. A. Shepp and B. F. Logan, "The Fourier reconstruction of a head section," *Nuclear Science, IEEE Transactions on*, vol. 21, no. 3, pp. 21–43, 1974.

[54] R. L. Siddon, "Fast calculation of the exact radiological path for a three-dimensional CT array," *Medical physics*, vol. 12, no. 2, pp. 252–255, 1985.

[55] E. Y. Sidky, C.-M. Kao, and X. Pan, "Accurate image reconstruction from few-views and limited-angle data in divergent-beam CT," *Journal of X-ray Science and Technology*, vol. 14, no. 2, pp. 119–139, 2006.

[56] B. D. Smith, "Image reconstruction from cone-beam projections: necessary and sufficient conditions and reconstruction methods," *Medical Imaging, IEEE Transactions on*, vol. 4, no. 1, pp. 14–25, 1985.

[57] ——, "Cone-beam tomography: recent advances and a tutorial review," *Optical Engineering*, vol. 29, no. 5, pp. 524–534, 1990.

[58] J. Stoer and R. Bulirsch, *Introduction to numerical analysis*. Springer Science & Business Media, 2013, vol. 12.

[59] H. K. Tuy, "An inversion formula for cone-beam reconstruction," *SIAM Journal on Applied Mathematics*, vol. 43, no. 3, pp. 546–552, 1983.

[60] G. Wang and H. Yu, "The meaning of interior tomography," *Physics in medicine and biology*, vol. 58, no. 16, p. R161, 2013.

[61] G. Wang, S. Zhao, and P.-C. Cheng, "Exact and approximate conebeam x-ray microtomography," *Focus of Multidimensional Microscopy*, vol. 1, pp. 233–261, 1999.

[62] J. P. Ward, M. Lee, J. C. Ye, and M. Unser, "Interior tomography using 1D generalized total variation. Part I: Mathematical foundation," *SIAM Journal on Imaging Sciences*, vol. 8, no. 1, pp. 226–247, 2015.

[63] H. Yan and X. Wang, "Multi-GPU cone-beam CT reconstruction," *Graphics Processing Unit-Based High Performance Computing in Radiation Therapy*, p. 83, 2015.

[64] Y. Ye, H. Yu, and G. Wang, "Exact interior reconstruction from truncated limited-angle projection data," *Journal of Biomedical Imaging*, vol. 2008, p. 5, 2008.

[65] Y. Ye, H. Yu, Y. Wei, and G. Wang, "A general local reconstruction approach based on a truncated Hilbert transform," *Journal of Biomedical Imaging*, vol. 2007, no. 1, pp. 2–2, 2007.

[66] H. Yu and G. Wang, "Compressed sensing based interior tomography," *Physics in medicine and biology*, vol. 54, no. 9, p. 2791, 2009.

[67] G. L. Zeng, R. Clack, and G. Gullberg, "Implementation of Tuy's cone-beam inversion formula," *Physics in medicine and biology*, vol. 39, no. 3, p. 493, 1994.

[68] S. Zhao and G. Wang, "Feldkamp-type cone-beam tomography in the wavelet framework," *Medical Imaging, IEEE Transactions on*, vol. 19, no. 9, pp. 922–929, 2000.

[69] A. Ziegler, T. Nielsen, and M. Grass, "Iterative reconstruction of a region of interest for transmission tomography," *Medical physics*, vol. 35, no. 4, pp. 1317–1327, 2008.